Spring 2024

Exploring Cation Exchange: Unveiling Its Significance in Biochar and Bioenergetics Applications

Gyanendra Kharel
Old Dominion University, gkharell72@gmail.com

EXPLORING CATION EXCHANGE: UNVEILING ITS SIGNIFICANCE IN BIOCHAR AND BIOENERGETICS APPLICATIONS

by

Gyanendra Kharel
M.S. December 2013, Tribhuvan University
M.S. December 2021, Old Dominion University

A Dissertation Submitted to the Faculty of
Old Dominion University in Partial Fulfillment of the
Requirements for the Degree of

DOCTOR OF PHILOSOPHY

CHEMISTRY

OLD DOMINION UNIVERSITY
May 2024

Approved by:

James W. Lee (Director)

Sandeep Kumar (Member)

Jingdong Mao (Member)

John Cooper (Member)

ABSTRACT

EXPLORING CATION EXCHANGE: UNVEILING ITS SIGNIFICANCE IN BIOCHAR AND BIOENERGETICS APPLICATIONS

Gyanendra Kharel
Old Dominion University, 2024
Director: Dr. James W. Lee

Cation exchange, a cornerstone of soil chemistry and nutrient cycling, is a fundamental chemical process that occurs in soils, sediments, membranes, and other solid materials. It involves the interchange of positively charged ions, or cations, between a solid matrix and a surrounding solution. This process is crucial in various natural and engineered systems, leading to a range of applications across different fields.

This dissertation presents an extensive investigation into the applications of cation exchange in the fields of biochar and bioenergetics, encompassing three distinct aims. The first aim concentrates on the surface oxygenation of biochar through ozonization, aiming to achieve an exceptional cation exchange capacity. This innovative approach seeks to transform biochar into a humic like material through controlled ozonization, promising implications for soil fertility enhancement and nutrient management. This was accomplished by treating the biochar with ozone for 90 minutes in an enclosed vessel. The initial CEC value of untreated biochar ranged between 14 and 17 cmol/kg. However, ozone treatment led to a remarkable increase in CEC, with values ranging from 109 to 152 cmol/kg. The ozonization process also induced a significant reduction in biochar pH, from 9.82 to as low as 3.07, indicating the formation of oxygen-functional groups, particularly carboxylic acids, on the biochar's surface.

In the second research aim, the focus shifts to the solubilization of phosphorus from soil utilizing ozonized biochar. This strategy explores the potential of ozonized biochar to enhance phosphorus availability while minimizing phytotoxicity. By coupling the findings from first aim with the outcomes of this aim, a comprehensive approach to sustainable phosphorus management in agriculture is explored, contributing to the development of eco-friendly fertilization practices.

The final aim introduces a paradigm shift by demonstration of a protonic capacitor and investigation of cation-proton exchange with transmembrane-electrostatically localized protons (TELP) at a liquid-membrane interface. Understanding the complexities of cation-proton exchange could potentially revolutionize bioenergetic mechanisms, particularly in microbial systems. This pioneering endeavor not only provides fundamental insights into cation exchange processes but also offers a bridge to the field of bioenergetics.

I dedicate this dissertation to my father, Hari Prasad Kharel, my mother, Pabitra Kharel, my wife, Sushma Nembang, my little daughter, Reeyona N Kharel, and all my family members who have been my source of inspiration, support, and guidance.

ACKNOWLEDGEMENTS

First and foremost, I express my deepest gratitude to my advisor, Dr. James W. Lee, for his unwavering support, invaluable guidance, and scholarly insights throughout every stage of this dissertation. His expertise and mentorship have been instrumental in shaping the direction and depth of my research. I am profoundly grateful to my dissertation committee members, Dr. Jingdong Mao, Dr. John Cooper, and Dr. Sandeep Kumar, for their expertise, constructive feedback, and commitment to excellence. Their collective wisdom has enriched this work immeasurably. Special thanks are due to Dr. Sandeep Kumar for the fantastic opportunities provided to work in his lab within the Environmental Engineering Department.

I extend my heartfelt appreciation to Dr. Craig A. Bayse, Dr. Bala Ramjee, and the entire faculty of the Chemistry & Biochemistry department for not only providing a stimulating academic environment and access to resources essential for conducting this research, but also for the financial support, which enabled me to pursue my doctoral studies and undertake this research endeavor. I would also like to thank Dr. Alvin Holder for his warm welcome and guidance. I am deeply thankful to Dr. Yuan Zhang for her willingness to conduct various SEM imaging. I am indebted to Dr. Xu Feng, Dr. John R. Morris, and the staff of Virginia Tech University for their administrative assistance, technical support, and provision of facilities essential for the XPS analysis of biochar. I would also like to thank Dr. Jim Ippolito for providing soil samples and Mr. Grant Scheve of Oregon Biochar Solutions for generously sending the Rogue biochar samples used in this research.

I am grateful to my colleagues, collaborators, undergraduate researchers, and fellow researchers for their friendship, stimulating discussions, and moral support. I would like to extend a special acknowledgment to my lab partners Bayan Alharbi, and Curtis Wood for their unwavering support and friendship throughout this research endeavor. Additionally, I am grateful for the guidance and advice provided by previous lab members Dr. Matthew Huff, Dr. Thu Nguyen, and Dr. Oumar Sacko, who warmly welcomed me to the lab and offered valuable insights. Their diverse perspectives and shared experiences have enriched my doctoral journey. I am deeply thankful to my friends for their encouragement, understanding, and unwavering belief in me throughout the challenges and triumphs of this doctoral journey. Their friendship has made the challenges more manageable and the successes more meaningful.

Lastly, I express my deepest appreciation to my family for their unconditional love, unwavering support, and sacrifices. Their encouragement and belief in my abilities have been my guiding light.

NOMENCLATURE

ATP	Adenosine triphosphate
ADP	Adenosine diphosphate
$FADH_2$	Flavin adenine dinucleotide
CEC	Cation exchange capacity
NMR	Nuclear Magnetic Resonance Spectroscopy
XPS	X-ray Photoelectron Spectroscopy
FTIR	Fourier-Transform Infrared Spectroscopy
EA	Elemental Analysis
SEM	Scanning Electron Microscopy
EDS	Energy Dispersive X-ray Spectroscopy
TELP	Transmembrane electrostatically localized protons
IBI	International Biochar Initiative
RBC	Rogue biochar
RBC UN	Untreated (non-ozonized) rogue biochar
RBC 90D	90-minute dry ozonized rogue biochar
RBC 90W	90-minute wet ozonized rogue biochar

P400	Pine biochar made at 400 ^{o}C
P400 UN	Untreated (non-ozonized) pine 400 biochar
P400 90D	90-minute dry ozonized pine 400 biochar
P400 90W	90-minute wet ozonized pine 400 biochar
P400 90W+S	90-minute wet ozonized and sonicated pine 400 biochar
DOC	Dissolved organic carbon
AOAC	Association of Official Analytical Chemists
USDA-ARS	U.S. Department of Agriculture – Agricultural Research Service
BET	Brunauer-Emmett-Teller
PTFE	Polytetrafluoroethylene
SRM	Standard reference material
NIST	National Institute of Standards and Technology
P-soil	Portneuf Soil
B-soil	Bennett Soil
ppm	Parts per million
pmf	Proton motive force
Tf	Teflon
Al	Aluminum

TABLE OF CONTENTS

Page

LIST OF TABLES xii

LIST OF FIGURES xiii

Chapter

1. INTRODUCTION 1
   - CATION EXCHANGE CAPACITY OF SOIL AND BIOCHAR 6
   - BIOCHAR SURFACE OXYGENATION FOR ENHANCING CEC 7
   - SOLUBILIZATION OF PHOSPHORUS WITH OZONIZED BIOCHAR 8
   - CATION-PROTON EXCHANGE IN MITOCHONDRIA 10
   - GOALS AND OBJECTIVES OF STUDY 12

2. BIOCHAR SURFACE OXYGENATION BY OZONIZATION FOR SUPER HIGH CATION EXCHANGE CAPACITY 15
   - PREFACE 15
   - INTRODUCTION 15
   - MATERIALS AND METHODS 18
   - RESULTS AND DISCUSSION 27
   - CONCLUSION 44

3. SOLUBILIZATION OF PHOSPHORUS FROM SOIL USING OZONIZED BIOCHAR AND PHYTOTOXICITY STUDY OF THE OZONIZED BIOCHAR FILTRATE 46
   - INTRODUCTION 46
   - MATERIALS AND METHODS 49
   - RESULTS AND DISCUSSION 59
   - CONCLUSION 68

4. INVESTIGATION OF CALCIUM AND MAGNESIUM CATION-PROTON EXCHANGE WITH TRANSMEMBRANE ELECTROSTATICALLY LOCALIZED PROTONS (TELP) AT A LIQUID-MEMBRANE INTERFACE 71
   - INTRODUCTION 71
   - MATERIALS AND METHODS 78
   - RESULTS AND DISCUSSION 90
   - CONCLUSION 118

5. CONCLUSIONS AND FUTURE DIRECTIONS 121

REFERENCES 124

Page

APPENDICES

A. THE CHARACTERISTICS OF ROGUE BIOCHAR 143
B. BIOCHAR CEC MEASUREMENT PROTOCOL (MODIFIED AMMONIUM ACETATE METHOD) USED AT THE USDA/ARS LABORATORY 152
C. PHOSPHORUS SOLUBILIZATION BY OZONIZED BIOCHAR AND ITS DOC FILTRATE 154
D. PHYTOTOXICITY STUDY OF OZONIZED BIOCHAR AND ITS DOC FILTRATE 157
E. CALCIUM AND MAGNESIUM CATION-PROTON EXCHANGE 162

VITA 172

LIST OF TABLES

Table Page

1. pH, CEC and BET surface area of the ground biochar before and after ozonization 30

2. Representation of the atomic concentration (in %) from XPS measurement 34

3. SEM-EDS analysis result of ozonized biochar and control biochar 35

4. Amount of DOC material extracted from the non-ozonized control biochar and the dry-ozonized biochar 38

5. Elemental analysis (oxygen and carbon) on the non-ozonized and dry-ozonized Rogue biochar samples 39

6. Germination data for the monocotyl Sorgo (*Sorghum saccharatum*) and the dicotyl mustard (*Sinapis alba*) in soil mixed with different biochar concentrations 40

7. Germination data for the dicotyls garden cress (*Lepidium sativum*) and mustard (*Sinapis alba*) in various DOC biochar filtrate concentration 43

8. Layout of phosphate assays prepared using RBC and P400 biochar 55

9. Layout of phosphate assays prepared using ozonized biochar filtrate 56

10. pH and CEC of the RBC and P400 biochar before and after ozonization 60

11. Amount of DOC material extracted from the RBC and P400 biochar before and after ozonization. The values are means ± SD (n =2) 61

12. Phosphorus concentration released by ozonized biochar (10% by soil mass) in soil after 14 days of incubation with P-soil and B-soil 62

13. Phosphorus concentration released by ozonized biochar filtrate with various DOC concentrations in soil after 30 minutes of incubation with SRM 694, P-soil, and B-soil 63

14. Change in pH of central sample chamber, change in mass of P' and $KpCa2+$ for various concentrations of $Ca(HCO_3)_2$, before and after the experiment at 200 V. 104

15. Change in pH of central sample chamber, change in mass of P' and $KpMg2+$ for various concentrations of $Mg(HCO_3)_2$ before and after the experiment at 200 V 113

LIST OF FIGURES

Figure Page

1. Cation exchange in a clay particle 2

2. Cation exchange across a biological membrane 4

3. Membrane depolarization and repolarization in single heart cells 5

4. ^{31}Phosphorus NMR of the filtrate from samples of the hydroxyapatite assay..... 10

5. Schematic for post-production biochar ozonization to create oxygen containing functional groups on biochar surfaces..... 18

6. FT-IR spectra from 400-4000 cm^{-1} for 90-min dry ozonized Rogue biochar (RBC 90D) and the untreated Rogue biochar (RBC UN) control..... 32

7. FT-IR spectra from 400-1700 cm^{-1} for 90-min dry ozonized Rogue biochar (RBC 90D) and the untreated Rogue biochar (RBC UN) control..... 33

Figure 8. SEM images of the control biochar RBC UN (left) and ozonized biochar RBC 90D (right) 36

9. Images of the test plates for phytotoxicity study of ozone treated biochar taken after 5 days of exposure of seeds of monocotyl Sorgo (*Sorghum saccharatum*) and the dicotyl mustard (*Sinapis alba*) to soil mixed with various biochar concentrations 41

10. Images of the test plates for phytotoxicity study of various concentration of ozone treated biochar DOC filtrate taken after 5 days of exposure of seeds of the dicotyls garden cress (*Lepidium sativum*) and mustard (*Sinapis alba*) 42

11. Incubations of phosphorus treatment samples 57

12. Calibration curve plotted for the area of the peak versus the phosphate concentration of the Dionex 7 Anion standard for Ion Chromatography 58

13. A part of Ion Chromatogram showing the phosphate peak for B-soil 64

14. A part of Ion Chromatogram showing the phosphate peak for P-soil 65

15. A part of Ion Chromatogram showing the phosphate peak for SRM 694 67

16. Images of the tubes for phytotoxicity study of ozone treated biochar taken after 10 days of exposure of seeds of the dicotyl garden cress (*Lepidium sativum*) to soil mixed with ozonized biochar filtrate of various DOC concentrations..... 68

Figure Page

17. TELP model for a bacterial cell membrane 75

18. ElectroPrep electrolysis system 80

19. Dimensions of the ElectroPrep electrolysis system 81

20. Experimental system design: Cathode (water) Aluminum-Teflon-Aluminum (Solution) Aluminum- Teflon-Aluminum (water) Anode 89

21. Current versus time data points recorded during 5-hour experiment utilizing 200V-driven water electrolysis when two aqueous phases are not separated by a membrane 93

22. Formation of gas bubbles at platinum electrodes during electrolysis..... 94

23. Demonstration of protonic capacitor 95

24. Distribution of the transmembrane electrostatically localized hydroxide ions..... 97

25. Distribution of the transmembrane electrostatically localized protons..... 98

26. Alkaline (excess hydroxides) corrosion and acidic (excess protons)corrosion of Aluminum membrane 99

27. Current versus time data points for the experimental system with Teflon 101

28. Current versus time data points for the experimental system with Aluminum..... 102

29. Digital images of P' aluminum membranes showing extent of acidic corrosion in the surface of aluminum revealed by the presence of brown deposits in varying concentrations of $Ca(HCO_3)_2$ solution 105

30. Photograph of various N aluminum membrane taken against the light..... 108

31. Current versus time data points for the experiments with $Ca(HCO_3)_2$ 111

32. Digital images of P' aluminum membranes showing extent of acidic corrosion in the surface of aluminum revealed by the presence of brown deposits in varying concentrations of $Mg(HCO_3)_2$ along with a typical P aluminum membrane 114

33. SEM images of the P' membranes taken after 5-hour experiment 116

34. Current versus time data points for the experiments with $Mg(HCO_3)_2$ 118

CHAPTER 1

INTRODUCTION

Cation exchange is a chemical process that occurs in soil, sediment, biological membranes, or other porous materials, where positively charged ions, known as cations, are exchanged between a solid phase and a liquid phase. This process is important in many natural systems, including the movement of nutrients through soil, the behavior of pollutants in water, the uptake of nutrients by plant roots, regulating the movement of cations through ion channels, and transport ions across the membranes through ion pumps.[1, 2]

In cation exchange in the soil or sediment, cations such as calcium (Ca^{2+}), magnesium (Mg^{2+}), and potassium (K^{+}), are attracted to negatively charged sites on the surface of the solid phase. When a solution containing other cations, such as hydrogen (H^{+}) or sodium (Na^{+}), meets the solid phase, these cations can displace the original cations and become bound to the negatively charged sites.[3] This exchange can continue until the cations in the solution are depleted or until the solid phase becomes saturated with cations. Cation exchange is an important process in soil fertility and plant nutrition because it can affect the availability of nutrients for plant uptake. For example, if a soil has a high concentration of hydrogen ions, they can displace other cations such as calcium or magnesium, making these nutrients less available to plants.[4] On the other hand, if the soil has a high concentration of calcium or magnesium ions, they can displace hydrogen ions and increase the pH of the soil, making it more alkaline and potentially more favorable for certain crops.[5]

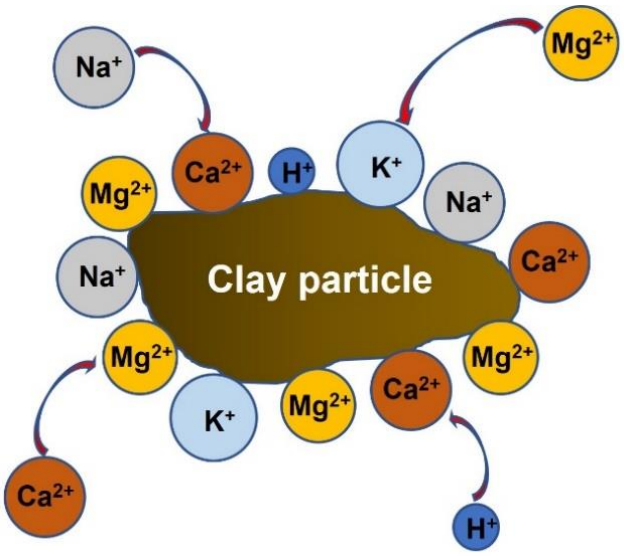

Figure 1. Cation exchange in a clay particle.

Cations such as calcium (Ca^{2+}), magnesium (Mg^{2+}), potassium (K^{+}), hydrogen (H^{+}), and sodium (Na^{+}) being exchanged between the negatively charged sites on the surface of the clay particle and the solution around the clay particle.

Biochar is a carbon-rich material produced through the process of pyrolysis, which involves heating biomass in a low-oxygen or oxygen-free environment.[6] Pyrolysis is a thermochemical decomposition of solid organic materials at elevated temperatures in the absence of oxygen.[7, 8] This prevents the complete combustion of the biomass, leading to the production of biochar along with other by-products such as syngas and bio-oil.[9] The resulting biochar is a stable form of carbon with a high surface area and a porous structure. The highly porous structure with a large surface area provides ample sites for cation and anion exchange.[10] These pores and surface functionalities can attract and retain cations. The surface of biochar contains functional groups

such as carboxyl, and hydroxyl groups. These functional groups contribute to the negative charge on the biochar surface, enabling it to attract and hold onto positively charged cations.[11]

Cation exchange is also an important process in biological membranes, which are thin, selectively permeable barriers that separate cells and their internal structures from the external environment. The cell membrane is composed of a lipid bilayer with embedded proteins, and it plays a crucial role in maintaining the internal environment of the cell and regulating the movement of ions, molecules, and other substances in and out of the cell.[12] One way that biological membranes use cation exchange is through ion channels, which are specialized proteins that span the membrane and allow specific ions to pass through.[13] Ion channels can be either gated or ungated, meaning they can be opened or closed in response to various stimuli, such as changes in membrane potential or the binding of specific molecules. These channels play a critical role in regulating the movement of cations, such as sodium (Na^+), potassium (K^+), magnesium (Mg^{2+}) and calcium (Ca^{2+}), which are important for cellular signaling, muscle contraction, heartbeat regulation, and other physiological processes.[14, 15] Another way that cation exchange is used in biological membranes is through ion pumps, which are also specialized proteins that use energy to transport ions across the membrane against their concentration gradient. One example of an ion pump is the sodium-potassium ATPase pump, which is found in all animal cells and helps maintain the balance of Na^+ and K^+ ions inside and outside the cell. The pump uses ATP (adenosine triphosphate), as an energy source to exchange three Na^+ ions for two K^+ ions across the membrane.[16]

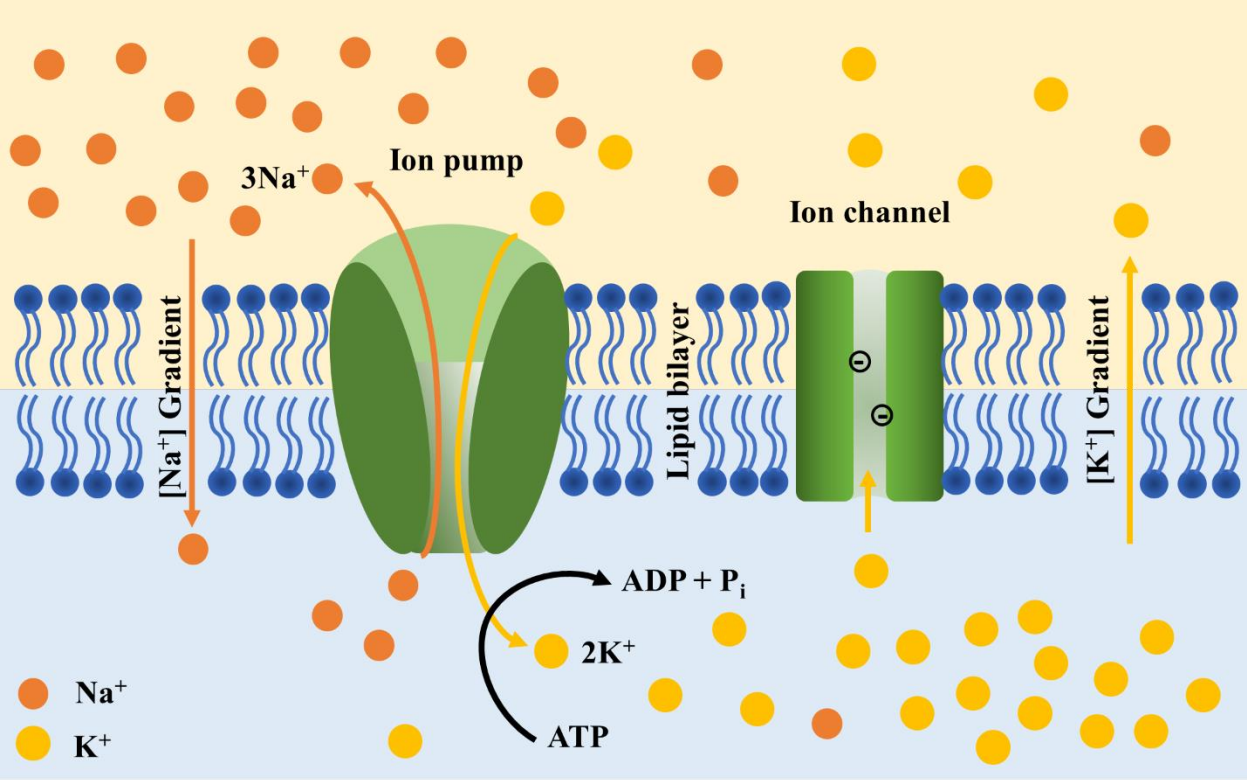

Figure 2. Cation exchange across a biological membrane.

Sketch of the structure of the cell membrane showing the ion gradient, ion channel and ion pumps for exchanging Na^+ and K^+ ions.

Cardiac muscle cell membrane depolarization and repolarization are properly timed to drive a typical heartbeat. Research indicates that contractile function can be affected by abnormal intracellular Ca^{2+} homeostasis or abnormal function of Ca^{2+}-release channel leading to ventricular arrhythmias.[15] Overall, cation exchange plays a critical role in the function of biological membranes, from regulating ion concentrations and membrane potential to maintaining the proper balance of nutrients and signaling molecules in the cell.[17]

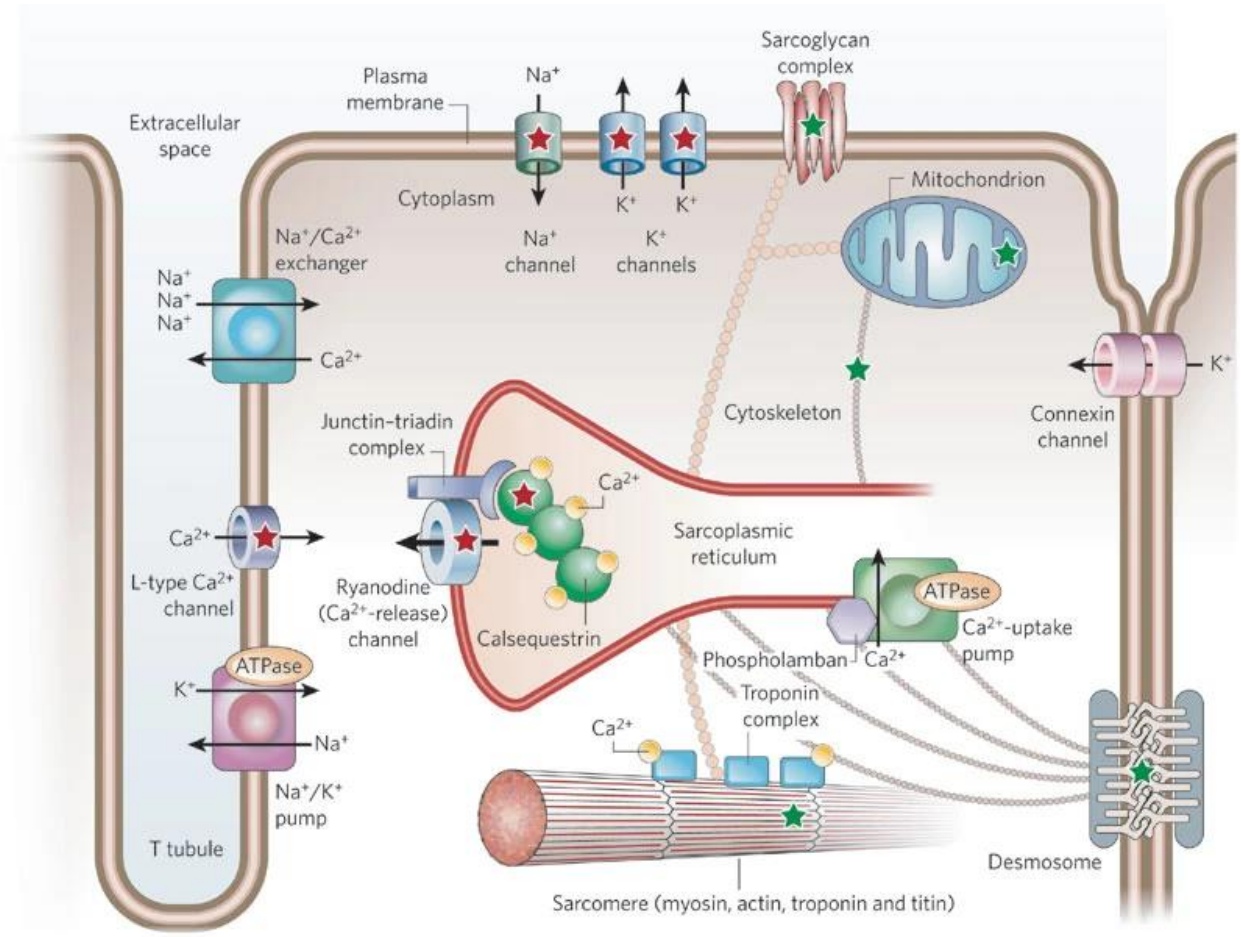

Figure 3. Membrane depolarization and repolarization in single heart cells.

Illustration of a ventricular cardiomyocyte. Membrane depolarization is brought on by ion entry through connexin channels followed by the opening of voltage-gated Na^+ channels and Na^+ entry. As the membrane depolarizes quickly, Na^+ channels are inactivated while K^+ and Ca^{2+} channels are opened. Ca^{2+} is released from the sarcoplasmic reticulum through the ryanodine channel when it enters the cell. The sarcomere is then activated by the binding of Ca^{2+} to the troponin complex. Cellular relaxation results from the exchange of Na^+/Ca^{2+} with the extracellular fluid and the removal of Ca^{2+} from the cytosol by the Ca^{2+} uptake pumps of sarcoplasmic reticulum. Intracellular Na^+ equilibrium is maintained through the Na^+/K^+ pump. (Adapted from Ref 15)

CATION EXCHANGE CAPACITY OF SOIL AND BIOCHAR

Cation exchange capacity (CEC) is a critical property used to characterize the chemical properties of soils and other natural materials such as biochar. It refers to the ability of a material to exchange cations with the surrounding environment and is often used as an indicator of soil fertility, nutrient availability, and potential for plant growth. CEC is influenced by several factors, including the composition and structure of the material, the pH of the surrounding environment, and the types and concentrations of cations present.[18] Biochar's CEC is dependent on the type of biomass and temperature during pyrolysis. Certain oxygen-containing functional groups, such hydroxyl, carboxyl, and carbonyl, are retained because of the partial breakdown of cellulose during the carbonization process, which raises the CEC of the biochar. Moreover, as biochar ages, oxidation reactions may lead to the formation of additional oxygen-containing functional groups on the surface raising the biochar's CEC. Within a specific range, the biochar CEC falls as the pyrolysis temperature rises. However, as the temperature rises, concentration of alkali/alkaline-earth metals like K, Ca, and Mg increases, which could result in a rise in CEC.[19]

CEC is typically measured in laboratory tests using methods such as the barium acetate exchange method, the ammonium acetate exchange method, or the sodium exchange method. These methods involve adding a solution containing exchangeable cations, such as barium, ammonium, and sodium, to the sample and measuring the number of cations exchanged by the material. The results are reported as the number of cations that can be held by the material per unit weight or volume.[20]

CEC is an important parameter in soil science, agronomy, and environmental studies because it can help predict the potential for nutrient leaching, soil acidification, and plant growth. Soils with high CEC are generally more fertile and can hold onto nutrients more effectively, while

soils with low CEC may require more frequent fertilizer applications to maintain plant growth.[21] In addition, CEC can also influence the mobility and bioavailability of certain pollutants, such as heavy metals, in soil and water systems. As such, understanding the CEC of soils and other natural materials is important for a wide range of applications, from agriculture and land management to environmental remediation and pollution control.[22]

BIOCHAR SURFACE OXYGENATION FOR ENHANCING CEC

One of the most valuable and simple indicators of high CEC is its oxygen to carbon ratio. A high O:C ratio within a biochar sample is considered indicative of high CEC. Understanding and optimizing the O:C ratio during biochar production is crucial for enhancing CEC.[23] Extensive research efforts focus on quantifying parameters throughout the biochar production process that contribute to high CEC. Nevertheless, there are various post-production techniques aimed at enhancing specific characteristics of biochar, emphasizing the alteration of surface area, structure, and functionality.[24, 25] The most common techniques include chemical activation with CO_2, KOH or H_2SO_4, and physical activation with steam.[26-28] These techniques aim to increase surface area, but challenges include the generation of unwanted by-products and high treatment chemical costs which can make these techniques less favorable on a large scale. Functionalization techniques, such as H_2O_2, HNO_3 and NH_3 treatment alter biochar's structure and add oxygen or nitrogen functionality.[24, 29] Some of these techniques requires the aid of microwave or ultrasound.[30, 31] Selective functionalization allows controlled tuning, influencing interactions with chemical species, hydrophobicity, and pH. Biochar surface oxygenation through ozonization can be employed to modify the surface properties of biochar while preserving the overall bulk composition of the biochar. Ozonization process introduces oxygen functionalities such as hydroxyl (-OH), carbonyl (C=O), and carboxyl (-COOH) groups markedly enhancing the CEC,

reducing pH and improving its reactivity and interaction with the surrounding environment.[25] This dissertation focuses on a breakthrough process to improve biochar CEC through biochar surface oxygenation by ozonization.[32] These techniques offer modified biochar properties for agriculture, environmental remediation, and carbon sequestration.

SOLUBILIZATION OF PHOSPHORUS WITH OZONIZED BIOCHAR

Phosphorus (P) is a basic nutrient which is essential for the growth of all life forms and is one of three key components in most typical fertilizers. Most of the fertilizer phosphorus is sourced from mined rock phosphate.[33] Because phosphorus has no alternatives, fertilizer availability, particularly with respect to phosphorus, is identified as a major issue. It was predicted in 2009 that a worldwide phosphorus peak can be reached as early as 2030.[34, 35] The prediction is based on the theory that when demand for limited resource keeps growing, production costs would go beyond profits resulting either a decrease in production or an increase in pricing.[36] Although there is controversy over the exact date of peak P production, it is generally accepted that the quality of the remaining phosphate rock is decreasing over time.[37, 38] The United States, having limited phosphate rock reserves compared to other countries like Morocco and China, heavily relies on phosphate for fertilizers and animal feed.[39] Phosphorus is overapplied in current agricultural techniques, which causes P to build up in soils and ultimately contributes to eutrophication of aquatic bodies through surface runoff.[40] Furthermore, because phosphate rock can contain significant quantities of radioactive contaminants like uranium, using P fertilizers can have negative effects on the ecosystem, such as the buildup of radioactive contaminants like uranium in the soil and food chain. Ensuring the real availability of soluble phosphorus for plants in agricultural soils remains a global concern, even though P buildup is caused by excess fertilizer use in soils. Phosphorus exhibits low solubility and is predominantly available to plants in its

inorganic forms as HPO_4^{2-} or $H_2PO_4^-$ and H_3PO_4, hindered by factors like adsorption, precipitation, and conversion into organic forms.[41, 42] Given the crucial role of phosphorus in agriculture and its limited global availability, finding efficient ways to generate and utilize phosphorus is imperative.

Biochar, a solid material derived from the thermochemical conversion of biomass in an oxygen-deprived environment, has emerged as a transformative soil amendment. Over the past decade, it has gained a lot of interest and importance in agricultural research.[43] The quality of biochar is strongly correlated to various production factors and the characteristics of the biomass used as feedstock. Because biochar retains the nutrients found in the original biomass, it acts as a reservoir for nutrients essentials for plant growth.[44, 45] Biochar is essential in enhancing the soil resilience by improving soil structural stability. Biochar has a major impact on CEC, facilitating the exchange and retention of essential cations. This leads to increased nutrient availability to plants which promotes optimal growth parameters.[46, 47] The use of biochar has a positive impact on different crops, enhancing their growth, yield, and overall health. An improved nutrient availability and soil fertility promotes to a healthier agricultural ecosystem. Biochar stands as a pioneer in sustainable agriculture since it provides complex solution to soil enhancement.[48, 49] As agricultural practices transition towards more sustainable models, the role of biochar in improving soil health and increasing crop productivity becomes gradually significant.

A recent study shows that phosphate can be solubilized from insoluble phosphate materials such as hydroxyapatite by agitating it with ozonized biochar in water. NMR results (Figure 4) showed a distinct peak for HPO_4^{2-} implying it as a dominant form of phosphate in the mixtures. Phosphorus solubilization may take place via several different molecular pathways such as protonic effect, cation exchange, and anion interchange or a combination of these. Cation exchange

pathway involves calcium removal after complexing with deprotonated carboxylate groups on the surface or in the molecules of biochar. The release of phosphate from insoluble phosphate compounds is thermodynamically favored by the removal of calcium.[50]

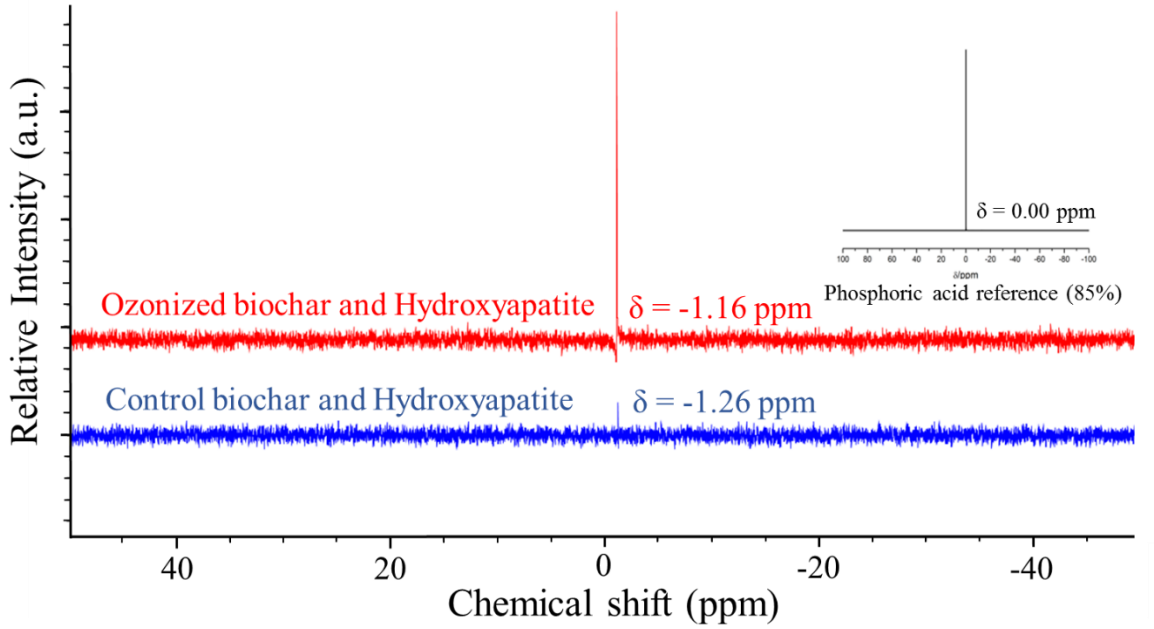

Figure 4. ^{31}Phosphorus NMR of the filtrate from samples of the hydroxyapatite assay.

The ozonized biochar and hydroxyapatite (−1.16 ppm) and the control biochar and hydroxyapatite (−1.26 ppm) representing phosphorus in the form of HPO_4^{2-}. The phosphoric acid reference is also shown in the figure. (Adapted from Ref 50)

CATION-PROTON EXCHANGE IN MITOCHONDRIA

ATP synthesis is an essential process that occurs in biological systems. ATP is a high-energy molecule that stores energy for cellular processes.[51] The synthesis of ATP occurs through

two main mechanisms: oxidative phosphorylation and substrate-level phosphorylation.[52] Oxidative phosphorylation occurs in the mitochondria of eukaryotic cells. The cation-proton exchange is a critical process involved in ATP synthesis. It occurs in the mitochondria and is essential for the maintenance of the proton gradient that drives ATP synthesis through oxidative phosphorylation. During oxidative phosphorylation, electrons are transferred from electron donors, such as NADH or $FADH_2$, to the electron transport chain, which pumps protons across the inner mitochondrial membrane, creating a proton gradient. This proton gradient is then used by ATP synthase to synthesize ATP from ADP and inorganic phosphate.[53] Substrate-level phosphorylation, on the other hand, involves the transfer of a phosphate group from a high-energy molecule, such as phosphoenolpyruvate or creatine phosphate, to ADP to form ATP. This process occurs in the cytosol and other cellular compartments and is used to generate ATP when the demand for energy is high.[54] In addition to these two mechanisms, ATP can also be synthesized through the process of photophosphorylation, which occurs in photosynthetic organisms. In this process, light energy is used to generate a proton gradient across the thylakoid membrane of the chloroplast, which is then used by ATP synthase to synthesize ATP from ADP and inorganic phosphate.[55] Overall, ATP synthesis is a critical process that occurs in all living organisms and is essential for a wide range of cellular functions, including muscle contraction, protein synthesis, and the maintenance of ion gradients.[56]

The cation-proton exchange process involves the exchange of positively charged ions, such as calcium, sodium, or potassium, with protons across the inner mitochondrial membrane. This exchange helps to maintain the proton gradient by balancing the charge across the membrane and preventing the buildup of positive charges. For example, during the transport of calcium ions into the mitochondria, an equal number of protons are transported out of the mitochondria, helping to

maintain the proton gradient.[57] Similarly, during the transport of potassium ions out of the mitochondria, an equal number of protons are transported into the mitochondria, again helping to maintain the proton gradient.[58] Therefore, the cation-proton exchange process is essential for the proper functioning of the electron transport chain and ATP synthase, which ultimately lead to the synthesis of ATP in the mitochondria.[59]

In brief, the study of cation exchange has important implications for a wide range of fields, including biology, agriculture, environmental science, and materials science. With so many advantages, the cation exchange technique is widely used in many different industrial applications including but not limited to pharmaceutical technology, industrial and potable water treatment, hydrometallurgy, soft water generation for cleaning products and soaps, metal extraction from ores, metal finishing, food and beverage production, semiconductor applications, geotechnical engineering, and pollution remediation.[60-65] By understanding cation exchange, we can develop new technologies and strategies in the field of biochar for soil science applications, to improve human health, environmental sustainability, and economic development. It can equally be applied in the field of membrane bioenergetics to get a better understanding of plant membrane transport, mitochondrial ion transport, as well as physiochemical, biochemical, and electrochemical processes in biological membranes.[66-68] With this broad spectrum of applications, cation exchange is an area of active research with many opportunities for discovery and innovation.

GOALS AND OBJECTIVES OF STUDY

The main objective of this dissertation is to comprehensively investigate cations exchange effects and further explore its applications in the field of biochar and bioenergetics. The following are the specific goals and objectives of this study:

1. Biochar surface oxygenation by ozonization for super high cation exchange capacity. As discussed above that biochar is a type of charcoal produced from organic materials through a process called pyrolysis. The addition of biochar to soil can improve CEC. So, the first goal of this dissertation is to increase the biochar CEC. Because of its high surface area and porous structure, biochar provides sites for high surface functionalization. It is fundamental to remember that different biomass types, production methods, and pyrolysis temperature might have different effects on CEC. Ozonization was conducted on a biochar with high surface area with the assumption that biochar with higher surface area shows higher improvement in CEC through surface oxygenation. Analytical techniques such as X-ray Photoelectron Spectroscopy (XPS), Fourier-Transform Infrared (FTIR) Spectroscopy, Elemental Analysis (EA), Scanning Electron Microscopy (SEM), and Energy Dispersive X-ray Spectroscopy (EDS) were employed for the characterization. The work of Chapter 2 in this dissertation has for the first time demonstrated an improvement in biochar CEC by a factor of nearly 10 through biochar surface oxygenation by ozonization. To be applied in the soil, the toxicity effect of this high CEC biochar was also studied (Goal 1- Chapter II).
2. Solubilization of phosphorus from soil using ozonized biochar and phytotoxicity study of ozonized biochar filtrate. This chapter aims in the application of ozonized biochar in solubilizing phosphorus from insoluble phosphate mineral phases present in the soil without using any strong industrial acid. Furthermore, it also aims in the investigation of phytotoxic effects of ozonized biochar water soluble organic materials. ^{31}Phosphorus Nuclear Magnetic Resonance (NMR) Spectroscopy was utilized to investigate the nature of solubilized phosphorus. After exploring the capacity of biochar to solubilize phosphorus,

additional investigations on the toxicity of biochar and its dissolved organic carbon to plant germination were conducted (Goal 2- Chapter III).

3. Investigation of calcium and magnesium cation-proton exchange with transmembrane-electrostatically localized protons (TELP) at a liquid-membrane interface. According to the TELP theory [69-72], excess positively charged protons on one side of a membrane in an aqueous medium will electrostatically repel each other to become localized at the membrane surface, drawing an equal number of excess negatively charged hydroxide anions to the opposite side of the membrane forming an "excess protons-membrane-excess hydroxides" capacitor structure. The core concept of this theory is the idea that liquid water can function as a protonic conductor because protons may move swiftly between water molecules through the "hops and turns" mechanism. Furthermore, according to the TELP theory, electrostatically localized protons at the water-membrane interface may be partially delocalized by other cations in the form of salt solutions by the process of cation exchange.[71, 72] In this chapter, the effect of divalent cations (Ca^{2+} and Mg^{2+}) on localized excess protons at the liquid-membrane was investigated by measuring the exchange equilibrium constant of Ca^{2+} and Mg^{2+} cations in exchanging with the transmembrane-electrostatically localized protons using a range of cation concentrations. The work presented in this chapter details the effect of divalent cations (Ca^{2+} and Mg^{2+}) on localized excess protons at the liquid-membrane interface and provide fundamentals to bioenergetics (Goal 3- Chapter IV).

CHAPTER 2

BIOCHAR SURFACE OXYGENATION BY OZONIZATION FOR SUPER HIGH CATION EXCHANGE CAPACITY

PREFACE

Major contents of this chapter were published in 2019 in ACS Sustainable Chemistry & Engineering and are reformatted to fit this prospectus. Below is the full citation.

Kharel, G.; Sacko, O.; Feng, X.; Morris, J. R.; Phillips, C.; Trippe, K.; Kumar, S.; Lee, J. W. Biochar Surface Oxygenation by Ozonization for Super High Cation Exchange Capacity. ACS Sustainable Chem. Eng. 2019, 7, No. 16410

INTRODUCTION

Biochar, a carbon-rich soil amendment, has been used for several centuries to improve soil fertility and increase yield. While recent interest in biochar has produced an abundance of scientific knowledge, variability in the physiochemical properties of biochar and an inability to predict biochar-soil interactions and agronomic outcomes have stifled the implementation of biochar-related practices. While some studies show improvements in crop production and soil fertility following biochar amendment, meta-analyses also demonstrate no improvements or declines in crop production in a large fraction of studies.[73-75]

The enhanced fertility of soils historically amended with charcoal, such as Amazonian Terra Preta soils, can be partially attributed to improved cation exchange capacity (CEC).[76, 77]

CEC is a key indicator of soil fertility, buffering capacity, and water holding capacity.[78-80] However, many contemporary biochars have a low CEC (mostly below a typical soil CEC value of 15 cmol/kg) and weathering studies have demonstrated that natural surface oxygenation of biochar develops at decadal timescales.[81-83] Thus, the variability of crop response to biochar-amended soils may be attributed to their low CEC.[82, 84-88] Therefore, biochars with greater CECs are critically needed to achieve the mission of biochar as a soil amendment and carbon sequestration agent.[89-92]

While a high O:C ratio is desirable for high CEC [23], it must also be understood that the higher the O:C ratio, the shorter the overall half-life of biochar when placed in soils. Biochars with O:C ratios >0.2 have half-lives less than 1000 years in natural soil environments.[93] The expected half-lives drop precipitously to <100 years for an O:C ratio of ≥0.6. An ideally designed biochar for use as both a soil amendment and carbon sequestering agent would need to enhance the O:C ratio only on the surface of biochar [25], giving a higher CEC, while still maintaining the poly-aromaticity (preferably lower O:C ratio) of the biochar core to ensure long-term stability.

This article reports a technological solution that dramatically increases the CEC of biochars through surface oxygenation. The underlying concept is that an innovative application of post-production biochar ozonization (Figure 5) can cost-effectively create oxygen-containing functional groups on biochar surfaces that will substantially increase its CEC and improve its performance in agronomic and remediation applications.

According to our preliminary understanding [25, 94], the most significant reactions of O_3 with organic matter are likely based on the cleavage of the carbon double bond, which acts as a nucleophile having excess electrons. The injected O_3 stream may lead to the formation of carbonyl

and carboxyl groups on biochar surfaces by reacting with carbon-carbon (C=C) double bonds at ambient pressure and temperature:

$$\text{Biochar-CH=CH-Biochar} + O_3 \rightarrow \text{Biochar-COH} + \text{Biochar-COOH} \quad (1)$$

In this case, the ozonized biochar will become more hydrophilic since both carbonyl and carboxyl groups can attract water molecules. Because the carboxyl groups readily deprotonate in water and result in more negative charge on biochar surfaces, it will also increase the CEC:

$$\text{Biochar-COOH} \rightarrow \text{Biochar-COO}^- + H^+ \quad (2)$$

In a previous study [25], we tested this biochar ozonization process, and observed an increase in CEC value of the biochar by a factor of nearly 2. In the present study using a biochar material with high BET surface area, the use of ozonization resulted in a dramatic increase in biochar CEC to over 100 cmol/kg, which may represent a significant breakthrough in biochar science and technology. Further research was conducted on the toxicity of this ozone treated biochar to plant germination.

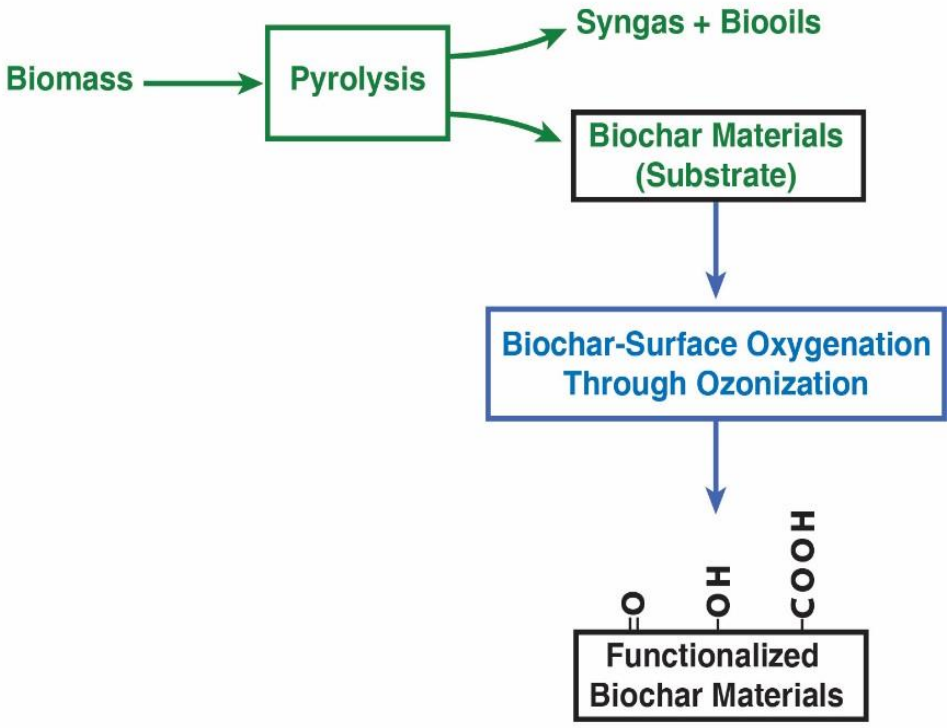

Figure 5. Schematic for post-production biochar ozonization to create oxygen containing functional groups on biochar surfaces. (Adapted from Ref 32)

MATERIALS AND METHODS

Characterization of Biochar

The Rogue Biochar used during the experiment was obtained from Oregon Biochar Solutions. The biochar was characterized by the International Biochar Initiative (IBI, Lab ID number 7020309-01). The characteristics of the Rogue biochar are represented in Table S1 of the supporting information.

Dry ozone treatment

The Rogue biochar obtained from Oregon Biochar Solutions was oven-dried overnight at 105 ^{o}C in an electric oven. The biochar was then grinded, sieved using a 106 µm sieve, washed with ultrapure water (100 mL per gram) and placed back in the oven at 105^{o}C overnight for drying. This biochar is represented by RBC UN in the paper. 1.5 g of the oven dried biochar was weighed and placed in an ozone treatment vessel. The ozone generator (Welsbach T-series) was set to optimum condition for the generation of ozone as described next. Briefly, the oxygen pressure was set to 8 psi and the flow of ozone was set to 3 L/min. The ozone gas stream was passed into the sample containing reactor vessel for a duration of 90 min. During the treatment, the sample reactor vessel was shaken in regular intervals of 15 min in order to treat every particle of biochar with ozone. After 90 min, the biochar was washed thoroughly in two steps with ultrapure water. The first rinse of 25.0 mL and the second rinse of 300 mL were both collected in vessels for subsequent dissolved organic carbon (DOC) determination. The washed biochar was then placed in the oven at 105 ^{o} C for drying. This biochar is represented by RBC 90D in the paper. Proportional amounts of ultrapure water were also used to rinse 3 g of RBC UN biochar, and filtrates were collected for subsequent DOC determination.

pH determination

The biochar pH was recorded with a Beckman Coulter Phi 570 pH meter connected to a Thermo Scientific Orion pH probe. To determine the pH of the biochar, three replicates of 1.0 g each of RBC UN and RBC 90D biochar were taken and placed into 50-mL centrifuge tubes with 10 mL of ultrapure water added to each tube. For the RBC 90D biochar, pH was determined both before and after the rinsing procedure described above, in order to determine the impact of the DOC component. The tubes with the mixture were then placed on a shaker Innova 2300 platform

shaker (New Brunswick Scientific, Eppendorf AG, Germany) and the shaker was set at 120 rpm for 1 hour. After shaking, the pH of the slurry of each sample was recorded.

CEC measurement using the AOAC method (at the ODU Laboratory)

To determine the CEC of the biochar, a similar approach with a modified protocol from AOAC method 973.09 as reported by Rippy et al. (2007) was used.[18] Briefly, six replicates of 0.5 g each of RBC UN and RBC 90D biochar were taken and each of the 0.5 g samples was placed into a 125 mL Erlenmeyer flask with 50 mL of 0.5 M hydrochloric acid (HCl) added to each flask. The flasks with the mixture were then placed on the shaker set at 120 rpm and were shaken for 2 hours. The mixture was then filtered and washed through Whatman ™ GF/F 70-mm glass microfiber filter with 100 mL portions of Millipore water until no precipitation was seen upon the addition of silver nitrate ($AgNO_3$) in the filtrate. The biochar residue was then transferred into a clean 125 mL Erlenmeyer flask along with the filter paper and 50 mL of 0.5 M barium acetate ($Ba(OAc)_2$) was added to each flask. The flasks with the mixture were again placed in the shaker set at 120 rpm for 2 hours. The mixture was then filtered and washed with 300 mL of Millipore water. The residue was discarded, whereas the filtrate was then titrated with 0.025 M sodium hydroxide (NaOH) solution until the end point was reached. The CEC was the calculated using the following equation:

$$\frac{cmol}{Kg\ biochar} = \frac{mL\ NaOH \times molarity\ NaOH\ \times 100}{gram\ sample} \qquad (3)$$

Independent CEC measurement using modified ammonium acetate (NH_4OAc) method (at the USDA/ARS Laboratory)

Samples of the biochars (RBC UN and RBC 90D) were sent to the USDA-ARS Laboratory for independent CEC measurements using an ammonium acetate (NH_4OAc) method (Graber et al., 2017) with modifications suggested by Munera-Echeverri et al. (2018).[95] Because CEC is pH-dependent, biochar samples were pretreated by adjusting the pH to 7. Briefly, 1 gram of dried biochar was mixed with 20 mL of deionized water and shaken horizontally for 4 hours at 200 rpm to ensure complete wetting. 1.5 M HCl (or NaOH) was used to adjust the pH of the slurry to 7. The pH was monitored periodically over 48 hours to ensure it had stabilized, and the water was removed by filtering through 2-μm filter paper (Whatman Nucleopore Track-Etch membrane). As a modification of Munera-Echeverri et al. (2018), extraction steps were performed using a filtration apparatus instead of a centrifuge, because the ozone-treated biochar did not form a translucent supernatant (see Section 2.6). A fresh 2-μm filter and Whatman glass funnel were prepared on a 250 mL Erlenmeyer flask. The pH-adjusted biochar sample and 20 mL of 1 M NH_4OAc were added to the funnel, swirled, and let to stand on the funnel for 2 hours before applying vacuum to remove the NH_4OAc. Repeated additions of 20 mL NH_4OAc were performed a total of 4 times. For the 4th addition, the NH_4OAc and biochar mixture was let to stand overnight before vacuuming. Next, repeated additions of 20 mL ethanol (EtOH 100%) were used to remove the non-complexed NH_4. EtOH was added to the funnel, swirled to mix with the biochar, and let stand for 2 hours before vacuuming. The EtOH wash was performed 4 times. The complexed NH_4 was then displaced with potassium chloride (KCl); 20 mL of 2 M KCl was added to the biochar sample, swirled, and allowed to stand for 2 hours, and then vacuum was applied to collect the filtrate in an Erlenmeyer flask. A total of 4 extractions were done, producing 80 mL of extracting volume.

Lastly, the ammonium was measured colorimetrically using a microplate reader (Ringuet et al., 2011), and CEC was calculated as follows:

$$CEC\ (cmol_c\ kg^{-1}) = \frac{NH_4^+\ conc.(mgL^{-1}) \times V(mL) \times 100}{molecular\ mass\ of\ NH_4^+ \times W(g)} \quad (4)$$

Triplicate samples of each biochar type were measured.

Surface area measurement with BET

The surface area was measured for the biochar samples before and after ozonization by using the Brunauer–Emmett–Teller (BET) nova 2000e series instrument. The biochar was weighted (about 0.1-0.3 g) and inserted into the sample cell. The biochar was then vacuum-degassed for 4 hours at 150 ^{o}C. Helium2000 at 10 psi was used for the backfill. The mass of the degassed biochar was then measured. For the analysis portion, the biochar samples were bathed on liquid nitrogen at 77 K and the nitrogen pressure was set to 10 psi. The multi-point BET technique was then used to obtain the surface area of the biochar samples. The surface area was measured for both the ground and sieved biochar samples (RBC UN and RBC 90D) as well as the unground biochar samples (RBC UN and RBC 90D) before and after ozonization. For a comparative analysis, the surface area was also measured for a non-ozonized ground and sieved biochar from slow pyrolysis (30 min) of pine wood biomass at 400 ^{o}C (P400). The same procedure as done for the RBC UN and RBC 90D was used for measuring the surface area of the P400 except that the backfill was done with the adsorbate (here nitrogen) instead of Helium. The reason for the change in the backfill gas was because the P400 being microporous the method using helium as a

backfill resulted in the inability of the nitrogen gas to adsorb and desorb on the surface, thus resulting in no measurable BET surface area. This may be due to possible entrapment of helium in the micropores of the biochar. To circumvent that limitation, nitrogen gas used as backfill instead of helium. In order to verify the validity of this method, the ground RBC UN and RBC 90D (before and after ozonization) had their surface area re-measured with nitrogen as the backfill gas.

Fourier-transform infrared (FTIR) spectroscopy

Biochar FT-IR spectroscopy was analyzed on a Nicolet 6700 FT-IR spectrometer from Thermo Scientific using a pellet. 1 mg of finely ground samples of RBC UN and RBC 90D biochar were mixed with 300 mg of pre-dried and ground FT-IR grade KBr. The FTIR spectra were recorded over the range of 400-4000 cm^{-1} with the resolution of 4 cm^{-1} and 64 scans per sample.

Dissolved organic carbon measurement

The dissolved organic carbon (DOC) concentration of the filtrates collected from the wash of the dry-ozonized biochar (RBC 90D) and the non-ozonized control biochar (RBC UN) was measured using a TOC-Analyzer (Shimadzu TOC-V CPH); the filtrates collection method was shown in section 1.2. Briefly, the DOC concentration was measured from the 1^{st} wash and the 2^{nd} wash collected from each biochar. The total amount of DOC in mg, extracted from the 1^{st} and 2^{nd} wash were combined and divided by the mass of biochar sample in order to get the mg of DOC per gram of biochar. Prior to the measurement, in order to exclude the non-dissolved organic materials, the solutions were filtered through a hydrophobic Polytetrafluoroethylene (PTFE) 0.2 µm filter (Millex-FG SLFG025LS). The samples were then diluted at two different concentrations and the DOC was measured.

X-ray photoelectron spectroscopy

Samples of untreated control biochar (RBC UN) and the dry-ozonized biochar (RBC 90D) were sent to the Department of Chemistry in Virginia Tech (Blacksburg, VA 24061) for X-ray Photoelectron Spectroscopy (XPS) analysis. The experimental method is as follows. XPS characterization was performed on a PHI VersaProbe III scanning XPS microscope using monochromatic Al K-alpha X-ray source (1486.6 eV). Spectra were acquired with 100 µm/100 W/20 kV X-ray and dual-beam charge neutralization over a 1400 µm × 100 µm area. All binding energies were referenced to C-C at 284.8 eV.

Survey: 280 eV Pass Energy, 1.0 eV/step, 50 ms/step, 10 sweeps;

C1s: 26 eV Pass Energy, 0.1 eV/step, 50 ms/step, 10 sweeps;

O1s: 26 eV Pass Energy, 0.1 eV/step, 50 ms/step, 30-40 sweeps;

Chemical states of elements were assigned based on the PHI and NIST XPS Databases.

Elemental Analysis (Oxygen and carbon)

The ground and sieved non-ozonized control biochar (RBC UN) and the dry-ozonized biochar (RBC 90D) samples were sent to the Kumar lab at ODU for Elemental Analysis. In the elemental analysis, the measured mass percentages of oxygen and carbon were converted to molar percentages by dividing the weight percent of each element with its molar mass. The molar O:C ratio was determined by dividing the molar percentages of O with that of C.

Scanning electron microscopy/Energy dispersive x-ray spectroscopy

Samples of untreated control biochar (RBC UN) and the dry-ozonized biochar (RBC 90D) were sent to the Nanoscale Characterization and Fabrication Laboratory in Virginia Tech (Blacksburg, VA 24061) for SEM/EDS analysis using an FEI Quanta 600 FEG environmental

scanning electron microscope and a Bruker QUANTAX 400 Energy Dispersive X-Ray Spectrometer.

Phytotoxicity of ozonized biochar

This test was performed with Phytotoxkit which consists of transparent test plates, reference soil, black filter paper, and test seeds. The monocotyl Sorgo (*Sorghum saccharatum*) and the dicotyl mustard (*Sinapis alba*) seeds were selected for the phytotoxicity assessment. The phytotoxicity of untreated control biochar (RBC UN) and the dry-ozonized biochar (RBC 90D) on the germination of these monocotyl and dicotyl seeds was investigated in a similar approach with a modified protocol from Tarnawski et al. (2018) [96] and the standard procedures described in Phytotoxkit.

The test plates are shallow and flat and have two compartments, the bottom of each of which was filled with one bag reference soil mixed homogeneously with biochar (1% and 2% by weight) and saturated with water using a syringe. The test was done in two replicates for each seed type in each category of soil/biochar mixture. Control plate was established with water saturated reference soil only. The reference soil's water holding capacity has been preestablished through experimentation. 35 mL of water must be added to a 90 cm^3 (one bag) soil to reach 100% water saturation. The wet soil of each test plate was spread out and flattened with spatulas to create a soil layer of uniform depth. One black filter paper was placed on top of the leveled wet soil in each plate so that the filter is completely wet. Ten (10) seeds of the same test plant were placed in a row on top of the filter paper, spaced equally apart and close to the central ridge of test plate. The plastic cover of the test plates was placed to close the test plates tightly. The test plates were set upright in cardboard holder and incubated in a cardboard box at 25 ^oC in darkness. The germination

of these plant species in these test plates were photographed on day 0, day 3, and day 5. The root and shoot length of both species on day 5 were recorded in millimeters using ImageJ.

Phytotoxicity of ozonized biochar filtrate

The phytotoxicity of ozonized biochar filtrate on the germination of seeds was investigated in a similar approach as with the phytotoxicity of biochar with a little improvement in the standard procedure. This test was performed with Phytotoxkit which consists of transparent test plates, foam pads, thick white filter paper, black filter paper, and test seeds. The dicotyls garden cress (*Lepidium sativum*) and mustard (*Sinapis alba*) seeds were selected for the phytotoxicity assessment.

Firstly, the "foam pad" was placed in the bottom compartments of each test plates (instead of filling with reference soil) and then the thick "white filter" paper was put on top of it with a "parafilm sheet" in between the foam pad and the white filter. The white filter paper is then completely saturated with 20 mL of test solution using a syringe. The parafilm sheet acts as an impermeable layer keeping the white filter completely saturated throughout the exposure period. The test was done in two replicates for each seed type for each DOC biochar filtrate concentration (0 ppm, 10 ppm, 100 ppm, 250 ppm, and 500 ppm). Control plate was established with white filter paper saturated with water. One black filter paper was placed on top of the white filter paper in each plate so that the filter is completely wet. Ten (10) seeds of the same test plant were placed in a row on top of the filter paper, spaced equally apart and close to the central ridge of test plate. The plastic cover of the test plates was placed to close the test plates tightly. The test plates were set upright in cardboard holder and incubated in a cardboard box at 25 ^{o}C in darkness. The germination of these plant species in these test plates were photographed on day 0, day 3, and day 5. The root and shoot length of both species on day 5 were recorded in millimeters using ImageJ.

RESULTS AND DISCUSSION

Effect of ozonization on biochar pH

The biochar pH drastically decreased as a result of the ozone treatment. The untreated control sample of biochar had a basic pH value of 9.82±0.03. After 90 min of dry-ozone treatment, the biochar pH dropped down to 3.07±0.03 (Table 1). The decrease in biochar pH is consistent with the understanding that biochar ozonization can create carboxylic acid groups on biochar surfaces, as demonstrated by FT-IR and XPS analyses (Sections 2.4 and 2.5, below). The carboxylic acid groups on biochar surfaces can deprotonate, displaying low pH characteristics as shown in Eq 2. To make sure that the acidic pH was not due to any water soluble organic carbon that may be present in the biochar sample after the ozone treatment, the ozonized biochar sample was washed with Millipore water (200 mL water per gram biochar), and the pH for the washed ozonized biochar was measured to be 3.19±0.02. Therefore, the bulk of acidifying functional groups upon ozonization were associated with the biochar surface and only a small portion were associated with a soluble component.

Effect of ozonization on Biochar CEC

Biochar cation exchange capacity (CEC) is a key property central to helping retain soil nutrients, reduce fertilizer runoff, and improve soil water retention. The present experimental study showed that the biochar ozonization can increase the biochar CEC value by a factor of 7-9. The CEC value of untreated biochar (control) was determined to be 17.02±0.63 cmol/kg using the AOAC $Ba(OAc)_2$ method. Upon 90 min of dry-ozone treatment, the biochar CEC increased to 152.08±4.06 cmol/kg (Table 1), which to the best of our knowledge represents the highest biochar CEC value experimentally reached so far.

This is a significant result since the improvement on biochar CEC value by ozonization is now far much more than that of our previous study [25] where we demonstrated the increase in the CEC value of biochars by a factor of 2 through ozonization of a pinewood-derived biochar produced by slow pyrolysis at 400 ^{o}C (P400).

The Biochar CEC was also independently measured by the USDA team using a somewhat different CEC assay method: the ammonium acetate (NH_4OAc) method following adjustment to pH 7. The measurement with this method also confirmed the dramatic increase in CEC upon ozonization of the biochar. As measured with the modified ammonium acetate (NH_4OAc) method, the CEC of the 90-minutes dry ozonized Rogue biochar (RBC 90D) was determined to be 109.09 ± 6.33 cmol/kg while that of the untreated Rogue biochar control (RBC UN) was measured to be 14.57 ±1.62 cmol/kg (Table 1). The independent measurement conducted at the USDA laboratory confirmed the same trend in the dramatically increasing in the biochar CEC effected by the ozone treatment. The Rogue biochar is known to have a high surface area. In order to further understand the high increase in cation exchange capacity following ozonization, the surface area was measured on the Rogue Biochar in comparison with that of the P400 biochar.

BET surface area

The ground and sieved Rogue biochar samples before ozone treatment (RBC UN) had a surface area of 418.3 m^2/g (± 17.7) as reported in Table 1. Compared to the P400 with a measured surface area of only 2.05m^2/g (±0.42) as seen in Table S4, the Rogue biochar presents a very large surface area; Rogue biochar surface area is 200 times greater than P400. We believe that the high surface area of the Rogue biochar may make the latter more favorable to interact with ozone molecules. Therefore, the major difference on biochar CEC improvement between our present and

previous studies [25] may be attributed to the difference in BET surface area between the P400 and the Rogue biochar.

Upon being ozonized, the ground and sieved Rogue biochar decreased in surface area to 229.2 m^2/g (± 6.9) as seen in Table 1. The drop in the measured surface area upon being ozonized may be due to two factors: 1) It is possible that the ozone is causing the destruction of the pores of the biochar; 2) It is also possible that such a drop in surface area measurement may be because of the oxygen-rich functional groups created in the micro/nanometer pores of the ozonized biochar. The method of BET surface area measurement uses non-polar nitrogen gas as the adsorbate. Therefore, these non-polar gases may be inadequate in terms of giving a true surface area when polar oxygen groups are obtruding the pores and/or coating the surface of the biochar.[97]

In addition, in order to see the effect of grinding and sieving on the biochar, the surface area was also measured before and after ozonization from the unground biochar materials. The unground non-ozonized biochar had a BET surface area of 377.4 (±22.2) m^2/g which is somewhat less than the ground non-ozonized biochar control. After ozonization, the measured BET surface area of the unground biochar was 332.1 (±17.8) m^2/g (Table S3). That is, the unground biochar samples also showed a slight drop in the measured surface area after ozonization. However, for the unground biochar samples, the drop in the surface area before and after ozonization is not as significant as it was observed for the ground biochar samples (Table 1). This may be due to the fact that the process of ozonization may have occurred more thoroughly on the ground biochar sample compared to the unground biochar sample.

Table 1. pH, CEC and BET surface area of the ground biochar before and after ozonization. The values are means ± SD from duplicates (n=2) of measurements for pH, 6 replicates (n=6) for CEC measured by $Ba(OAc)_2$, triplicates (n=3) for the CEC measured by NH_4-OAc, and 5 replicates (n=5) for the BET surface area measured with N_2 after a backfill with helium.

Parameters	**Non-ozonized Biochar (RBC UN)** (means ± SD)	**Dry-ozonized Biochar (RBC 90D)** (means ± SD)
pH	9.82 ± 0.03	3.07 ± 0.03
CEC (cmol/kg) measured by $Ba(OAc)_2$ method	17.02 ± 0.63	152.08 ± 4.06
CEC (cmol/kg) measured by NH_4-OAc method	14.57 ± 1.62	109.02 ± 6.33
BET Surface area (m^2/g)	418.3 ± 17.7	229.2 ± 6.9

FT-IR analysis of biochar

FT-IR technique was used for the identification and qualitative tracing of functional groups in biochar samples. Overall, FT-IR spectra showed a decrease in aromaticity and increase in carbonyl groups as a result of ozone treatment. Ozone treatment led to an increase in the relative intensity of a broad band centered at 3417 cm^{-1}, which was assigned for the overlap of the H-bonded O–H stretching vibrations of hydroxyl groups from alcohols, phenols, and organic acids and N–H stretching of amine. Bands at 2922 cm^{-1} and 3026 cm^{-1} assigned for alkyl and aromatic C–H stretching also increased in intensity after the ozone treatment (Figure 6). Bands at 1637 to 1616 cm^{-1} were assigned for aromatic and olefinic C=C vibrations, C=O in amide (I), ketone, and quinone groups and the relative intensity of this band increased after the ozone treatment (Figure

7), which could be due to the increase of the C=O functional groups after ozone treatment. The bands at 1540 to 1560 cm^{-1} in the RBC 90D sample were assigned for COO^- asymmetric stretching, which is absent in the RBC UN, and confirms that the extra C=O functional groups are added in the form of carboxylic acid. The relative intensity of several bands also decreased after the ozone treatment, including two bands at 1494 cm^{-1} and 1386 cm^{-1} that were assigned for N–O stretching, the band at 1451 cm^{-1} assigned for alkyl C–H bending, and three bands at 1115 cm^{-1}, 758 cm^{-1} and 471 cm^{-1} assigned for Si–O stretching and bending. The band at 669 cm^{-1}, which was only present in the RBC 90D, could be due to out of plane ring deformation (Figure 7).

XPS analysis of biochar

The atomic concentration percentages on biochar surfaces measured by X-ray Photoelectron Spectroscopy (XPS) revealed that the ozone treatment caused an increase of two-fold in the amount of oxygen present on the surface of the biochar (Table 2). The atomic percentages on the surface of the biochar were determined from the integrated intensity of the elemental photoemission features corrected by relative atomic sensitivity factors. The survey, C1s and O1s spectra for the untreated control biochar and the ozonized biochar are shown in Figures S2 and Figure S3. The ozone treatment caused an increase in total O concentration on the surface of the biochar from 13.93% to 23.70% (Table 2). The two-fold increase in the amount of oxygen was mostly seen in the form of organic C=O groups (e.g. carbonyl/carboxyl) and C-O (e.g. hydroxyl/ether) groups. The oxygen content in the form of C=O went from 7.44% for the untreated control biochar to 11.57% for the ozonized biochar. This measurement confirmed our prediction in the installment of the oxygen groups mostly in the form of carboxyl groups. The carboxyl groups observed by XPS here also explains the drop in pH that was shown in Table 1. The oxygen group installment

post ozone treatment was also seen in the form of C-O; the untreated control biochar had a C-O of 5.79% and it increased to 11.33% after ozone treatment (Table 2).

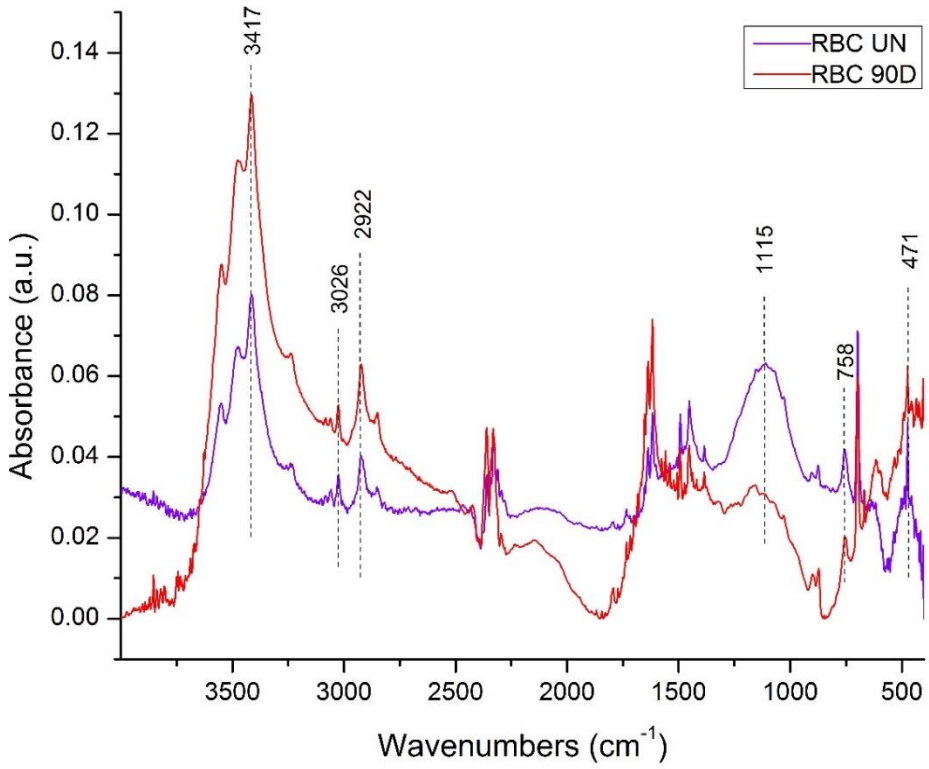

Figure 6. FT-IR spectra from 400-4000 cm^{-1} for 90-min dry ozonized Rogue biochar (RBC 90D) and the untreated Rogue biochar (RBC UN) control.

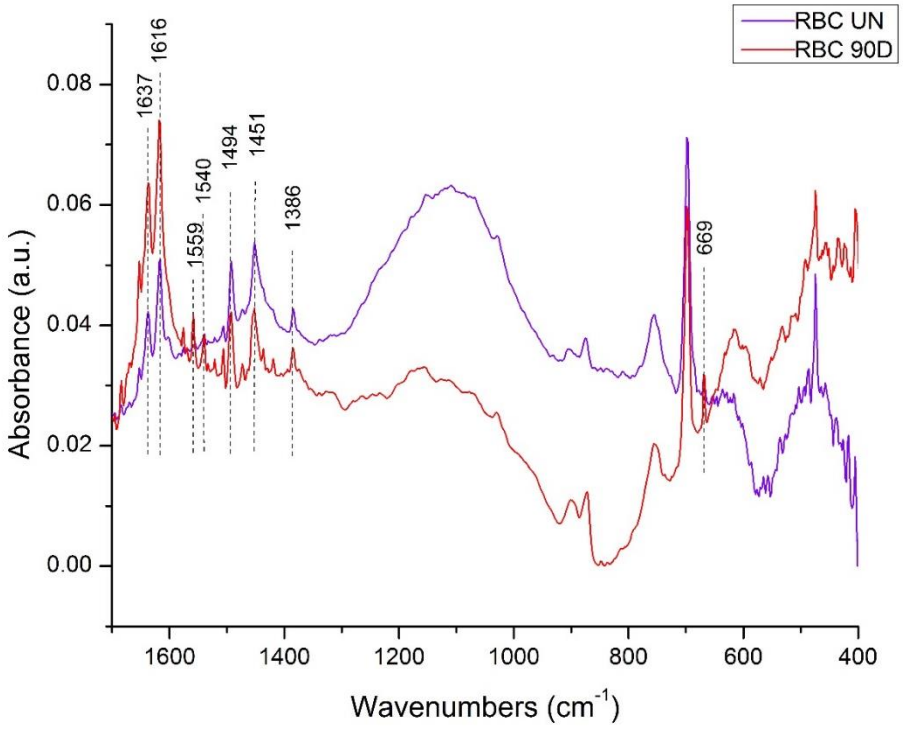

Figure 7. FT-IR spectra from 400-1700 cm^{-1} for 90-min dry ozonized Rogue biochar (RBC 90D) and the untreated Rogue biochar (RBC UN) control.

As a result, the formation of oxygen-functional groups including carboxylic acids on biochar surfaces have now, for the first time, been observed with XPS upon biochar surface oxygenation through the ozonization treatment. There is a strong correlation between the biochar oxygen-to-carbon (O/C) ratio and its CEC, due to the negative charge on oxygen functional groups electrostatically attracting cations from solution.[98, 99]

The data in Table 2 showed that the molar O/C ratio (23.70/76.30 = 0.31:1) on ozonized biochar surface is indeed significantly higher than that (13.93/86.07 = 0.16:1) of the control biochar surface. Therefore, biochar ozonization can indeed be used as a significant biochar surface oxygenation technique.

Table 2. Representation of the atomic concentration (in %) from XPS measurement. The atomic percentages represented here were determined from the integrated intensity of the elemental photoemission features corrected by relative atomic sensitivity factors. The survey and C1s/O1s spectra are shown in Figure S2 and S3. The data represented here were measured by the Department of Chemistry in Virginia Tech.

Sample								
Ozonized Biochar (RBC 90D)	**C**					**O**		
	76.30					23.70		
	sp^2 C	**sp^3 C**	**C-O**	**C=O**	**CO_3**	**C=O**	**C-O**	**H_2O**
	29.00	21.56	11.72	11.06	2.96	11.57	11.33	0.80
Control Biochar (RBC UN)	**C**					**O**		
	86.07					13.93		
	sp^2 C	**sp^3 C**	**C-O**	**C=O**	**CO_3**	**C=O**	**C-O**	**H_2O**
	38.80	27.75	8.98	6.32	4.22	7.44	5.79	0.70

SEM imaging and EDS analysis of ozonized biochar

Scanning electron microscopy (SEM) imaging (Figure 8) showed that the biochar material had little difference before and after the ozonization treatment. This observation indicated that the ozonization process indeed did not significantly alter the biochar bulk material appearance as we predicted.

As shown in Figure 8, both biochar samples are fragments of honeycomb-like bulk biochar structure, with particle size <100 μm. There is no noticeable difference in surface morphology between the RBC UN and RBC 90D. The large variations of particle shape, size and surface

orientation can be used to explain the insignificant changes in O/C ratios obtained by angle-resolved XPS.

The Energy-Dispersive X-Ray Spectroscopy (EDS) conducted during the SEM imaging showed that the mean O/C ratio value of the ozonized biochar material RBC 90D was 0.16:1, which is slightly higher than that (0.080:1) of the control biochar (RBC UN) as listed in Table 3. The EDS result, which provides "bulk" elemental composition with information depth of >1 μm, shows an increase of O/C ratio of 92.8% (from 0.080 to 0.16) after ozone treatment. This value is about the same as the 94% increase (from 0.16 to 0.31) on the biochar particle surfaces obtained by XPS, which is quite surprising in regarding to the biochar surface oxygenation by ozonization where we expected the effect of ozonization to be noticeable only on the first molecular layer (likely within a few nanometers) of the biochar material surface.

Table 3. SEM-EDS analysis result of ozonized biochar and control biochar. The numbers represent mean values (±SD) of 20 replicates (n=20) for the control biochar (RBC UN) and 20 replicates (n=20) for the ozonized biochar (RBC 90D).

Sample	**C**	**O**	**O/C**
Control biochar (RBC UN)	92.26 (±1.36)	7.74 (±1.36)	0.080 (±0.020)
Ozonized biochar (RBC 90D)	86.35 (±5.21)	13.65 (±5.21)	0.16 (±0.07)

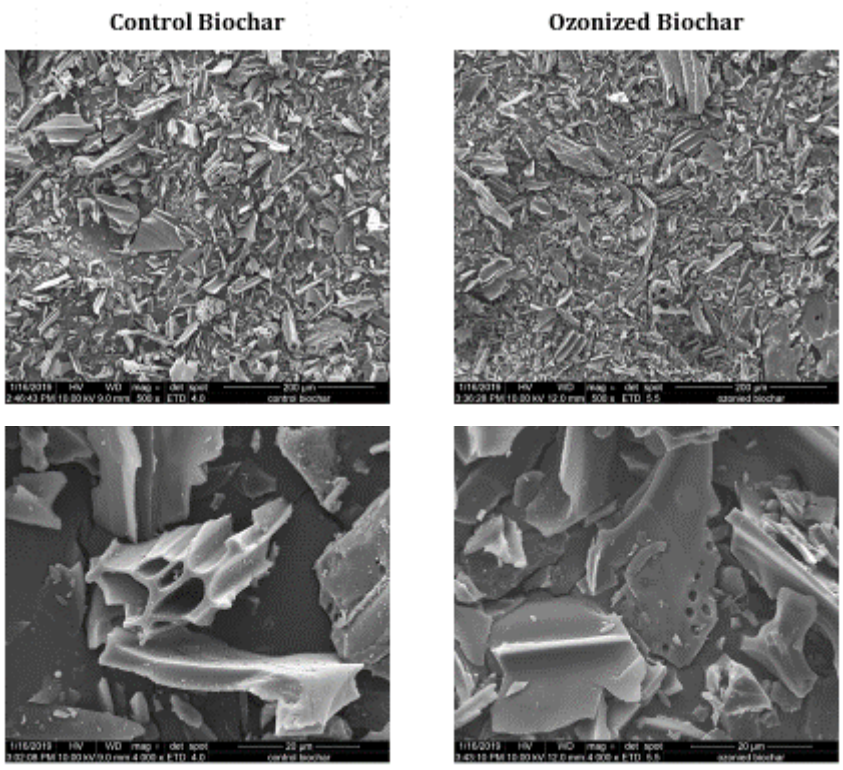

Figure 8. SEM images of the control biochar RBC UN (left) and ozonized biochar RBC 90D (right). (Adapted from Ref 32)

When the specific biochar material RBC UN used in the study is considered, with such a high BET surface area (418.3 ± 17.7 m^2/g), it is so porous at the molecular scales that its averaged carbon material thickness between the porous spaces is only about 5 nm. When such a thin (5 nm) piece of biochar carbon material is oxygenated at its two surface sides by ozone molecules, the resulting surface-oxygenated biochar carbon product may no longer be distinguishable by comparing the XPS and EDS measurements on O:C ratio. For example, assuming the thickness of ozonization-enabled biochar surface-oxygenation layer is about 1 nm, it would result in a surface-oxygenated biochar product with a structure of "oxygenated surface layer (1 nm) - biochar carbon

layer (3 nm) - oxygenated surface layer (1 nm)" that could no longer be distinguishable by the XPS and EDS measurements on the O:C ratio since the XPS measuring depth could be up to 10 nm. Therefore, the XPS data (Table 2) and EDS data (Table 3) both showing a doubling of O/C ratio in the RBC 90D sample is still consistent with the understanding that the ozonization process enables oxygenation at the first molecular layer (likely within a few nanometers) of the biochar material surface.

Dissolved organic carbon

Ozone treatment resulted in a low pH within its slurry as reported in Table 1. We think that the process of ozonization results in the breaking of C=C double bonds on the biochar material (Huff et al. 2018).[25] Following that breaking, there should be organic carbon fragments of biochar with carboxylic groups "Biochar-COOH" (Huff et al. 2018).[25] In order to further test the efficiency of ozone treatment on our biochar, and to verify the formation of those "Biochar-COOH" fragments, the filtrate of the wash of the biochar was collected before and after ozonization for dissolved organic carbon concentration measurement. The effect of ozonization on the biochar was seen on the color of the filtrate extracted from the biochar. The filtrate from the non-ozonized biochar appeared clear while the filtrate of the dry-ozonized biochar appeared dark brown thus indicating more presence of organic carbon fragments (Figure S1). The total extracted DOC from the dry-ozonized biochar was 10.98 (±1.00) mg DOC/g biochar whereas the non-ozonized biochar control only resulted in 2.10 (±0.23) mg DOC/g biochar as observed in Table 4. Ozonization leads to a high amount of dissolved organic carbon in its filtrate which is due to the high oxygenation occurring on its surface leading to a breaking of the C=C double bonds.

This result demonstrated that biochar ozonization can also produce certain amount of oxygenated biochar molecular fragments, which may be solubilized by liquid water as DOC for

certain special applications such as to help unlocking phosphorous from insoluble phosphate materials in soils.[100]

Table 4. Amount of DOC material extracted from the non-ozonized control biochar and the dry-ozonized biochar. The values are means ± SD (n =2).

Biochar Sample	**DOC from Biochar (mg DOC/g biochar)**
Non-ozonized biochar control RBC UN	2.10 (±0.23)
Dry-ozonized biochar RBC 90D	10.98 (±1.00)

Elemental analysis

In an attempt to have a characterization of the elemental atomic content of the Rogue biochar before and after ozonization, elemental analysis was performed. Prior to ozonization, the biochar had a high content of carbon (87.022 mol % ±5.676) as reported in Table 5). Following ozonization, the carbon content dropped to 72.229 mol % (±0.912). In addition, following ozonization, there was a significant increase in oxygen content; the non-ozonized control had 6.669 mol % (±1.301) of oxygen whereas the ozonized sample had 13.926 mol % (±1.590) of oxygen. The mole percentages of carbon and oxygen were used to calculate the molar O:C. The ozonization process increased the molar O:C ratio by a factor of 2.5; the non-ozonized control had a molar O:C ratio of 0.077 whereas the dry-ozonized sample had a molar O:C ratio of 0.193 (Table 5). Ozone treatment changed the molar percentages of oxygen and carbon in the Rogue biochar. Even though we didn't expect the bulk properties of the biochar to be affected by ozone treatment, those results

suggest that dry-ozone treatment may have altered the overall oxygen content of the biochar, as we observed with the SEM-EDS data (Table 3) In support of our theory that ozonization mostly happens on the surface of the biochar we wanted to compare the changes in bulk properties before and after ozonization of a high surface area biochar (Rogue Biochar) and a lower surface area biochar. Previously in our lab using P400 biochar, Huff et al. (2018) [9] demonstrated that the bulk properties of the biochar didn't vary as much following ozonization as we believe that the ozonization mechanism happens on the surface of biochar. In an attempt to explain this change in bulk properties, we measured the surface area of P400; we found that P400 is a low surface area biochar with only 2.05 m^2/g (±0.42) compared to the Rogue biochar as reported in Table S4. Therefore, we believe that the total oxygen groups installed on the surface of the Rogue biochar may be significant enough to slightly change the overall percentage of oxygen within the whole biochar sample.

Table 5. Elemental analysis (oxygen and carbon) on the non-ozonized and dry-ozonized Rogue biochar samples. The values are moles average percentages from 6 replicates ± SD. The weight percent of each element was converted to mole percent by using the respective molar mass of each element. The O:C mol ratio was calculated from the averages of moles percentages of O and C.

	Non-ozonized Biochar (RBC UN)	Dry-ozonized Biochar (RBC 90D)
Oxygen mol % (± SD)	6.669 (±1.301)	13.926 (±1.590)
Carbon mol % (± SD)	87.022 (±5.676)	72.229 (±0.912)
O:C mol ratio	0.077	0.193

Phytotoxicity study of ozonized biochar and its DOC filtrate

The results on phytotoxicity of the biochar and its DOC filtrate was determined by comparing the length of roots and shoots of the seedlings grown in various biochar and DOC filtrate concentrations. Ozone treated biochar did not show any decrease and/or absence of germination of plant species after 5 days of exposure. Rather, with the proper concentration of biochar added, rogue biochar seems to stimulate the seed germination as seen in the monocotyl Sorgo (*Sorghum saccharatum*) and the dicotyl mustard (*Sinapis alba*). Ozone treated biochar filtrate however, when applied in a high concentration, may show some decrease and/or absence of germination of some plant species as seen in dicotyl garden cress (*Lepidium sativum*) seeds after 5 days of exposure. While there was no obvious trend in the root and shoot growth (Figure 9, Figure 10, Table 6, and Table 7), ozonized biochar along with its filtrate with DOC concentrations upto 100 ppm proved to be beneficial during the germination.

Table 6. Germination data for the monocotyl Sorgo (*Sorghum saccharatum*) and the dicotyl mustard (*Sinapis alba*) in soil mixed with different biochar concentrations.

	Sorghum saccharatum		*Sinapis alba*	
	Root (mm)	Shoot (mm)	Root (mm)	Shoot (mm)
Control	70.3 (±5.1)	38.9 (±6.2)	75.7 (±8.1)	57.5 (±7.1)
RBC UN (1%)	73.8 (±4.3)	43.8 (±5.5)	92.6 (±5.4)	76.2 (±9.5)
RBC UN (2%)	74.1 (±9.7)	39.0 (±7.1)	86.2 (±4.8)	80.8 (±8.6)
RBC 90D (1%)	85.1 (±6.8)	59.1 (±4.5)	79.3 (±7.2)	73.1 (±9.3)
RBC 90D (2%)	72.5 (±8.5)	40.6 (±6.3)	95.3 (±5.7)	64.3 (±4.4)

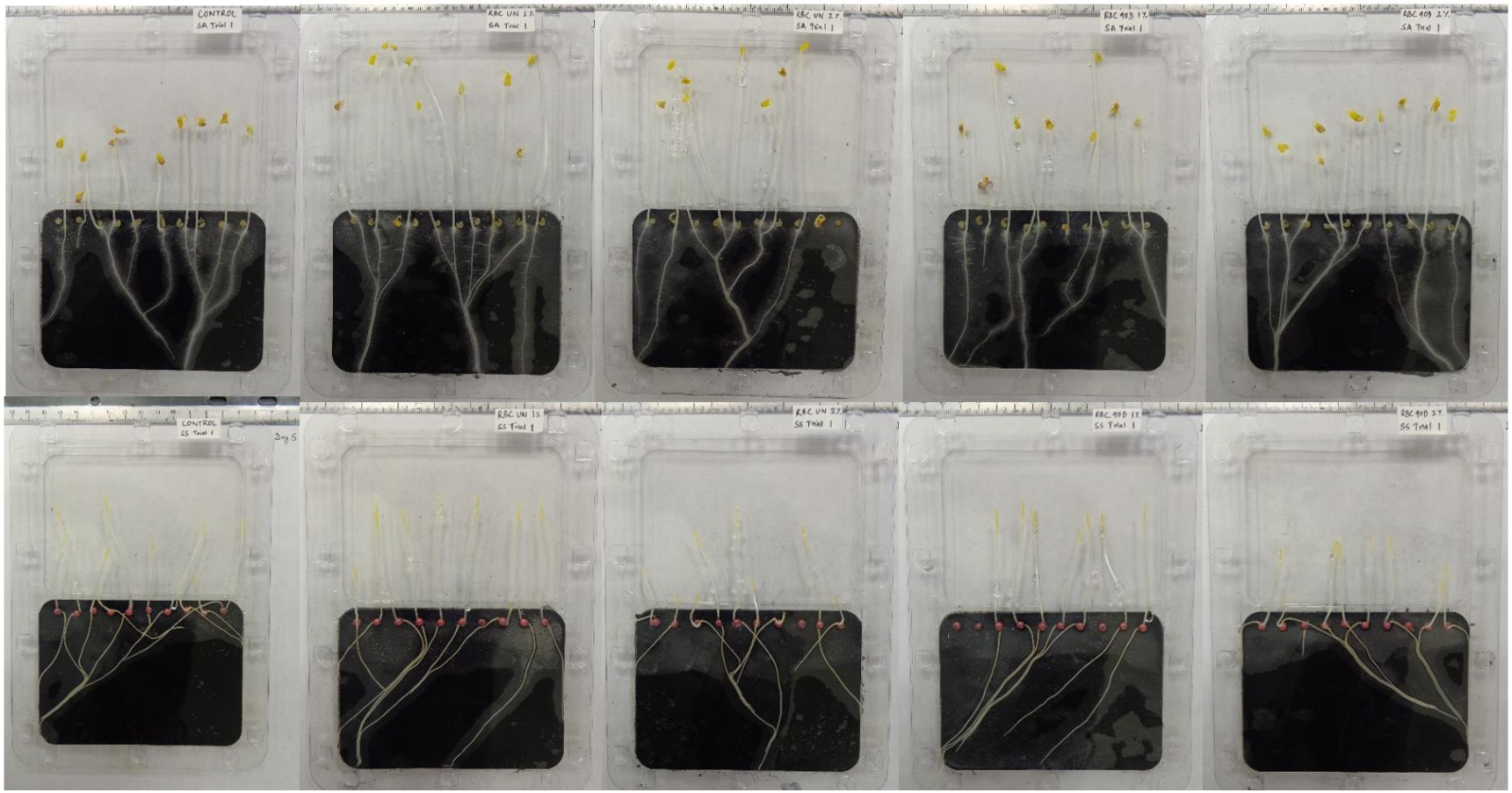

Figure 9. Images of the test plates for phytotoxicity study of ozone treated biochar taken after 5 days of exposure of seeds of monocotyl Sorgo (*Sorghum saccharatum*) and the dicotyl mustard (*Sinapis alba*) to soil mixed with various biochar concentrations.

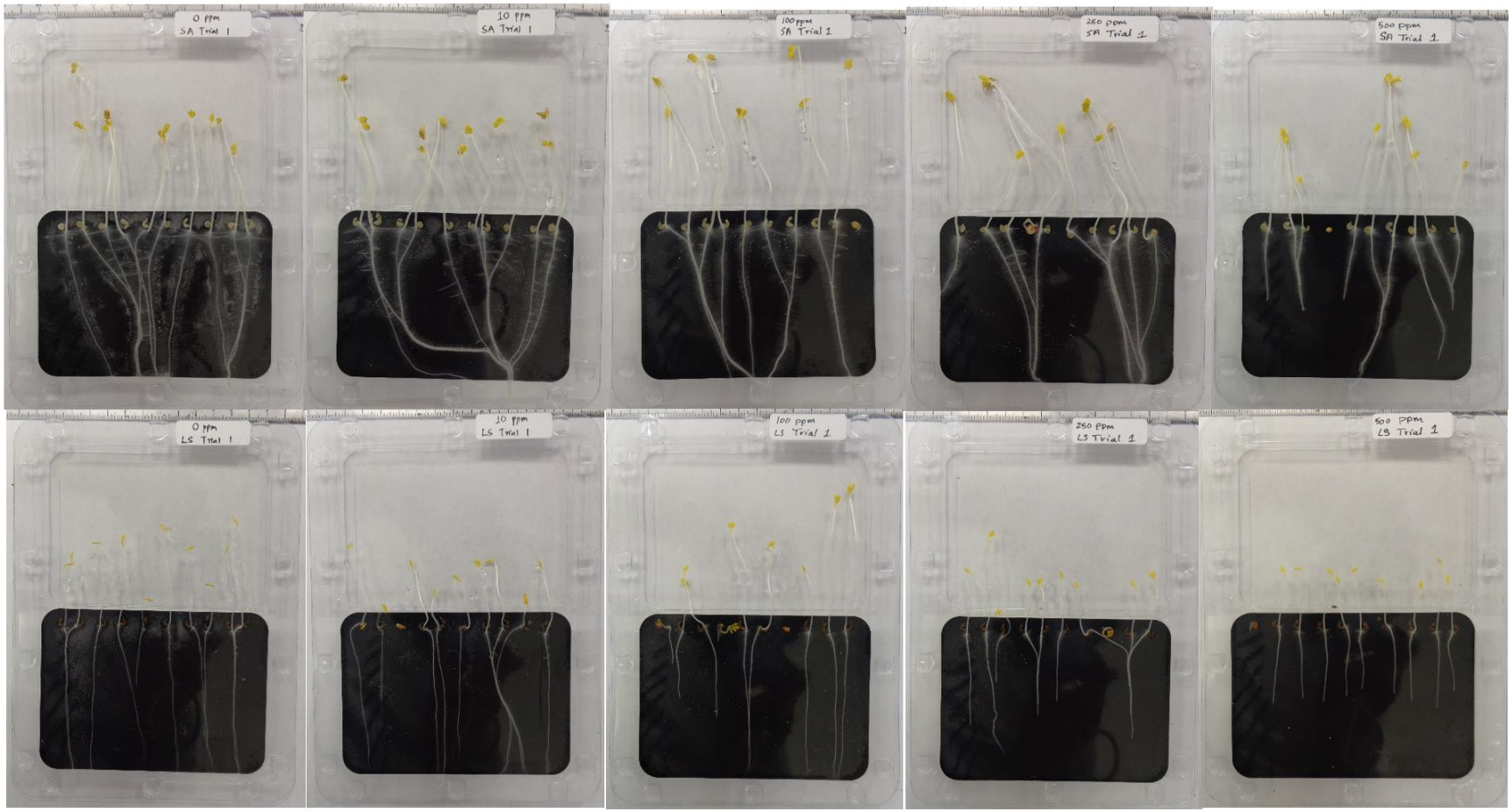

Figure 10. Images of the test plates for phytotoxicity study of various concentration of ozone treated biochar DOC filtrate taken after 5 days of exposure of seeds of the dicotyls garden cress (*Lepidium sativum*) and mustard (*Sinapis alba*).

Table 7. Germination data for the dicotyls garden cress (*Lepidium sativum*) and mustard (*Sinapis alba*) in various DOC biochar filtrate concentration.

DOC concentration	*Lepidium sativum*		*Sinapis alba*	
	Root (mm)	Shoot (mm)	Root (mm)	Shoot (mm)
0 ppm	84.0 (±5.3)	39.7 (±4.3)	92.9 (±5.8)	59.9 (±6.2)
10 ppm	77.6 (±6.2)	31.1 (±5.4)	108.0 (±6.5)	58.1 (±5.7)
100 ppm	67.2 (±8.6)	44.6 (±6.3)	91.2 (±4.2)	74.7 (±7.3)
250 ppm	45.4 (±6.5)	26.8 (±4.6)	87.7 (±5.6)	62.8 (±7.6)
500 ppm	48.7 (±3.5)	23.2 (±2.8)	50.6 (±7.8)	47.2 (±6.5)

Comparison of surface oxygenation methods

The ozone treatment described here has promising advantages over previous work to enhance biochar CEC, particularly when applied to biochars with high surface areas. Prior approaches have included treatment with concentrated hydrogen peroxide, which resulted in a doubling of CEC (Huff and Lee, 2016) [24]; air oxidation of biochar surface at 250 ^{o}C after pyrolysis also increased CEC by no more than a factor of two (Suliman et al., 2016) [101]; previous applications of ozone achieved a similar magnitude of CEC increase. For instance, Smith et al. (2015) [102] reported CEC increases of up to just about 20 and 7 cmol kg^{-1} for biochars produced from 500 ^{o}C pyrolysis of Douglas fir bark (DFBC) and Douglas fir wood (DFWC), respectively. Our previous study [25] demonstrated the increase in CEC value of a pinewood-derived (P400) biochar through an ozone treatment from 15.39 cmol kg^{-1} (± 1.59) to 32.69 cmol kg^{-1} (± 2.51), which is

approximately 1/4th of the increase reported here. In addition to our effort in optimizing the biochar ozonization process, the major factor that contributed to the present success in producing such a super high cation exchange capacity biochar (109~152 cmol/kg) appeared to be the special characteristics of the Rogue Biochar with its BET surface area of over 400 m^2/g (Table 1); whereas the P400 biochar used in our previous study [25] had a BET surface area of only about 2.05 (±0.42) m^2/g (Table S4). The large surface area of the Rogue Biochar seems to be beneficial to its interaction with ozone molecules for surface oxygenation to achieve dramatic increase in biochar CEC value.

CONCLUSION

Through this experimental study, we have now demonstrated a dramatic improvement of biochar CEC value by a factor of 7.5 through biochar surface oxygenation by ozonization. The CEC value of the untreated biochar was measured to be anywhere between 14 and 17 cmol/kg. A 90-minutes dry ozonization treatment resulted in a dramatically increased biochar CEC value of 109 ~ 152 cmol/kg, which is comparable to that of certain humic materials such as humins [103-108]. Simultaneously, the biochar ozonization process resulted in dramatic reduction of biochar pH from 9.82 to as low as 3.07, indicating the formation of oxygen-functional groups including carboxylic acids on biochar surfaces. Using the techniques of X-ray photoelectron spectroscopy, the formation of oxygen-functional groups including carboxylic acids on biochar surfaces have now, for the first time, been observed upon biochar surface oxygenation through the ozonization treatment. The molar O:C ratio (23.70/76.30 = 0.31:1) on ozonized biochar surface as analyzed by XPS is indeed significantly higher than that (13.93/86.07 = 0.16:1) of the control biochar surface. Similarly, the elemental analysis data showed a dramatic increase in O:C mol ratio from the control biochar (0.077) to the dry-ozonized biochar (0.193). The surface area measurements showed a

dramatic decrease in surface area following ozone treatment with values of 418.3 $m^2/g \pm 17.7$ (for the non-ozonized control biochar) and 229.2 $m^2/g \pm 6.9$ (for the dry-ozonized biochar). FTIR analysis also showed an increase in the content of oxygen-functional groups in the form of carbonyl groups on biochar surfaces upon ozonization, which can also produce certain amount of oxygenated biochar molecular fragments. This high CEC biochar show no signs of phytotoxicity for the germination of seeds. Furthermore, these oxygenated biochar molecular fragments may be solubilized by liquid water for greater effects upon the application of biochar in soil as it seems to stimulate the seed germination in some plant species.

CHAPTER 3

SOLUBILIZATION OF PHOSPHORUS FROM SOIL USING OZONIZED BIOCHAR AND PHYTOTOXICITY STUDY OF THE OZONIZED BIOCHAR FILTRATE

INTRODUCTION

Phosphorus (P), along with potassium and nitrogen is an essential element for life and plays a critical role in many biological processes. However, it is a finite resource, and its availability is limited as it is almost entirely mined as phosphate rock. Phosphorus is the most underestimated element for feeding the world with food production contributing to around 90% of the world's phosphorus needs.[109-111] Phosphorus scarcity has similarities to water scarcity and peak oil but only few people outside the farming and fertilizer industry fully understand the importance of phosphorus. The issue of peak phosphorus and the potential threats of global phosphorus limitation have been subjects of significant discussion and research in recent years. The question of whether there will be a true physical shortage of phosphorus in rock reserves in the upcoming decades or if there will be limitations due to economic and technical factors has generated controversy recently with reports predicting that chemical P fertilizer will be required globally to maintain agricultural and grassland productivity.[112, 113] Predictions suggest that the demand for phosphorus will surpass the supply of known phosphate rock reserves soon. Phosphate rock reserves are highly geographically concentrated, with significant deposits in Morocco, Moroccan-occupied Western Sahara, China, and the US. The geopolitical distribution of phosphate rock reserves may lead to increased tensions, as seen in regions like Western Sahara and Morocco.[114-118] The scarcity of

phosphorus poses significant challenges to global food security, and its geopolitical and environmental inferences highlight the need for sustainable practices and increased awareness of this vital resource. Furthermore, the concentration of reserves in specific regions adds complexity to the situation, requiring international cooperation to ensure fair access and avoid potential conflicts.[34, 119] While there is ongoing debate about the timing and nature of peak phosphorus, it is widely recognized that sustainable phosphorus management practices and a diversified approach to sourcing phosphorus are critical for ensuring long-term agricultural productivity and environmental health. Phosphorus sustainability is therefore crucial to meeting the needs of the growing global population and protecting the environment.[120, 121] Phosphorus is used extensively in agriculture, industry, and other sectors, and its demand is expected to increase significantly in the coming decades. However, the current production and use of phosphorus are often inefficient and wasteful, leading to environmental pollution and depletion of this resource. Therefore, improving the sustainability of phosphorus is essential for ensuring its availability for future generations and minimizing its impact on the environment.[41, 122]

Biochar, as a carbon-rich material produced through thermochemical conversion of biomass, has been the subject of research for its effects on physical and chemical properties of the soil.[123-127] These studies shows that the effect of biochar on phosphorus availability depends on factors such as biochar feedstock type, pyrolysis temperature, and soil properties. The characteristics of biochar, such as surface area, pH, phosphorus content, and cation exchange capacity (CEC), are important factors in determining its impact on soil phosphorus. Biochar can improve the phosphorus availability in soil indirectly by altering the physical and chemical properties of the soil such as pH, CEC, organic carbon pool, water-holding capacity, and surface properties of soil particle.[41, 128] Furthermore, biochar in soil can serve as a direct source of

accessible phosphorus or as an adsorbent for phosphates. Biochar may release negatively charged organic molecules that compete with phosphate ions for exchange sites in the soil colloids influencing the adsorption–desorption processes that results in the precipitation–dissolution of phosphate ions.[129] Modified biochar has recently been used as a slow-release phosphorus fertilizer.[130-136] Dissolved organic matter, often measured as dissolved organic carbon (DOC), is frequently studied in soil science.[137, 138] Investigating biochar DOC within different biochar types can be valuable for understanding trends in regions with diverse soil compositions. DOC is a complex organic mixture that mostly contains small molecular compounds such as amino acids, sugars, and organic acids as well as some macromolecular compounds which can influence the adsorption–desorption of phosphates through functional groups. Phosphorus is present in the soil in various mineral forms such as apatite, rock-phosphate, and phosphorite. Although the mineralization of phosphorus in soil from organic sources has been extensively studied, less is known about the mobilization of phosphorus from inorganic phosphorus pools, a process known as phosphorus solubilization.

There are several strategies for promoting phosphorus sustainability, including improving the efficiency of phosphorus use, recycling and reuse of phosphorus-containing wastes, recovery of phosphorus from natural sources, and raising public awareness about the importance of phosphorus sustainability. These strategies require multidisciplinary approaches that involve collaboration between different areas and participants.[34] Despite the challenges, there are many opportunities for innovation and collaboration in promoting phosphorus sustainability. New technologies, policies, and practices are being developed and implemented to reduce phosphorus waste, improve efficiency, and promote responsible use of this resource. Because of all these factors, we intend to explore the current state of phosphorus sustainability and the challenges and

opportunities for promoting sustainable phosphorus use.[139] A recent study reports a breakthrough process for surface oxygenation of biochar by ozonization to increase its CEC value to 109 – 152 cmol/kg. This process leads to release a high amount of organic acids (11 mg DOC/g) in the ozonized biochar extract which is a potential candidate for P solubilization.[32] Other study shows that phosphate can be dissolved from insoluble phosphate compounds like hydroxyapatite by mixing it in water with ozonized biochar.[50]

Here, we propose an improvement in phosphorus solubilization in different soil types by the use of ozonized biochar and its water filtrate. Further research was conducted on the toxicity of the used biochar and its dissolved organic carbon fragments on seed germination. This study provides a valuable step towards phosphorus sustainability which is a pressing issue for long-term agricultural and environmental well-being.

MATERIALS AND METHODS

All the chemicals used during this study were obtained from Sigma-Aldrich or Fisher. Solvents used were of analytical grade. Ultrapure water was used during all the purpose. Pyrolysis of the Pinewood was conducted in 500 mL hastelloy autoclave high pressure Parr reactor controlled by Parr 4848 reactor controller. Ozone was generated by Welsbach T-series ozone generator. Sonication was conducted with a 750 Watt, 20 KHz Ultrasonic Processor VCX-750. Centrifuge was done in a Beckman Coulter Avanti® J-26 XP centrifuge. pH was recorded in a Beckman Coulter Phi 570 pH meter connected to a Thermo Scientific Orion pH probe. Shaking of the biochar assays was done in an Innova 2300 Platform Shaker. Ion chromatography spectra were recorded on a Dionex ICS-5000 Ion Chromatography system. Dionex IonPac AS23 anion-exchange column (2×250 mm) was used during the analysis.

Production of Biochar

This method was adapted from Huff et al. (2016).[24] The pine wood biochar used during the experiment was produced from wood biomass from Loblolly pine trees (Pinus taeda) found on the Old Dominion University campus in Norfolk, Virginia. The bark was removed, and the pine woods were cut into tiny chips. The wood was then dried in an electrical oven at 105 °C overnight. 50 g of the pine wood biomass was placed on a Hastelloy Parr 0.5 L autoclave high pressure Parr reactor controlled by Parr 4848 reactor controller. Pyrolysis was conducted at atmospheric pressure. An outlet was made to prevent autogenic pressure buildup. The reaction chamber was purged with nitrogen for 5 min, and the biomass was slowly heated to 400 °C while collecting the bio-oil via the outlet. It was maintained at 400 °C for 30 min before slowly cooling it down using the internal water coil cooling system. For this study, a total of six batches of pinewood biochar were made. The average heating rate was 6.88 ± 1.87 °C/min. The average yield of biochar produced was 16.95 g (34 %). The collected biochar was ground and sieved through a 106 μm sieve, washed with ultrapure water (100 mL per gram). The biochar was then dried in the oven overnight at 105 °C. The biochar was collected and named as "P400". The Rogue biochar used during the experiment was obtained from Oregon Biochar solutions. It was ground, sieved, washed, and dried as described above before using it in the study. This biochar was named as "RBC".

Soils and phosphate rock used in the experiment

1. Western phosphate rock SRM 694 from National Institute of Standard and Technology (NIST)
2. Portneuf Soil or P-Soil from South Central Idaho sent by Dr Ippolito
3. Bennett Soil or B-Soil from Eastern Colorado sent by Dr Ippolito

Biochar ozonization treatment

This method was adapted from Sacko et al. (2020).[50]

Wet biochar ozonization treatment

1.5 g of oven dried biochar was weighed and placed in an ozone treatment vessel and 25.0 mL of ultrapure water was added to it. The ozone generator was set to optimum condition (ozone-containing gas flow was set to 3.0 L/min with the oxygen gas pressure set to 8 psi and the voltage of the ozone generator set to 116 V) for the generation of ozone. The ozone was bubbled into the sample mixture for complete 90 min. After 90 min, the mixture was transferred into a Buchner funnel filtration system setup using a Fisherbrand P8 filter paper, and the filtrate was collected in a vessel and stored at 4 °C for further analysis. The biochar was then washed with 300 mL of ultrapure water and kept in oven maintained at 105 °C for drying. This wet ozone treated pinewood biochar is represented by P400 90W and rogue biochar is represented by RBC 90W in rest of the paper.

Dry biochar ozonization treatment

1.5 g of oven dried biochar was weighed and placed in an ozone treatment vessel. The ozone generator was set to optimum condition for the generation of ozone. The ozone was passed into the sample containing vessel for complete 90 min. During the treatment, the sample vessel was shaken in a regular interval of 15 min to treat every particle of biochar with ozone. After 90 min, the biochar was washed thoroughly using Buchner funnel with 25 mL of ultrapure water which was collected in a vessel and stored at 4 °C for further analysis. The biochar was then washed with additional 300 mL of ultrapure water and kept in oven maintained at 105 °C for drying. This dry ozone treated pinewood biochar is represented by P400 90D and rogue biochar is represented by RBC 90D in rest of the paper.

Sonication and wet ozone treatment of pinewood biochar

3.0 g of oven dried P400 biochar was weighed and placed in an ozone treatment vessel and 50.0 mL of ultrapure water was added to it. The sample mixture was sonicated for 15 minutes with the Ultrasonic Processor set at 50% amplitude. The ozone generator was set to optimum condition for the generation of ozone. The ozone was bubbled into the sample mixture for 45 minutes. After that, the sample mixture was sonicated again for 15 minutes. Then, ozone was bubbled into the sample mixture for next 45 minutes. The mixture was then transferred into a Buchner funnel filtration system setup using a Fisherbrand P8 filter paper, and the filtrate was collected in a vessel and stored at 4 °C for further analysis. The biochar was then washed with 600 mL of ultrapure water and kept in oven maintained at 105 °C for drying. This biochar is represented by P400 90W+S in rest of the paper.

Control biochar

1.5 g of oven dried biochar was washed thoroughly using Buchner funnel with 25 mL of ultrapure water which was collected in a vessel and stored at 4 °C for further analysis. The biochar was then washed with additional 300 mL of ultrapure water and kept in oven maintained at 105 °C for drying. This untreated pinewood biochar is represented by P400 UN and rogue biochar is represented by RBC UN in rest of the paper.

pH measurement

This method was adapted from Sacko et al. (2020).[50] For each of the untreated control, dry ozone treated, and wet ozone treated pinewood and rogue biochar, three replicates of 1.0 g each were taken and placed into 50-mL centrifuge tubes with 10 mL of ultrapure water added to each tube. The tubes were then shaken on an Innova 2300 Platform Shaker at 120 RPM for 1 hour. The

pH of the mixture was then measured with a Beckman Coulter Phi 570 pH meter connected to a Thermo Scientific Orion pH probe.

Cation exchange capacity (CEC) measurement

This method was adapted from Rippy et al. (2020).[18] Briefly, three replicates of 0.5 g each of RBC UN, P400 UN, RBC 90D, P400 90D, RBC 90W, and P400 90W biochar were placed into a 125 mL Erlenmeyer flask with 50 mL of 0.5 M hydrochloric acid (HCl) added to each flask. The flasks with the mixture were were shaken on an Innova 2300 Platform Shaker at 120 RPM for 2 hours. The mixture was then filtered and washed through a Buchner funnel filtration system setup using a Fisherbrand P8 filter paper with 100 mL portions of ultrapure water until no precipitation was seen upon the addition of silver nitrate ($AgNO_3$) in the filtrate. The biochar residue was then transferred into a clean 125 mL Erlenmeyer flask along with the filter paper and 50 mL of 0.5 M barium acetate ($Ba(OAc)_2$) was added to each flask. The flasks with the mixture were again placed in the shaker set at 120 rpm for 2 hours. The mixture was then filtered and washed with 300 mL of Millipore water. The residue was discarded, whereas the filtrate was then titrated with 0.025 M sodium hydroxide (NaOH) solution until the end point was reached. The CEC was the calculated using equation 3 as mentioned in previous chapter:

$$\frac{cmol}{Kg\ biochar} = \frac{mL\ NaOH \times molarity\ NaOH\ \times 100}{gram\ sample} \qquad (3)$$

Dissolved organic carbon (DOC) measurement

This method was adapted from Kharel et al. (2019).[32] The filtrates collected from each of the untreated control, dry ozone treated, and wet ozone treated pinewood and rogue biochar was filtered through a hydrophobic polytetrafluoroethylene (PTFE) 0.2 μm filter (Millex-FG SLFG025LS). The filtrate liquid was collected and referred to as untreated, dry-ozonized, and wet-ozonized biochar filtrate, respectively. The dissolved organic carbon (DOC) concentrations of the biochar filtrate that was filtered through 0.2 μm filter was measured using a TOC-Analyzer (Shimadzu TOC-V CPH). The total amount of DOC in mg, extracted from the filtrate was divided by the mass of biochar sample in order to get the mg of DOC per gram of biochar.

Phosphorous assay preparation using RBC and P400 biochar

This method was adapted from Sacko et al. (2020).[50] Each of the assay treatments were performed in triplicates using 50-mL centrifuge tubes. 0.5 g of biochar, 5.0 g of soil, 15.0 mL of ultrapure water/biochar filtrate was used in the assay. The components of each assay were mixed thoroughly in a centrifuge tube by placing on an Innova 2300 Platform Shaker at 30 rpm at room temperature and allowing to shake for 30 minutes. After 30 minutes the samples were centrifuged at 4000 rpm in a Beckman Coulter Avanti® J-26 XP centrifuge using a JS-5.3 rotor for 5 min. The samples were then carefully removed from the centrifuge and placed upright in order to prevent disturbing any particulate back into solution. 1.0 mL of each sample solution was pipetted and placed into poly vials for phosphate analysis. The pH of the remaining mixture was then recorded, and the sample tubes were placed back onto the shaker platform. 1.0 mL of each sample solution was collected again in two days and fourteen days in the same method as stated above and the pH was also recorded.

Table 8. Layout of phosphate assays prepared using RBC and P400 biochar

Control	**Portneuf Soil (P-Soil)**	**Bennett Soil (B-Soil)**
Water	Water + P-soil	Water + B-soil
P400 UN + water	P400 UN + water + P-soil	P400 UN + water + B-soil
RBC UN + water	RBC UN + water + P-soil	RBC UN + water + B-soil
P400 90D + water	P400 90D + water + P-soil	P400 90D + water + B-soil
RBC 90D + water	RBC 90D + water + P-soil	RBC 90D + water + B-soil
P400 90W + water	P400 90W + water + P-soil	P400 90W + water + B-soil
RBC 90D filtrate	RBC 90D filtrate + P-soil	RBC 90D filtrate + B-soil
P400 90D filtrate	P400 90D filtrate + P-soil	P400 90D filtrate + B-soil
P400 90W filtrate	P400 90W filtrate + P-soil	P400 90W filtrate + B-soil
P400 90W+S filtrate	P400 90W+S filtrate + P-soil	P400 90W+S filtrate + B-soil

Ozonized biochar filtrate with various DOC concentrations for phosphorus solubilization

The amount of phosphate and pH change resulting from just the filtrates with various DOC concentrations was determined. 15 mL of each of the respective filtrate dilutes of ozonized biochar measured as DOC concentration ranging from 0 ppm (water) to 100 ppm was incubated in a tube without adding soil for a period of up to 8 days to serve as controls. A mixture of ozonized biochar filtrate and soil (SRM 694, P Soil and B Soil) was prepared. The purpose is to determine the amount of phosphate and pH change upon addition of the soil to the filtrate. 10 g of soil was added to 30 mL of each respective filtrate dilutes and incubated for a period of up to 8 days. Whereas 0.2

g of SRM 694 was added to 15 mL of each respective filtrate and incubated for a period of up to 8 days for comparison. The concentration of phosphate solubilized from the soil was obtained by subtracting the amount of the phosphate from the filtrates only before soil was added.

Phosphorous assay layout

Total of 84 tubes (50-mL centrifuge tubes) of the filtrate treatment samples were incubated by placing them at room temperature on an Innova 2300 Platform Shaker at 30 rpm (Figure 11). After 30 min of shaking (day 0), the pH was measured in each tube using the pH probe. The samples were centrifuged at 4500 rpm for 15 min using a Beckman Coulter centrifuge with a JS-5.3 swinging-bucket rotor. 1 mL of the supernatant was collected from each sample. The tubes were placed back on the shaker for further incubation. The procedure was repeated at days 2, 4, 6, and 8 days.

Table 9. Layout of phosphate assays prepared using ozonized biochar filtrate

Control	**Portneuf Soil (P-soil)**	**Bennett Soil (B-soil)**	**SRM 694**
0 ppm DOC	0 ppm + P-soil	0 ppm DOC + B-soil	0 ppm + SRM
5 ppm DOC	5 ppm + P-soil	5 ppm DOC + B-soil	5 ppm + SRM
10 ppm DOC	10 ppm + P-soil	10 ppm DOC + B-soil	10 ppm + SRM
25 ppm DOC	25 ppm + P-soil	25 ppm DOC + B-soil	25 ppm + SRM
50 ppm DOC	50 ppm + P-soil	50 ppm + B-soil	50 ppm + SRM
100 ppm DOC	100 ppm + P-soil	100 ppm + B-soil	100 ppm + SRM
0 ppm DOC (pH 3)	0 ppm (pH 3) + P-soil	0 ppm (pH 3) + B-soil	0 ppm (pH 3) + SRM

Figure 11. Incubations of phosphorus treatment samples.

Phosphate Concentration Measurement

This method was adapted from Sacko et al. (2020).[50] Supernatant (1 mL) collected previously was diluted to 5 mL in poly vials and analyzed for the phosphate content right away using AS40 Automated Dionex ICS-5000 Ion Chromatography system mounted with Dionex IonPac AS23 anion-exchange column (2×250 mm). A standard calibration curve (Figure 12) was prepared using Dionex 7 Anion Standard II purchased from Thermo Scientific (057590). Standards containing 1 ppm, 2.5 ppm, 5 ppm, 10 ppm, 20 ppm, and 0 ppm (Ultrapure water) of phosphate anion were used for the calibration of the Ion Chromatography system.

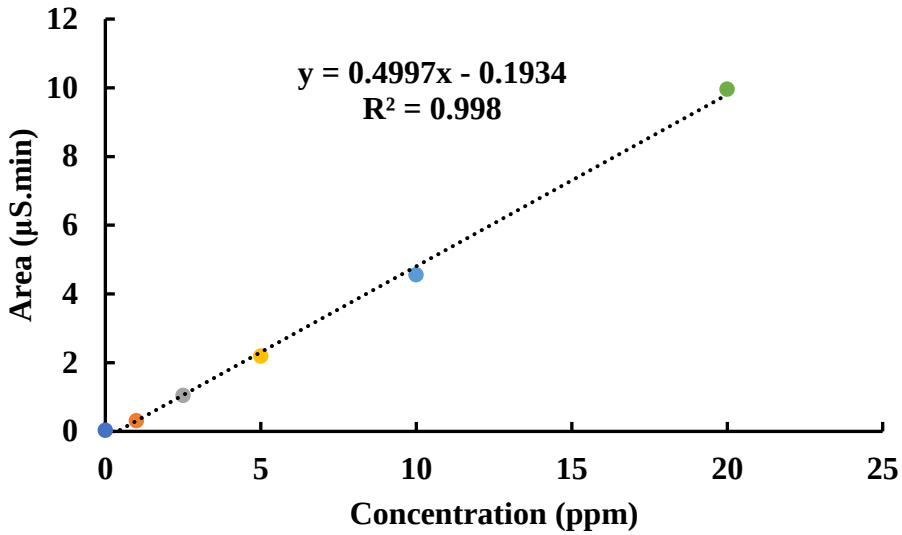

Figure 12. Calibration curve plotted for the area of the peak versus the phosphate concentration of the Dionex 7 Anion standard for Ion Chromatography.

Phytotoxicity study of ozonized biochar filtrate with various DOC concentrations used for phosphorus solubilization in dicotyl garden cress (*Lepidium sativum*) seeds

This experiment is a continuation of the phosphorus assay experiment and was conducted right after the 8th day of the phosphorus assay experiment. Only the tubes with B-soil and P-soil were used during the experiment. After collecting all the required supernatant liquid for phosphorus concentration measurement, 10 seeds of dicotyl garden cress were placed in each of the 50-mL centrifuge tubes. Dicotyl garden cress being suitable for hydroponic cultivation, small amount of supernatant liquid that was remaining in the tubes was okay for the experiment. Total of 84 tubes were placed in a holder in upright position without their caps. After taking the pictures of the tubes in a designated place inside the lab, the tubes were placed in an area with no light interference. The tubes were taken out every 24 hours for observation and pictures were taken in

the same manner as taken in Day 0. This process was repeated for 10 days. At the end of 10 days the tubes were placed in an area with sufficient light for further observations.

RESULTS AND DISCUSSION

Effect of ozonization on biochar pH:

Overall, the biochar pH decreased because of the ozone treatment. There was a large decrease in pH with RBC compared to P400. The untreated control sample of rogue biochar (RBC UN) had a basic pH value of 9.86±0.03. After 90 min of dry-ozone treatment, the biochar (RBC 90D) pH drastically dropped down to 3.13±0.04, whereas after 90 min of wet-ozone treatment, the biochar (RBC 90W) pH slightly dropped down to 9.05±0.12. On the other hand, the untreated control sample of pinewood biochar (P400) had almost acidic pH value of 6.08±0.04. After 90 min of dry-ozone treatment, the biochar (P400 90D) pH dropped down to 4.06±0.03, whereas after 90 min of wet-ozone treatment, the biochar (P400 90W) pH dropped down to 3.75±0.05 (Table 10).

Effect of ozonization on Biochar CEC:

The CEC value of RBC UN (control) was determined to be 19.71±1.42 cmol/kg using the AOAC $Ba(OAc)_2$ method. Upon 90 min of dry-ozone treatment, the biochar CEC increased to 142.92±2.64 cmol/kg (Table 10), whereas after 90 min of wet-ozone treatment, the biochar CEC increased to 22.91±0.04 cmol/kg. On the other hand, the CEC value of P400 UN (control) was determined to be 27.22±1.30 cmol/kg. Upon 90 min of dry-ozone treatment, the biochar CEC increased to 29.68±1.51 cmol/kg (Table 10), whereas after 90 min of wet-ozone treatment, the biochar CEC increased to 32.99±0.61 cmol/kg.

Table 10: pH and CEC of the RBC and P400 biochar before and after ozonization. The values for pH are the averages of 2 replicates ± SD (n=2) whereas the values for CEC are the averages of 6 replicates ± SD (n=6).

Biochar Sample	**pH** (means ± SD)	**CEC** (cmol/kg) measured by $Ba(OAc)_2$ method (means ± SD)
Non-ozonized biochar RBC UN	9.86 ±0.03	19.71±1.42
Wet-ozonized biochar RBC 90W	9.05 ±0.12	22.91±0.04
Dry-ozonized biochar RBC 90D	3.13 ±0.04	142.92±2.64
Non-ozonized biochar P400 UN	6.08 ±0.04	17.35±0.91
Wet-ozonized biochar P400 90W	3.75 ±0.05	32.99±0.61
Dry-ozonized biochar P400 90D	4.06 ±0.03	29.68±1.51

Dissolved organic carbon

The impact of ozonization on the biochar was evident in the color of the filtrate extracted from the biochar (Figure S9 and S10). The filtrate from the non-ozonized biochar (RBC UN & P400 UN) and wet-ozonized Rogue biochar (RBC 90W) appeared clear whereas the filtrate from the dry-ozonized biochar (RBC 90D & P400 90D), wet-ozonized Pinewood biochar (P400 90W), and wet-ozonized and sonicated Pinewood biochar (P400 90W+S) biochar appeared dark brown, suggesting a higher presence of dissolved organic carbon fragments. Although the CEC of dry-ozonized (P400 90D) and wet-ozonized (P400 90W) biochar was almost equal, the total extracted DOC from the wet-ozonized (P400 90W) biochar was twice the DOC from the dry-ozonized (P400 90D) biochar. On the other hand, CEC of dry-ozonized (RBC 90D) biochar was 5 times the CEC

of wet-ozonized (P400 90W) biochar, but their total extracted DOC was almost equal. The total extracted DOC from the dry-ozonized P400 90D biochar was 5.35 (±0.05) mg DOC/g, wet-ozonized P400 90W biochar was 11.44 (±0.16) mg DOC/g, and dry-ozonized RBC 90D biochar was 15.20 (±0.20) mg DOC/g. Wet-ozonization when combined with 30 minutes of sonication resulted in doubling the total extracted DOC. The total extracted DOC from the wet-ozonized and sonicated (P400 90W + S) biochar was 23.15 (±0.35) mg DOC/g.

Table 11: Amount of DOC material extracted from the RBC and P400 biochar before and after ozonization. The values are means ± SD (n =2).

Biochar Sample	**DOC from Biochar** (mg DOC/g biochar)
Non-ozonized biochar RBC UN	2.28 (±0.24)
Wet-ozonized biochar RBC 90W	2.75 (±0.15)
Dry-ozonized biochar RBC 90D	15.20 (±0.20)
Non-ozonized biochar P400 UN	2.32 (±0.32)
Wet-ozonized biochar P400 90W	11.44 (±0.16)
Dry-ozonized biochar P400 90D	5.35 (±0.05)
Wet-ozonized and sonicated biochar P400 90W + S	23.15 (±0.35)

Table 12. Phosphorus concentration released by ozonized biochar (10% by soil mass) in soil after 14 days of incubation with P-soil and B-soil

Releasing agent	**Concentration of phosphorus released (ppm)**	
	P-soil	**B-soil**
Water	0.40 (±0.12)	0.11 (±0.04)
Non-ozonized biochar P400 UN	1.17 (±0.08)	0.39 (±0.20)
Dry-ozonized biochar P400 90D	2.98 (±0.07)	1.58 (±0.09)
Wet-ozonized biochar P400 90W	3.60 (±0.22)	2.11 (±0.15)

Phosphorus solubilization of soil with RBC and P400 biochar

The solubilized phosphate concentration in the incubation liquid of B-soil and P-soil with RBC and P400 biochar and its filtrates of various DOC concentration was measured in comparison with the control incubation liquid of B-soil and P-soil with DI water. Here, phosphate concentration was measured by ion chromatography.[50] The peak that was detected at a retention time of 14.6-14.7 min for the incubation liquid of wet-ozonized pinewood biochar with soil appeared to be much higher than that of the phosphate signal curves for the incubation liquid of control as well as untreated pinewood biochar (Figure 13 & 14). As shown in the phosphate standard calibration measurements using ion chromatography, the conductivity signal intensity of the phosphate peak was detected at a retention time range of 14.6–14.7 min, thus verifying that the peak obtained was indeed phosphate. Rogue biochar (ozone treated and untreated) showed no difference in phosphate peak from the water control. Dry-ozonized RBC 90D biochar, despite of having a very high CEC, was not able to solubilize phosphorus from the soil samples. Wet-

ozonized (P400 90W) biochar was most efficient in solubilizing the insoluble phosphate materials in soil releasing 3.60 ppm of phosphorus in 15 mL of water used in its incubation with P-soil which is 9 times the phosphorus released in its water control. Although ozone treatment did not enhance the CEC in Pinewood biochar as much as Rogue biochar, it seems to have some effect in phosphorus solubilization. In P-soil, dry-ozonized (P400 90D) biochar released 2.98 ppm of phosphorus which is at least twice the amount of phosphorus released by non-ozonized (P400 UN) biochar. In B-soil, wet-ozonized (P400 90W) biochar released 2.11 ppm of phosphorus which is at least 5 times the amount of phosphorus released by non-ozonized (P400 UN) biochar.

Also, for all the ozonized biochar filtrate, the phosphate signal curve for the incubation liquid with both P-soil and B-soil appeared to be similar to the phosphate signal curve for the filtrate control. Ozonized biochar filtrate for both Rogue and Pinewood biochar used in the assay had a large amount of phosphorus which could potentially be a direct source of phosphorus to the plants when applied to phosphorus deficient soils.

Table 13. Phosphorus concentration released by ozonized biochar filtrate with various DOC concentrations in soil after 30 minutes of incubation with SRM 694, P-soil, and B-soil.

Releasing agent	**Concentration of phosphorus released (ppm)**		
	SRM 694	**P-soil**	**B-soil**
Water	0.99 (±0.18)	0.30 (±0.14)	0.14 (±0.09)
100 ppm DOC biochar filtrate	11.4 (±1.25)	N/A	N/A
Water (pH = 3)	1.12 (±0.12)	0.61 (±0.08)	0.19 (±0.14)

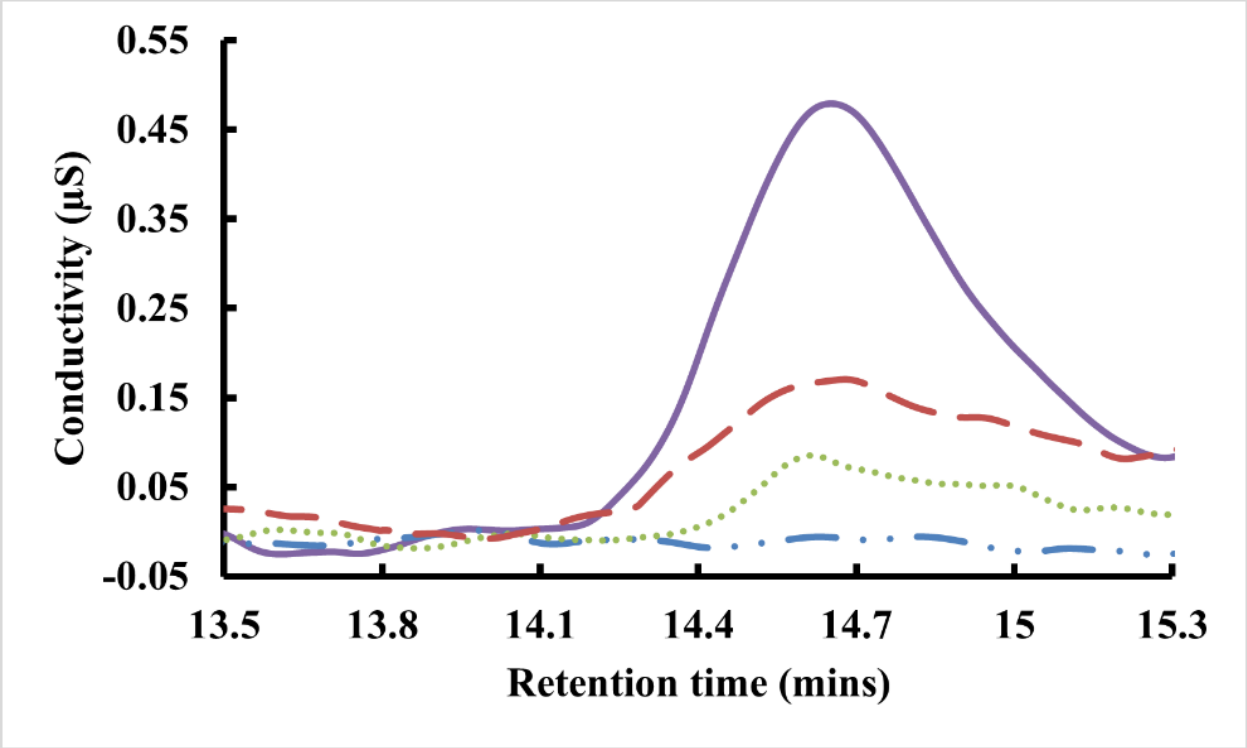

Figure 13. A part of Ion Chromatogram showing the phosphate peak for B-soil.

B-soil + Water represented by blue line (dashed with dots), P400 UN Biochar + B-soil + Water represented by green line (dotted), P400 90D Biochar + B-soil + Water represented by red line (dashed) and P400 90W Biochar + B-soil + Water represented by purple line (solid).

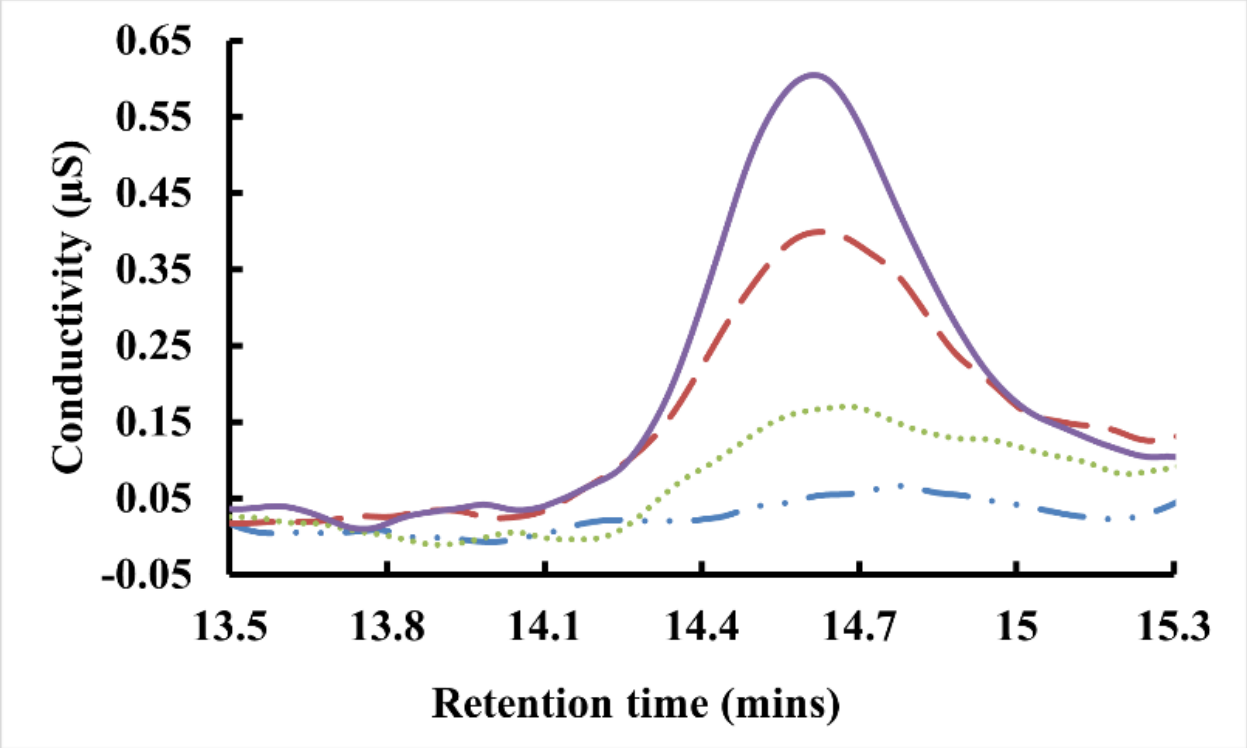

Figure 14. A part of Ion Chromatogram showing the phosphate peak for P-soil.

P-soil + Water represented by blue line (dashed with dots), P400 UN Biochar + P-soil + Water represented by green line (dotted), P400 90D Biochar + P-soil + Water represented by red line (dashed) and P400 90W Biochar + P-soil + Water represented by purple line (solid).

Phosphorus solubilization of SRM 694, B-soil, and P-soil using ozonized biochar filtrate with various DOC concentrations and its phytotoxicity study

The solubilized phosphate concentration in the incubation liquid of SRM 694, B-soil and P-soil with ozonized biochar filtrate of various DOC concentration was measured in comparison with the control incubation liquid of SRM 694, B-soil and P-soil in DI water with normal pH and pH 3.0 DI water (same pH of the dry-ozonized biochar filtrate). The peak at 10.9 min for the

incubation liquid of SRM 694 with the ozonized biochar filtrate (100 ppm DOC) appeared to be much higher than that of the phosphate signal curve for its incubation liquid with DI water (Figure 15). As shown in the phosphate standard calibration measurements using ion chromatography, the conductivity signal intensity of the phosphate peak was detected at a retention time range of 10.7–11.1 min (Figure S8), thus verifying that the peak obtained was indeed phosphate. In soil, for all the ozonized biochar filtrate DOC concentrations, the peak at 10.7–11.1 min had almost same intensity to the phosphate signal curve for the filtrate control. There was a large competition between the peaks of nitrate and sulphate in the chromatograms at retention time 9.5 and 11.7 min respectively with the peak of phosphate. Since this biochar filtrate has a lot of phosphate, and there is an interference in ion chromatography signals, no conclusions can be drawn yet on the phosphorus solubilization in soil. The effect of the biochar filtrate in phosphorus solubilization in SRM 694 is however significant. 100 ppm DOC biochar filtrate was able to release 11.4 ppm of phosphorus in 15 mL of water used in its incubation with SRM 694 which is at least 10 times the phosphorus released in its water control. Biochar filtrate with lower DOC concentrations however did not show significant effect in the phosphorus solubilization in SRM 694. In addition, the ozonized biochar filtrate shows no signs of phytotoxicity as shown by the experiment conducted right after the 8^{th} day of the phosphorus assay experiment (Figure 16). This result demonstrated that biochar ozonization can produce certain amount of oxygenated biochar molecular fragments, which not only can be used a direct source of phosphorus for plant applications as it contains a large amount of phosphorus, but has potentials in solubilizing the insoluble phosphate materials in soil.[100]

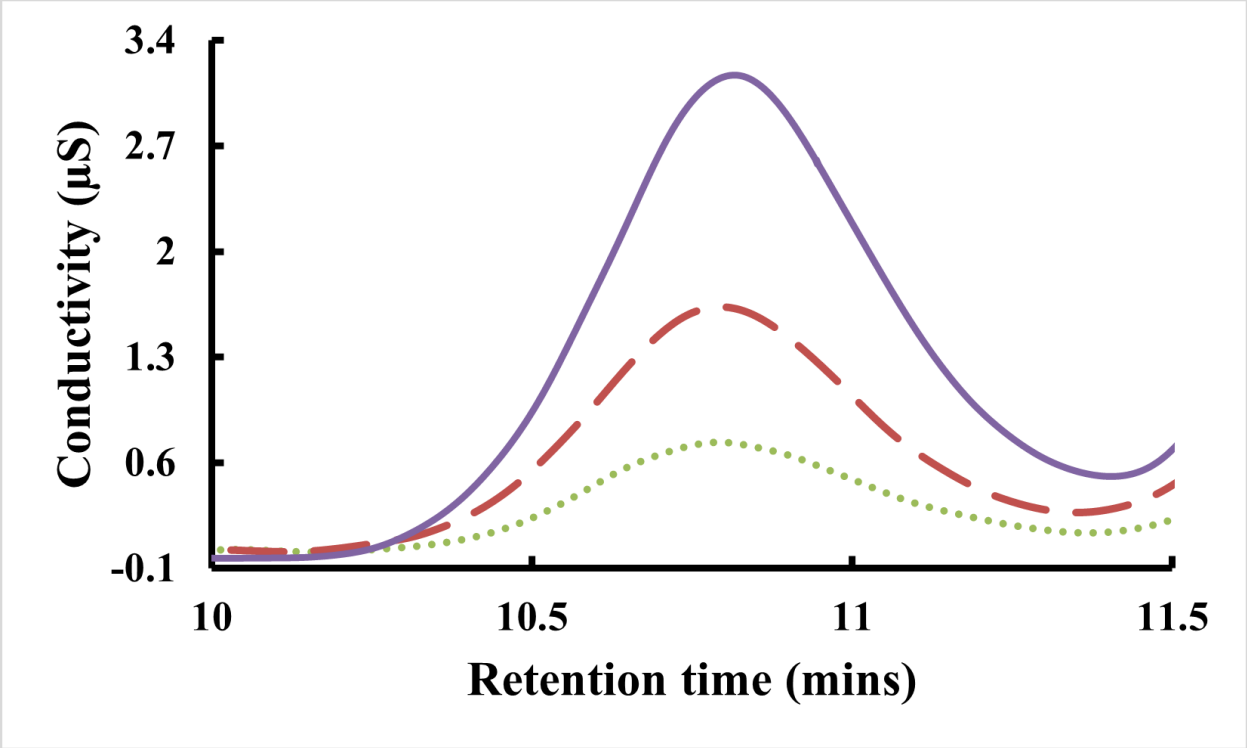

Figure 15. A part of Ion Chromatogram showing the phosphate peak for SRM 694.

SRM + Water represented by green dotted line, ozonized biochar filtrate (100 ppm DOC) control represented by red dashed line, and ozonized biochar filtrate (100 ppm DOC) + SRM represented by purple solid line.

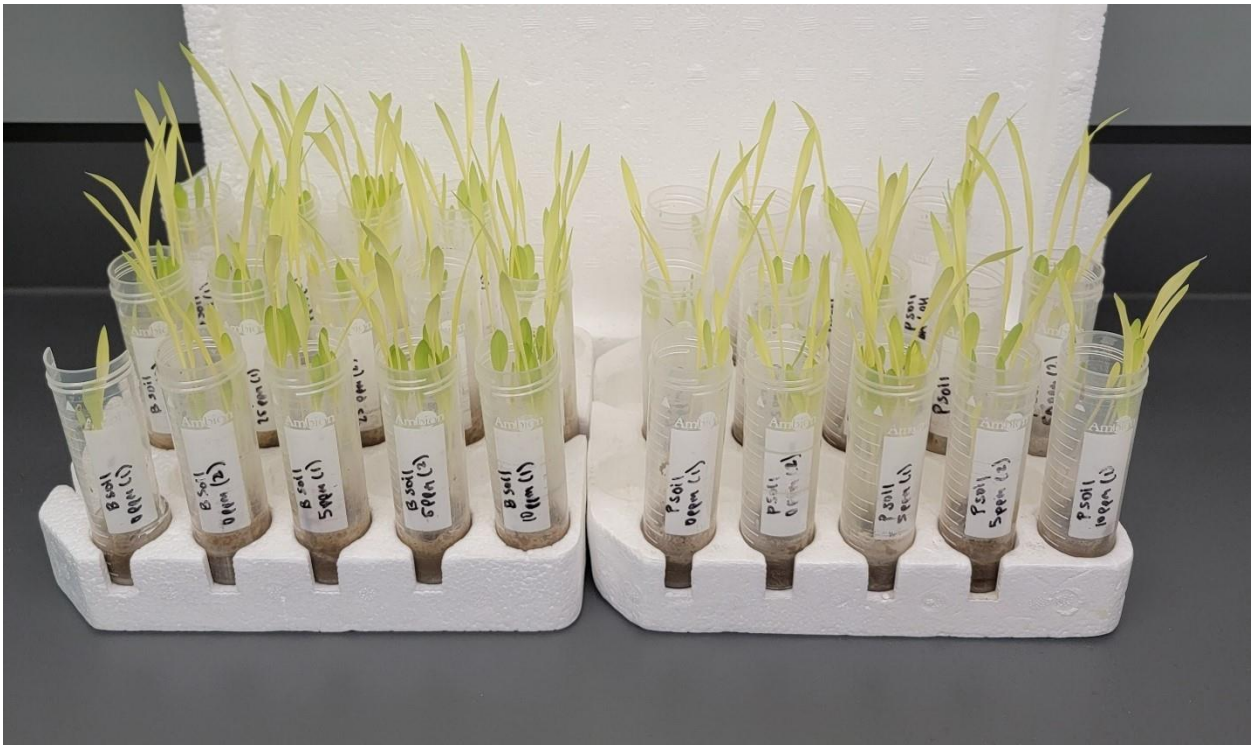

Figure 16. Images of the tubes for phytotoxicity study of ozone treated biochar taken after 10 days of exposure of seeds of the dicotyl garden cress (*Lepidium sativum*) to soil mixed with ozonized biochar filtrate of various DOC concentrations.

CONCLUSION

In conclusion, the ozonization treatment, while not enhancing the CEC in Pinewood biochar as much as Rogue biochar, seems to have some effect on phosphorus solubilization. Ozone treatment had significant impacts on both the pH and cation exchange capacity (CEC) of the studied biochars. The results indicated a substantial decrease in pH levels for both RBC and P400 after ozone treatments. Interestingly, while RBC experienced a drastic drop in pH during dry-ozone treatment, the wet-ozone treatment led to a milder decrease. Whereas P400, which initially had a more acidic pH, exhibited a reduction in pH with both dry and wet ozone treatment, with dry

treatment causing a more pronounced reduction. Regarding CEC, ozonization resulted in an increase in CEC values for both RBC and P400, indicating enhanced cation retention capacity. The extent of CEC increase varied between dry and wet ozone treatments. This suggests that ozonization not only affects biochar pH but also influences its ability to retain cations, potentially impacting soil fertility and nutrient availability. Additionally, the ozonization treatment influenced the dissolved organic carbon (DOC) content of the biochar. Wet-ozonized (P400 90W) biochar was found to be the most efficient in solubilizing insoluble phosphate materials in soil, releasing 3.60 ppm of phosphorus in 15 mL of assay used in its incubation with P-soil, which is 9 times the phosphorus released in its water control. Dry-ozonized (RBC 90D) biochar, despite having a high CEC, was not able to solubilize phosphorus from the soil samples. In P-soil, both wet-ozonized (P400 90W) and dry-ozonized (P400 90D) biochar released significant amounts of phosphorus compared to non-ozonized (P400 UN) biochar, whereas, in B-soil, wet-ozonized (P400 90W) biochar released 2.11 ppm of phosphorus, at least 5 times the amount released by non-ozonized (P400 UN) biochar. Ozonized biochar filtrate, for both Rogue and Pinewood biochar, had a large amount of phosphorus, potentially serving as a direct source of phosphorus to plants when applied to phosphorus-deficient soils. Biochar filtrate with 100 ppm DOC concentration was able to release 11.4 ppm of phosphorus in 15 mL of used in its incubation with SRM 694, at least 10 times the phosphorus released in its water control. However, lower DOC concentrations did not show a significant effect on phosphorus solubilization in SRM 694. Despite challenges in interpreting the phosphorus solubilization in soil due to interference in ion chromatography signals, the ozonized biochar filtrate demonstrates a significant impact on solubilized phosphate concentration in standard reference material (SRM). The solubilized phosphate concentration in the incubation liquid of soil with ozonized pinewood biochar appeared higher, suggesting a potential impact on

nutrient dynamics. Furthermore, the absence of phytotoxicity in the biochar filtrate implies the production of oxygenated biochar molecular fragments, offering a potential direct source of phosphorus for plant applications. Overall, the results suggest that ozonized biochar, particularly wet-ozonized (P400 90W) biochar, has the potential to enhance phosphorus solubilization in different soils, providing a valuable source of phosphorus for plant growth without exhibiting phytotoxic effects. However, challenges in ion chromatography analysis should be addressed for more accurate conclusions regarding phosphorus solubilization in soil.

CHAPTER 4

INVESTIGATION OF CALCIUM AND MAGNESIUM CATION-PROTON EXCHANGE WITH TRANSMEMBRANE ELECTROSTATICALLY LOCALIZED PROTONS (TELP) AT A LIQUID-MEMBRANE INTERFACE

INTRODUCTION

First postulated in 2012, JW Lee's Transmembrane Electrostatically Localized Proton (TELP) theory and subsequent laboratory experimentation has significantly expanded previous understandings of classical Mitchellian chemiosmotic theory.[70, 71, 140-144] Lee's theory originally aimed to explain the many naturally occurring circumstances of alkalophilic bacteria, phototrophs (including chloroplasts), and mitochondrial-powered chemotrophs that Peter Mitchell's historic textbook proton motive force (pmf) equation could not in isolation explain.[140, 142, 144] The most notable shortcoming of the classic pmf equation is seen in alkalophilic bacteria (*Bacillus pseudofirmus*) where the classic Mitchellian equation predicts a pmf of only 44 mV which when considered in isolation is not compatible with ATP synthesis. The most conservative values are generally accepted to be 156 mV.[145-147] The study of ATP generation in these species implores the question: do mitochondria-powered chemotrophs have additional thermotropic function and if so, how are they reaching biologically sustainable ATP productive thresholds? [70]

Peter Mitchell's equation for pmf is typically expressed as:

$$pmf = \Delta\psi - (2.3\ RT)\Delta pH/F \quad (5)$$

Over the last decade of research Lee has shown that these *B. pseudofirmus* species utilize heat energy in conjunction with TELP to optimize and drive ATP synthesis as well as uncovered the biological significance of mitochondrial cristae formation. Most specifically, TELP theory has expanded our understanding of the generation of proton motive force (pmf) near cellular membranes and adjacent surfaces.[70] Via bimimetic experimental demonstrations, TELP helped elucidate the bioenergetics of "protonic capacitors" as contributors to pmf that arise in the setting of excess hydroxide anions and protons on opposing sides of the membrane (Figure 17). Free excess protons in aqueous solution separated by an impermeable membrane will spontaneously localize to the liquid-membrane interface.[140, 147]

Mathematically, TELP theory can be expressed as the motor force across a biomembrane that incorporates both the classic and now local pmf that will be referred to as "total pmf" henceforward Equation 6.[70]

$$pmf = \Delta\psi + \frac{2.3\ RT}{F}\log_{10}\left(\left[H^+_{pB}\right]/[H^+_{nB}]\right) + \frac{2.3\ RT}{F}log_{10}(1 + [H^+_L]/[H^+_{nB}]) \quad (6)$$

where $\Delta\psi$ is the "membrane potential from the p-side to the n-side" as defined by Mitchell previously, $[H^+_L]$ is the TELP concentration at the liquid-membrane interface on the positive (P) side of the membrane; $\left[H^+_{pB}\right]$ is the "proton concentration in the bulk aqueous p-phase" (intermembrane space in the case of mitochondria); and $[H^+_{nB}]$ is the "proton concentration in the

bulk liquid n-phase" (matrix in mitochondria). The first two terms of Equation 6 includes the "Mitchellian bulk phase-to-bulk phase proton electrochemical potential gradients" that is now consider as the "classic" pmf, identical to that of Equation 5; while the final term accounts for the "local" pmf from TELP at the liquid-membrane interface.[70]

The relationship between the ideal TELP concentration $[H_L^+]^0$ at the liquid-membrane interface and the transmembrane potential $\Delta\psi$ in a proton capacitor can be expressed as:

$$[H_L^+]^0 = \frac{C}{S} \cdot \frac{\Delta\psi}{l \,.\, F} \tag{7}$$

where C/S is the specific membrane capacitance per unit surface area, l is the thickness of the localized proton layer.

The TELP theory has described "total pmf" with H^+ populations at both the liquid-membrane interface (TELP) and the bulk-liquid phase (delocalized protons). Non-proton cations in the bulk aqueous liquid phase can exchange with protons at the liquid-membrane interface and thus affect the force generated by TELP.[144] The exchange effects of non-proton cations in the bulk liquid phase on the effective TELP concentration at the liquid-membrane interface can be quantified with the following equation.

$$[H_L^+] = \frac{[H_L^+]^0}{\Pi_{i=1}^{n} \left\{ K_{Pi} \left(\frac{\left[M_{pB}^{i+}\right]}{\left[H_{pB}^+\right]} \right) + 1 \right\}} \tag{8}$$

where K_{Pi} is the equilibrium constant for cation to exchange with TELP, $\left[M_{pB}^{i+}\right]$ is the concentration of non-proton cations in the bulk phase of the surrounding liquid environment.

This "non-proton cation interference" has been observed with the non-proton cation species Na^+, K^+, Mg^{2+} and Ca^{2+}. To better elucidate the effects of non-proton cations on TELP, experimental models demonstrated the capacitor generated force using a proton sensing film apparatus. Localized cation exchange will occur in the presence of protons at a membrane surface when a voltage is applied to an electrolysis chamber.[142]

Electrolysis allows water to separate into its respective ions. In an electrolytic cell, water molecules (H_2O) are split into their constituent elements, hydrogen (H_2) and oxygen (O_2), through the process of electrolysis. Electrolysis typically involves application of an electrolytic voltage across two electrodes (anode and cathode) placed in a solution (in this case, water). At the cathode (negative electrode), electrons are supplied, which reduce water molecules to hydrogen gas and hydroxide ions (OH^-). At the anode (positive electrode), water molecules get oxidized to oxygen gas releasing protons (H^+). According to the proton electrostatic effect, it is anticipated that excess protons would disperse along the outer surface of a water body. Additionally, when two aqueous phases are separated by a membrane, these excess protons are expected to localize themselves at the interface between the water and the membrane on the anodic side of the electrolysis chamber.

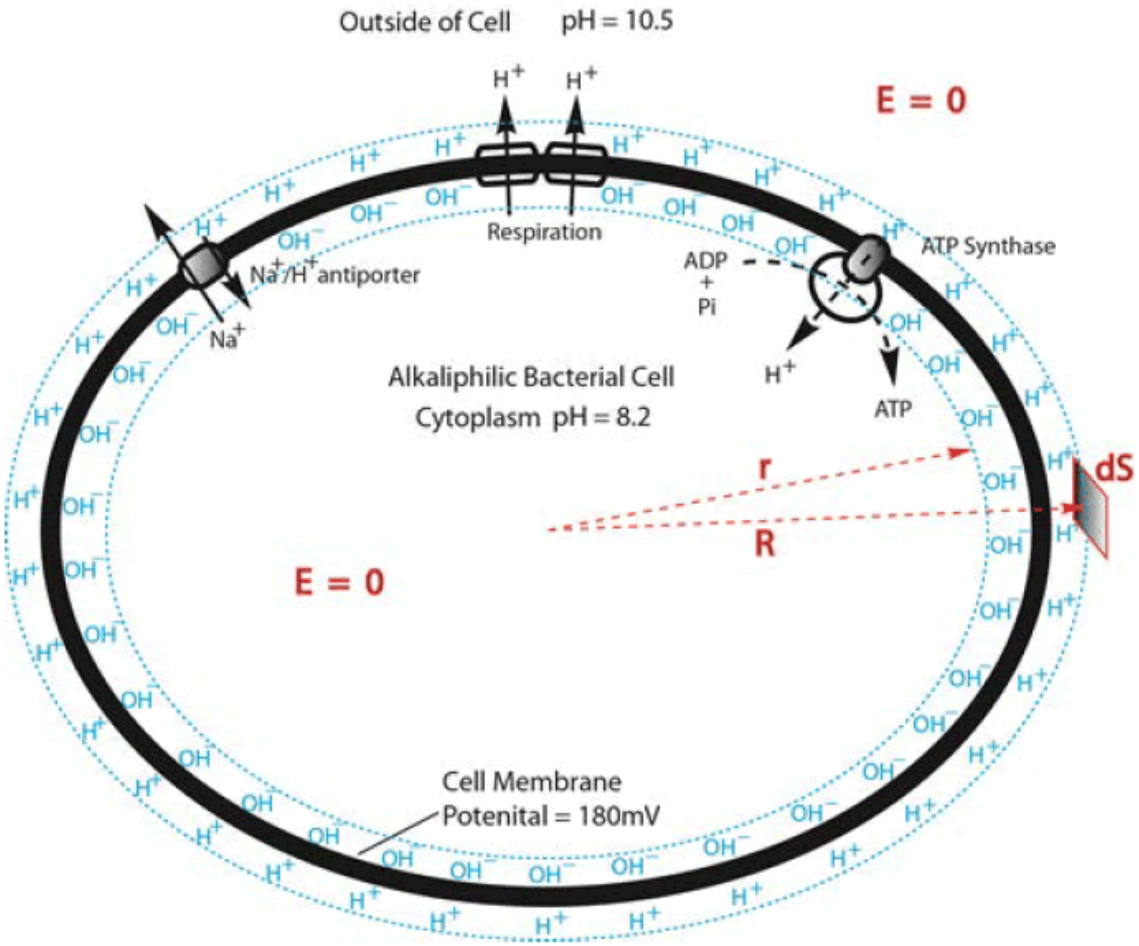

Figure 17. **TELP model for a bacterial cell membrane.**

The transmembrane-electrostatically localized protons (TELP) model shown as "a proton capacitor-like structure" illustrating how excess H^+ and OH^- are transmembrane electrostatically localized at the water-membrane interfaces along the two sides of the bacterial cell membrane before proton-cation exchange as it would be in a theoretically pure water-membrane-water system. (Adapted from Ref 141)

Conductance, expressed in siemens (S), is the inverse of electric resistance (measured in ohm). When dealing with bulk materials, it's often more convenient to measure specific conductance rather than just conductance. Specific conductance of a liquid, commonly referred to as conductivity, is measured with a non-electrolytic alternating current (AC) across the liquid per unit distance. The conductivity of water indicates its ability to conduct electric (ionic) current, which increases with the presence of mobile ions in water, serving as electric charge carriers. It is measured in microsiemens per centimeter (μS/cm) and is the reciprocal of resistivity (measured in Ω-cm). For instance, fresh ultrapure water typically exhibits a conductivity of 0.055 μS/cm, which gives a resistivity of 18.2 MΩ-cm. Conventional measurements of the electrical resistivity of water typically involve using non-electrolytic high-frequency AC probing voltage, which doesn't induce the water electrolysis process. This means that during conventional electrical resistivity measurement, no excess protons are generated within the water body. Consequently, the traditional method of measuring water electrical resistivity doesn't accurately reflect the protonic conductivity of water concerning excess protons.

During the open-circuit water electrolysis, excess protons and excess hydroxide ions are generated in two water bodies separated by a membrane. Excess hydroxide ions localize at the negative (N) side of the membrane in the cathode chamber, while an electric double layer forms at the cathodic electrode. Conversely, excess protons localize at the positive (P) side of the membrane in the anode chamber, while another electric double layer forms at the anodic electrode. When a central sample chamber containing a solution with non-proton cations is placed in between a cathode chamber and an anode chamber, the non-proton cations will compete with TELP at the liquid-membrane interface inside the central sample chamber. The competition at the liquid-membrane interface results in exchange between cations and TELP at the positive (P') side of the

membrane in the central sample chamber. There are two points of interest in investigating cation equilibrium exchange at the membrane interface. The first is the mid-point, where 50% of protons have exchanged with non-proton cations. This is called the equilibrium constant. The second point of interest is total proton-delocalization from the membrane. A previous study determined the equilibrium constant for Na^+ and K^+ to exchange with localized H^+ layer to be $(5.07 \pm 0.46) \times 10^{-8}$ and $(6.93 \pm 0.91) \times 10^{-8}$ respectively.[142] These results mean that localized protons at the water membrane interface were so electrostatically stable that it requires on the order of ten million sodium or potassium ions to partially delocalize protons at the water-membrane interface.

Whilst monovalent cation-proton equilibrium exchange has been studied by Lee and colleagues, divalent cation exchange has not been studied previously. It is possible that divalent cations undergo cation-proton exchange at the P' membrane that is different from potassium and sodium ions.[142] The presence of alkali and alkaline earth cations can indirectly promote the dissolution of aluminum by modifying the rates of solvent motion, exchange, or orientation at the interface between the membrane and the solution. The degree of enhancement is directly proportional to the concentration of ions at the membrane surface and their solvation characteristics.[148]

The ionic radius of calcium and magnesium is substantially smaller than that of potassium and sodium.[149-154] Since divalent ions have higher electrostatic interactions, they have very high hydration energy resulting a tight bound water hydration shell around them. For example, magnesium cations have more than a six-fold increase with hydration.[155, 156] The weak association with the surface leads to ion-pair surface interactions during which some water molecules associated with the cations are partially released. Additionally, the arrangement of ions at the surface may lead to the polarization of the remaining water molecules of hydration. Divalent ions

like Ca^{2+} and Mg^{2+} may interact with membrane interface through a displacement process involving the removal of protons.[157] Distinctive characteristics (and their biologic implications) necessitate the qualitative and quantitative investigation of divalent ion electrostatic equilibrium exchange. The following study investigates the cation equilibrium exchange of the divalent cations Mg^{2+} and Ca^{2+} given their biological significance.

MATERIALS AND METHODS

Experimental demonstration of liquid water as protonic conductor

ElectroPrep electrolysis systems (Cat no. 741196) from Harvard Apparatus Inc (Holliston, MA) with a cathode chamber, a central sample chamber, and an anode chamber was used for electrolysis. The cathode and anode are made of platinum wires. A plastic septum with a circular channel, 3.2 cm in diameter, separates the anode and the cathode, where the sample chamber fits water-tight. The central sample chamber is hollow cylindrical made of Teflon with external diameter 3.2 cm and internal diameter 1.5 cm. The central sample chamber is designed with two detachable ends that can held circular membranes of 2.4 cm diameter water-tight such that it can hold 1.5 mL of liquid in between the membranes. The cathode chamber is smaller than the anode, and can functionally hold 300 mL of water, while the anode chamber holds 600 mL of water. Instead of measuring each time, a max-fill line was marked and used as the standard indicator for all trials. Water filled electrolysis apparatus is shown in Figure 18 and the dimensions of the water filled apparatus with the central sample chamber is shown in Figure 19.

In the first set of experiments, the central sample chamber was not introduced in the channel. The cathode and anode chambers were filled to the max-fill line with autoclaved deionized water. Conductance and pH of the water used to fill the cathode and anode chamber was

measured in a beaker using a Beckman coulter conductivity probe (Model 16 x 120 mm, item no. A57201) and Orion™ ROSS Ultra™ pH Electrode (Thermo Scientific, Cat No. 8102BNUWP). Typically, the conductivity of a liquid water sample was measured first before its pH measurement to avoid interference from a small amount of ions that may pass through the glass membrane of the pH glass electrode into the highly pure water sample during a pH measurement. The lid was placed on top of the apparatus and an electrolysis voltage of 200 V was applied for 5 hours using a digital multimeter system (Keithley instruments series 2400S-903-01 Rev E) to the experimental system and the electrolysis current (measured across the black and red cables) was recorded at an interval of 10 seconds in a machine-interfaced PC computer using a LabVIEW software with a National Instrument interfacing card. At the completion of the allotted time, the voltage source was turned off and removed from the apparatus. Conductance in each of the cathode chamber water and anode chamber water (bulk liquid phase) was measured which was followed by the pH measurements. The pH measurements in the cathode chamber water and anode chamber water were performed at various distances from the cathode and anode (to demonstrate excess protons do not change the bulk water pH of the chambers).

In the second set of experiments, a hollow central sample chamber (without membranes) with an external diameter of 3.2 cm and an internal diameter of 1.5 cm was inserted into the circular channel (3.2 cm in diameter) of the plastic septum (Figures 18 and 19). The cathode and anode chambers were filled to the max-fill line with autoclaved deionized water. The lid was placed on top of the apparatus and an electrolysis voltage of 200 V was applied for 5 hours to the experimental system and the electrolysis current was recorded at an interval of 10 seconds. Conductance and pH measurements for the liquid water were performed before and after the 5-hour experiment as described previously.

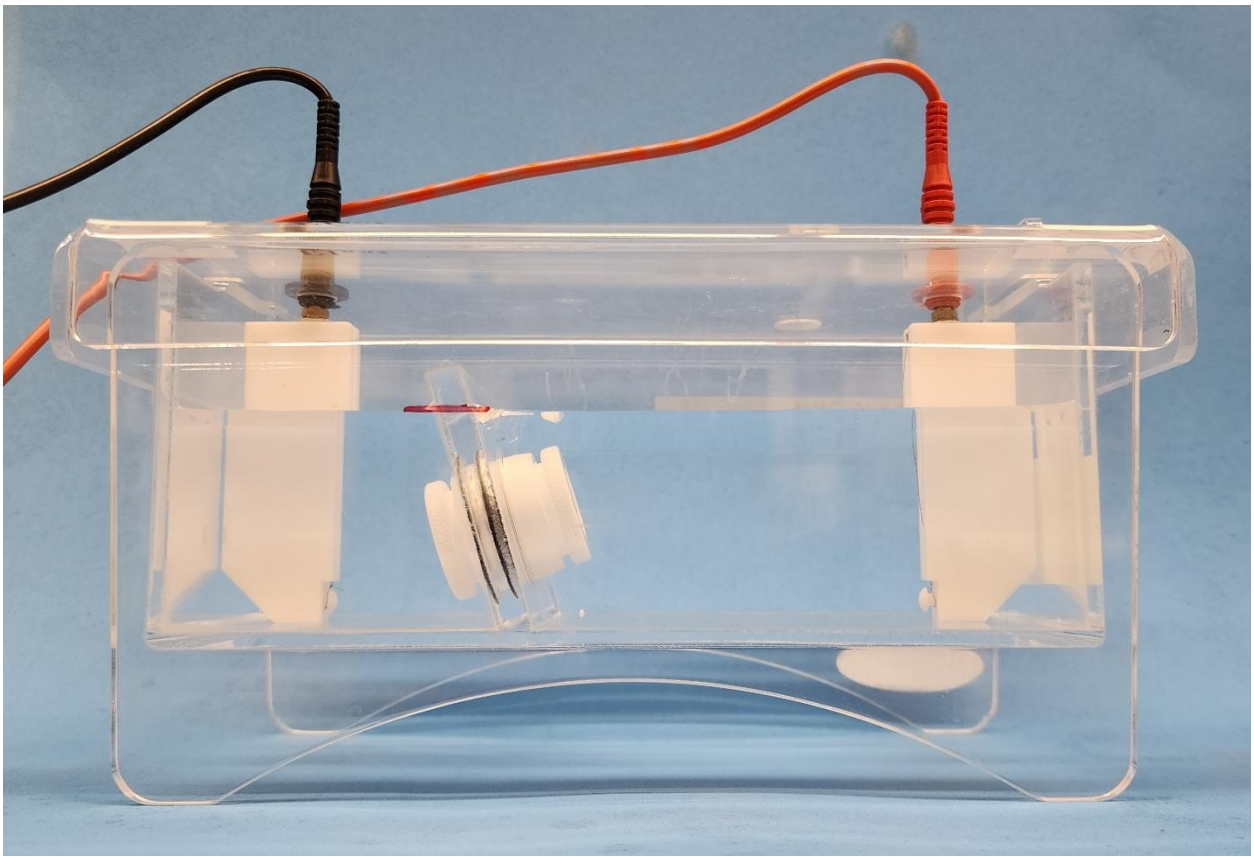

Figure 18. **ElectroPrep electrolysis system.**

Photograph of the ElectroPrep electrolysis apparatus filled with water to max-fill line (red) and a cylindrical Teflon central sample chamber inserted in the channel of the septum that separates the cathode chamber from the anode chamber. A platinum wire anchored with a Teflon bar (white material) serves as a cathode that is connected with the black cable (on the left); Another platinum wire anchored with a Teflon bar (white material) serves as an anode that is connected with the red cable (on the right).

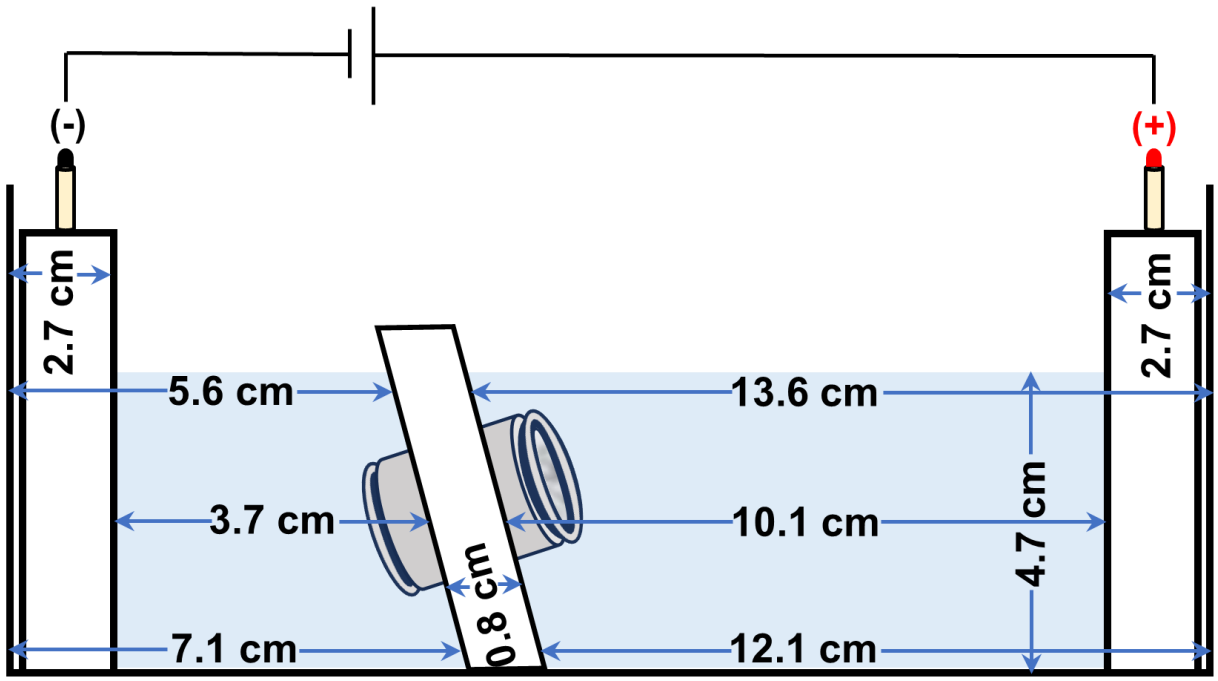

Figure 19. **Dimensions of the ElectroPrep electrolysis system.**

Sketch of the apparatus filled with water to max-fill line and the central sample chamber placed into the channel of the plastic septum. The septum is 0.8 cm thick, and the diameter of its channel is 3.2 cm. The water depth is 4.7 cm, the distance of the N membrane from the cathode is 3.7 cm, and the distance of the P membrane from the anode is 10.1 cm. The width of the anode and cathode liquid chambers is 9.5 cm (not shown). Each of the anode and cathode platinum wires is anchored with a Teflon bar (2.7-cm wide and 1-cm thick) and connected with the positive (Red) and negative (black) electric terminals, respectively.

Experimental demonstration of protonic capacitor

This method was adapted from the procedure previously reported in Saeed et al. (2018). [142]. ElectroPrep electrolysis systems (Cat no. 741196) from Harvard Apparatus Inc (Holliston,

MA) was used for electrolysis. To demonstrate the formation of a protonic capacitor, a membrane system was set up in the central sample chamber using aluminum (Al) and/or Teflon (Tf) as membranes. The aluminum and Teflon used in the experiments were 25 μm and 75 μm thick respectively. Aluminum sheet and Teflon were cut in circular discs of approximately 2.4 centimeters using a single-edge razor blade and a quarter dollar coin. In the first set of experiments, an electrolysis voltage of 200 V was applied and current versus time data points were recorded for the first 2000 seconds. Following set of experiments were performed by varying the thickness of the Teflon membrane:

75 μm (cathode-water-Tf-water-anode),

150 μm (cathode-water-2Tf-water-anode),

150 μm (cathode-water-Tf-water-Tf-water-anode),

150 μm (cathode-water-Tf-air-Tf-water-anode),

300 μm (cathode-water-4Tf-water-anode),

300 μm (cathode-water-2Tf-water-2Tf-water-anode), and

300 μm (cathode-water-2Tf-air-2Tf-water-anode)

Experiments with 75 μm and 150 μm membrane thickness were also performed with an electrolysis voltage of 100 V and 50 V. All the direct current (DC) electrolysis current versus time data points were recorded for various electrolysis voltages as well as various membrane thickness. Bulk water phase pH measurements were done before and after each of the experiments.

In the second set of experiments, aluminum (Al) film was used as protonic sensor along with Teflon (Tf) membrane. An electrolysis voltage of 200 V was applied for 5 hours and current versus time data points were recorded. Following set of experiments were performed by varying the thickness of the membrane:

125 µm (cathode-water-Al-Tf-Al-water-anode),

175 µm (cathode-water-Tf-Al-Tf-water-anode),

200 µm (cathode-water-Al-Tf-Water-Tf-Al-water-anode), and

200 µm (cathode-water-Tf-Al-Water-Tf-Al-water-anode)

The central sample chamber was held a consistent water-tight fit throughout experimentation. After testing for the integrity of the chamber such that it would not move, the cathode chamber was filled to the upper level of the central sample chamber and the entire apparatus was tipped carefully to the anode side so that the air bubble (Figure S11) that appears outside the central sample chamber towards the cathode chamber was removed. Then, the cathode chamber was filled to the max-fill line. After checking for leaks over to the other side, the anode chamber was filled to the max-fill line. The lid was placed on top of the apparatus, electrolysis voltage was applied, and the current was recorded as previously mentioned. Bulk water phase pH measurements were done before and after each of the experiments. pH of the solution in central sample chamber was also recorded before and after each of the experiments wherever applicable.

Synthesis of Calcium Bicarbonate

The $Ca(HCO_3)_2$ solutions used in all experiments were diluted solutions from a stock solution synthesized in Lee lab. 200 mL of 20 mM $Ca(HCO_3)_2$ (approx.) stock solution was synthesized through the following processes:

$$CO_2 + H_2O \rightarrow H_2CO_3 \quad (9)$$

$$CaCO_3 + H_2CO_3 \rightarrow Ca(HCO_3)_2 \quad (10)$$

At a 1:1 ratio of $Ca(CO)_3$ to $Ca(HCO_3)_2$ as depicted by the reaction above:

$$\frac{20\ mmol\ Ca(HCO_3)_2}{1\ L} = \frac{20\ mmol\ CaCOO_3}{1\ L}$$

$$\frac{20\ mmol\ CaCO_3}{1\ L} = \frac{x\ mmol\ CaCO_3}{0.2\ L}$$

$$x = 4.0x10^{-3}\ mol\ CaCO_3 * 100.09\frac{g}{mol} = 0.4004\ g\ CaCO_3$$

Using ultrapure Milli-Q deionized water filtered by Yamato Model SM510, Santa Clara, CA (Millipore, 18.2 MΩ.cm at 22.5 ºC), calcium bicarbonate was prepared from calcium carbonate (Sigma Aldrich, ≥99% reagent grade). 400.32 mg of $CaCO_3$ was added to a 250 mL glass bottle. 200.0 mL of water was then added to the bottle and following all MSDS regulations, CO_2 was bubbled into the solution. CO_2 was introduced for two hours with the reaction resulting in the formation of both carbonic acid, and calcium bicarbonate. Reaction progress was tracked by examining the insoluble calcium carbonate at the bottom of the glass bottle. The solution was then stirred for two more hours. Some precipitate was visible and so the supernatant liquid was transferred into a clean glass bottle. Notably, pH change can occur up to 48 hours after introducing CO_2. Therefore, the solution was left under the hood for two days to let it equilibrate and then refrigerated to maintain solubility.

Synthesis of Magnesium Bicarbonate

The $Mg(HCO_3)_2$ solutions used in all experiments were diluted solutions from a stock solution synthesized in Lee lab. 200 mL of 20 mM $Mg(HCO_3)_2$ (approx.) stock solution was synthesized as follows:

$$Mg(OH)_2 + 2CO_2 \rightleftharpoons Mg(HCO_3)_2 \quad (11)$$

At a 1:1 ratio of $Mg(OH)_2$ to $Mg(HCO_3)_2$ as depicted by the reaction above:

$$\frac{20\ mmol\ Mg(HCO_3)_2}{1\ L} = \frac{20\ mmol\ Mg(OH)_2}{1\ L}$$

$$\frac{20\ mmol\ Mg(OH)_2}{1\ L} = \frac{x\ mmol\ Mg(OH)_2}{0.2\ L}$$

$$x = 4.0x10^{-3}\ mol\ Mg(OH)_2 * 58.32\frac{g}{mol} = 0.2333g\ Mg(OH)_2$$

Using ultrapure Milli-Q deionized water filtered by Yamato Model SM510, Santa Clara, CA (Millipore, 18.2 MΩ.cm at 22.5 ºC), magnesium bicarbonate was prepared from magnesium hydroxide (Sigma Aldrich, 95% reagent grade). 233.0 mg of $Mg(OH)_2$ was added to a 250 mL glass bottle. 200.0 mL of water was then added to the bottle and following all MSDS regulations, CO_2 was bubbled into the solution. CO_2 was introduced for two hours with the reaction resulting in the formation of both carbonic acid, and magnesium bicarbonate. Reaction progress was tracked by examining the insoluble magnesium hydroxide at the bottom of the glass bottle. The solution was then stirred for two more hours. Some precipitate was visible and so the supernatant liquid was transferred into a clean glass bottle. Notably, pH change can occur up to 48 hours after introducing CO_2. Therefore, the solution was left under the hood for two days to let it equilibrate and then refrigerated to maintain solubility.

Flame atomic absorption spectroscopy of Calcium and Magnesium solutions

The concentration of magnesium (Mg^{2+}) and calcium (Ca^{2+}) contained in the prepared $Mg(HCO_3)_2$ and $Ca(HCO_3)_2$ solution was measured by flame atomic absorption spectroscopy

using a Shimadzu Flame Atomic Absorbance Spectrophotometer ASC-7000. For determining the concentration of magnesium (Mg^{2+}), a standard calibration was prepared using magnesium sulfate to make a 7-points standard calibration curve 0 to 2 mg/L. The sample was prepared at two dilutions (DF 1250 and DF 2500) and each diluted sample had its magnesium (Mg^{2+}) concentration measured and the average concentration of the total 6 replicates was calculated. For determining the concentration of calcium (Ca^{2+}), a standard calibration was prepared using calcium chloride to make a 7-points standard calibration curve 0 to 50 mg/L. The sample was prepared at two dilutions (DF 100 and DF 200) and each diluted sample had its calcium (Ca^{2+}) concentration measured and the average concentration of the total 6 replicates was calculated.

Experimental setup for Proton-Cation exchange equilibrium constants

This method was adapted from the procedure previously reported in Saeed et al. (2018).[142] Two ElectroPrep electrolysis systems (Cat no. 741196) from Harvard Apparatus Inc (Holliston, MA) were used. One apparatus was used for electrolysis, and one was used as a control. Both systems had identical functionality, with a cathode chamber, a central sample chamber, and an anode chamber. First, all systems were cleaned using dilute hydrochloric acid, and washed with deionized water and allowed to sit for two days. To determine the effect of divalent calcium (Ca^{2+}) and magnesium (Mg^{2+}) cations on TELP, a membrane system was set up using aluminum (Al) and Teflon (Tf). The aluminum and Teflon used in the experiments were 25-µm and 75-µm thick respectively. Aluminum sheet was cut in circular discs of approximately 2.4 centimeters using a single-edge razor blade and a quarter dollar coin. Similarly, Teflon was cut in circular discs of approximately 2.3 centimeters such that when a Teflon disc was sandwiched in between two aluminum discs, the periphery of the aluminum discs will touch each other. Therefore, the two aluminum discs were connected around the circular edge, since the diameter (2.3 cm) of the Teflon

disc is slightly smaller than that (2.4 cm) of the aluminum discs. Note, the use of an inert Teflon disc (in between the two aluminum discs) is essential to prevent the edge-connected Al-Tf-Al membrane assembly from leaking of any ions even when the two aluminum discs are corroded by TELP and transmembrane-electrostatically localized hydroxide anions (TELA). Aluminum discs were weighed before and after using it in the experiment and the mass was recorded to the tenth microgram.

First, the cathode-facing end of the central sample chamber was sealed with an Al-Tf-Al membrane assembly. As shown in Figure 20, we designated the left side of the membrane assembly (**Al**-Tf-Al) as negative (N) since electrolysis forms a hydroxide (OH^-) monolayer at the liquid-membrane interface. The right side of the membrane assembly (Al-Tf-**Al**) was designated as P', since positively charged protons and cations are induced at this liquid-membrane interface. 1.5 mL of the calcium bicarbonate solution, magnesium bicarbonate solution, or control (DI water) was introduced into the central sample chamber, and then the anode-facing end of the central sample chamber was sealed by the Al-Tf-Al membrane assembly. At the anode-facing end of the central sample chamber, we designated the left side of the membrane assembly (**Al**-Tf-Al) as N' since negatively charged OH^- ions are induced at the liquid-membrane interface (within the central sample chamber) during water electrolysis. Similarly, the right side of the membrane assembly (Al-Tf-**Al**) was designated as P since electrolysis creates a monolayer of H^+ ions (TELP) at this liquid-membrane interface.

The central sample chamber was then inserted into the channel of the septum that connects the anode and cathode chambers. The central sample chamber should fit snugly and become impermeable to any water. After testing for the integrity of the chamber such that it would not move, the cathode chamber was filled to the level of the central sample chamber and the entire

apparatus was tipped carefully to the anode side so that the air bubble (Figure S11) formed at N membrane during filling the cathode chamber was removed. Then, the cathode chamber was filled with water to the max-fill line. After checking for leaks over to the other side, the anode chamber was filled with water to the max-fill line.

The pH values of $Ca(HCO_3)_2$ and $Mg(HCO_3)_2$ solution samples were measured in a separate 1.5 mL Teflon central sample chamber, henceforth referred to as the "reading chamber," prior to the start of the experiment (to avoid contamination from a small amount of ions that may pass through the glass membrane of the pH glass electrode into the solution sample during a pH measurement). Conductance of the water used to fill the cathode and anode chambers was measured in a beaker which was followed by the pH measurements. After setting up the control and experimental apparatuses under the same conditions, an electrolysis voltage of 200 V was applied for 5 hours to the experimental system and the electrolysis current was recorded at an interval of 10 seconds.

At the completion of the allotted time, the voltage source was removed from the apparatus. Conductance of the cathode and anode bulk water phase was measured followed by the pH measurements prior to removing the central sample chamber. Upon removal, the central sample chamber was opened from the P' side and qualitative observations were made of the proton sensing foil membranes and the liquid inside the chamber. Liquid from the central sample chamber was transferred to the reading chamber with a pipette and pH was measured. Proton sensing aluminum membranes were left to dry overnight, and their mass was recorded. Identical measurements were repeated for the control apparatus. The solutions were stored at room temperature in vials for future analysis.

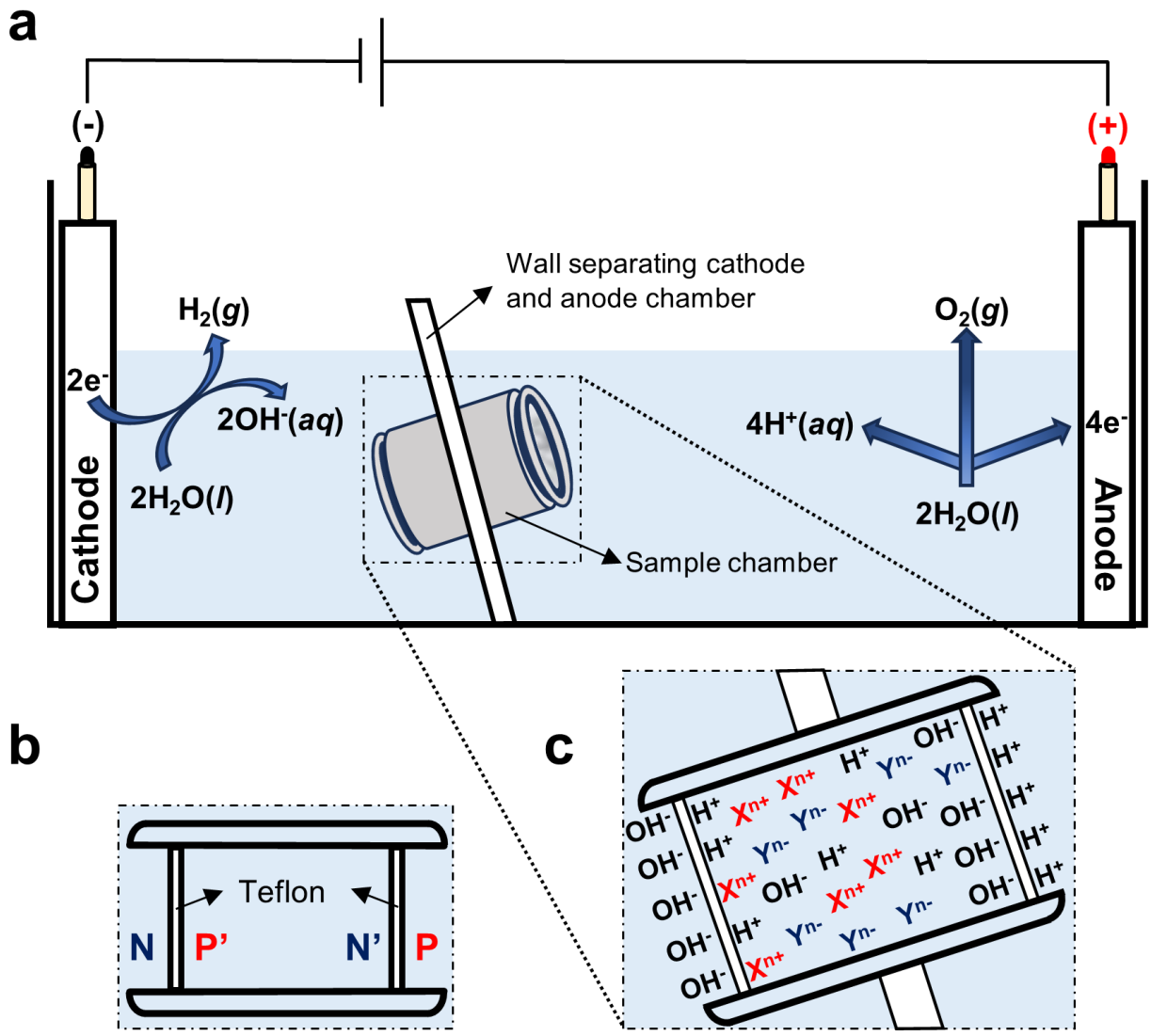

Figure 20. Experimental system design: Cathode (water) Aluminum-Teflon-Aluminum (Solution) Aluminum- Teflon-Aluminum (water) Anode.

(a) Schematic diagram of the system testing the effects of non-proton cations on TELP. (b) Cross-section of central sample chamber with membranes labelled: N and P' (and also N' and P) are the edge-connected Al discs sandwiching a Tf disc. (c) Inset showing the exchange of the added cations (X^{n+}) with the TELP at the P′ side.

The experimental procedures were followed for the control and experimental solutions. Experiments were run for 0 mM (positive control), 0.5, 0.8, 0.9, 1.0, 1.25, 1.5, 3.0, 5.0, 7.5, & 15 mM $Mg(HCO_3)_2$ and for 0 mM (positive control), 0.5, 1.0, 1.5, 2.0, 2.5, 3.0, 5.0, & 10 mM $Ca(HCO_3)_2$. Negative controls without electrolysis were also run and replicates were performed for each electrolysis.

RESULTS AND DISCUSSION

Demonstration of liquid water as protonic conductor

In a 5-hour experiment utilizing 200V-driven water electrolysis, the formation of small gas bubbles was observed at both the platinum electrodes of the anode and cathode (Figure 22). This observation aligns with the established process of water electrolysis, where water is oxidized electrolytically to form molecular oxygen generating protons at the anode water compartment. Similarly, protons are reduced to form molecular hydrogen, leaving an increased presence of hydroxide anions in the cathode water compartment.

Fresh ultrapure water typically exhibits a conductivity of 0.055 µS/cm, which gives a resistivity of 18.2 MΩ-cm. With this low conductivity, pure water is electronically nonconductive as it lacks charge carrier for electrons. During experimental demonstration of liquid water as protonic conductor, an electrolysis DC voltage of 200 V was applied for 5 hours to the experimental system and the electrolysis current was recorded at an interval of 10 seconds. As mentioned earlier, the central sample chamber has an external diameter of 3.2 cm and internal diameter 1.5 cm. Removal of central sample chamber increased the diameter of the liquid water channel for the flow of protons by almost two times, which led to the increase in the DC electrolysis current by around two times. Average electric current of 3 replicates of experiments

with the hollow central sample chamber (without membranes) was 6.4×10^{-5} Amperes, and without the central sample chamber was 1.5×10^{-4} Amperes (Figure 21). This large value for the water electrolysis current is caused by the movement of protons through the water molecules. This observation aligns with the literature findings [158, 159] that protons (H^+) in water exhibit abnormally high mobility (3.62×10^{-3} cm^2 V^{-1} s^{-1}) compared to other ions of similar size. This high mobility of protons in water is due to their ability to participate in rapid proton transfer reactions, which involve the transfer of protons between water molecules.[160, 161] This phenomenon plays a crucial role in various chemical and biological processes. With 1.5×10^{-4} Amperes of current flowing for 5 hours, the total amount of charges (coulombs) that passed through the electrolysis process was calculated to be 2.7 C for the system without central sample chamber. This charge value can only be carried by 1.7×10^{19} protons through the pure water body between the electrodes. The pH of cathode and anode bulk water phase before the start of experiment was (6.02 ± 0.05). After 5 hours of experiment, the pH of cathode and anode bulk water phase were measured at various distances from each of the cathode and anode (Figure S12). The bulk liquid water pH value slightly dropped from the original pH of 6.02 ± 0.05 to 5.86 ± 0.07 but showed negligible difference irrespective of the distance of the water bulk from either the cathode or the anode.

Demonstration of protonic capacitor

During the open-circuit electrolysis of deionized water, excess protons are produced in the anode (P) chamber while excess hydroxide anions are generated in the cathode (N) chamber. According to the TELP theory, the free excess protons in the anode water body would not stay in the bulk liquid phase but localize to the water-membrane (Teflon) interface (the P_I site) in the anode (P) chamber and attract the excess hydroxide ions of the cathode water body to the N_I site at the other side of the membrane, forming an “excess anions-membrane-excess protons”

capacitor-like system (as shown in the inset of Figure 23). Because of this phenomenon, the bulk pH in either the anode water body or the cathode water body is not affected by the excess protons or the excess hydroxide anions created by the water electrolysis process.

The bulk pH measurements in the cathode water body (5.86 ± 0.07) and the anode water body (5.86 ± 0.07) at the end of the experiment with the set up “cathode-water-Tf-water-anode” system were almost identical. Thus, bulk pH is not affected by the excess protons or the excess hydroxide ions created by the water electrolysis process. These free excess protons in the anode water body are localized at the water-membrane (Teflon) interface in the anode chamber and attract the excess hydroxide ions of the cathode water body to the other side of the membrane, forming an “excess anions-membrane-excess protons” capacitor-like system. The membrane thickness of this system is 75 μm. As the thickness of the Teflon membrane increases, the capacitance of the system decreases which is shown by the current measurements (Figure 27).

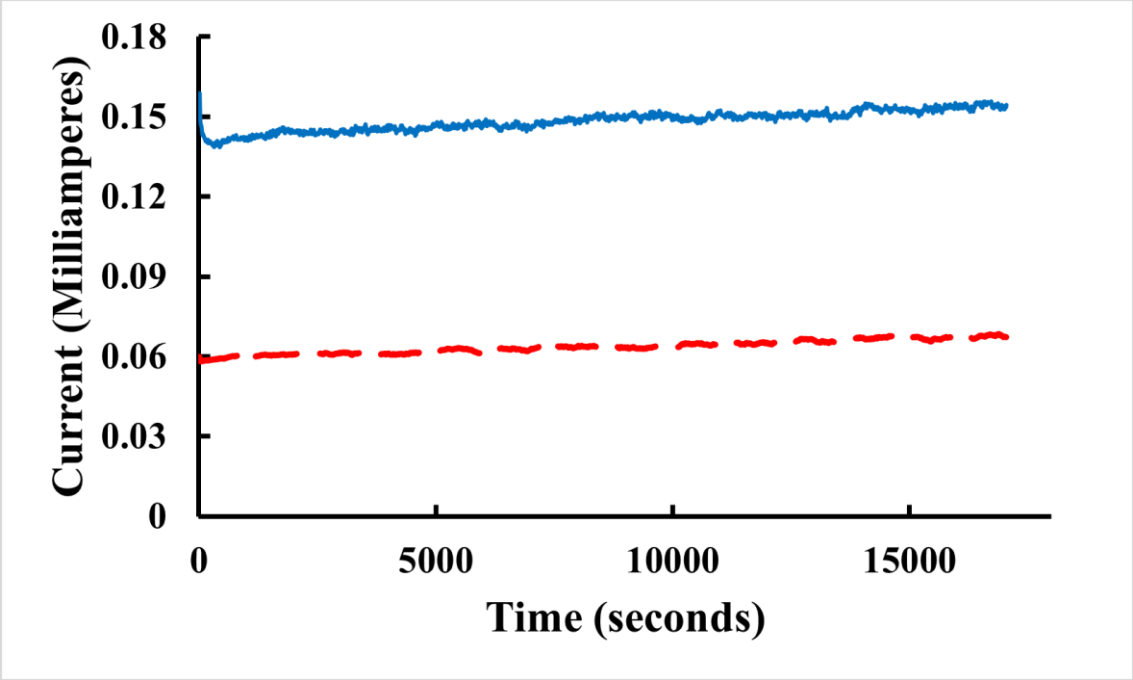

Figure 21. Current versus time data points recorded during 5-hour experiment utilizing 200V-driven water electrolysis when two aqueous phases are not separated by a membrane.

Blue solid line represents the averaged current of three trials of experiment without the central sample chamber in the channel of the septum that separates the cathode chamber from the anode chamber. Red dashed line represents the averaged current of three trials of experiment when the hollow central sample chamber (without membranes) was inserted in the channel of the septum.

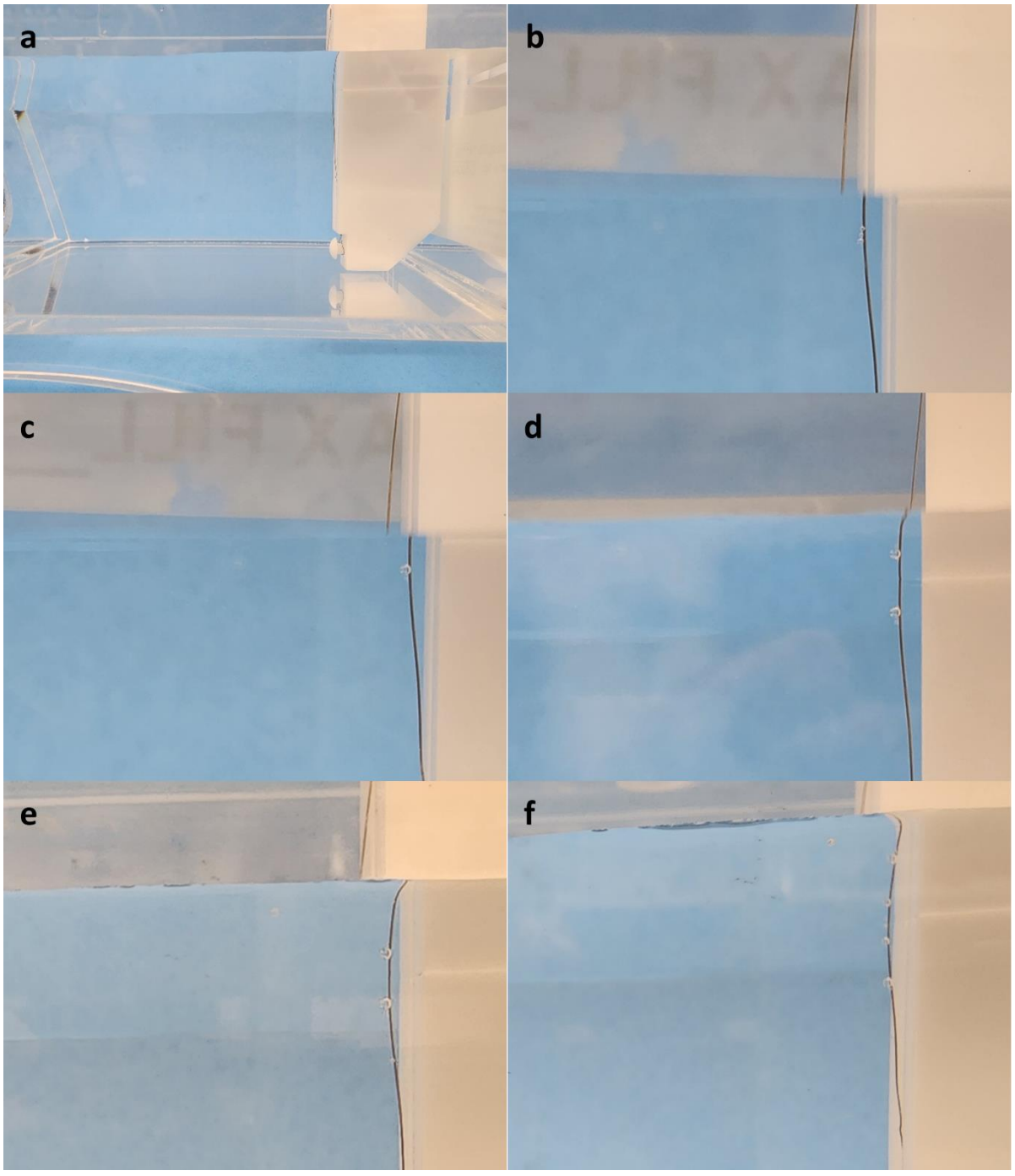

Figure 22. Formation of gas bubbles at platinum electrodes during electrolysis.

(a) No bubbles before the start of experiment. (b) Bubbles formed after 30 minutes. (c) Bubbles formed after 45 minutes. (d) Bubbles formed after 1 hour. (e) Bubbles formed after 1.5 hours. (f) Bubbles formed after 5 hours.

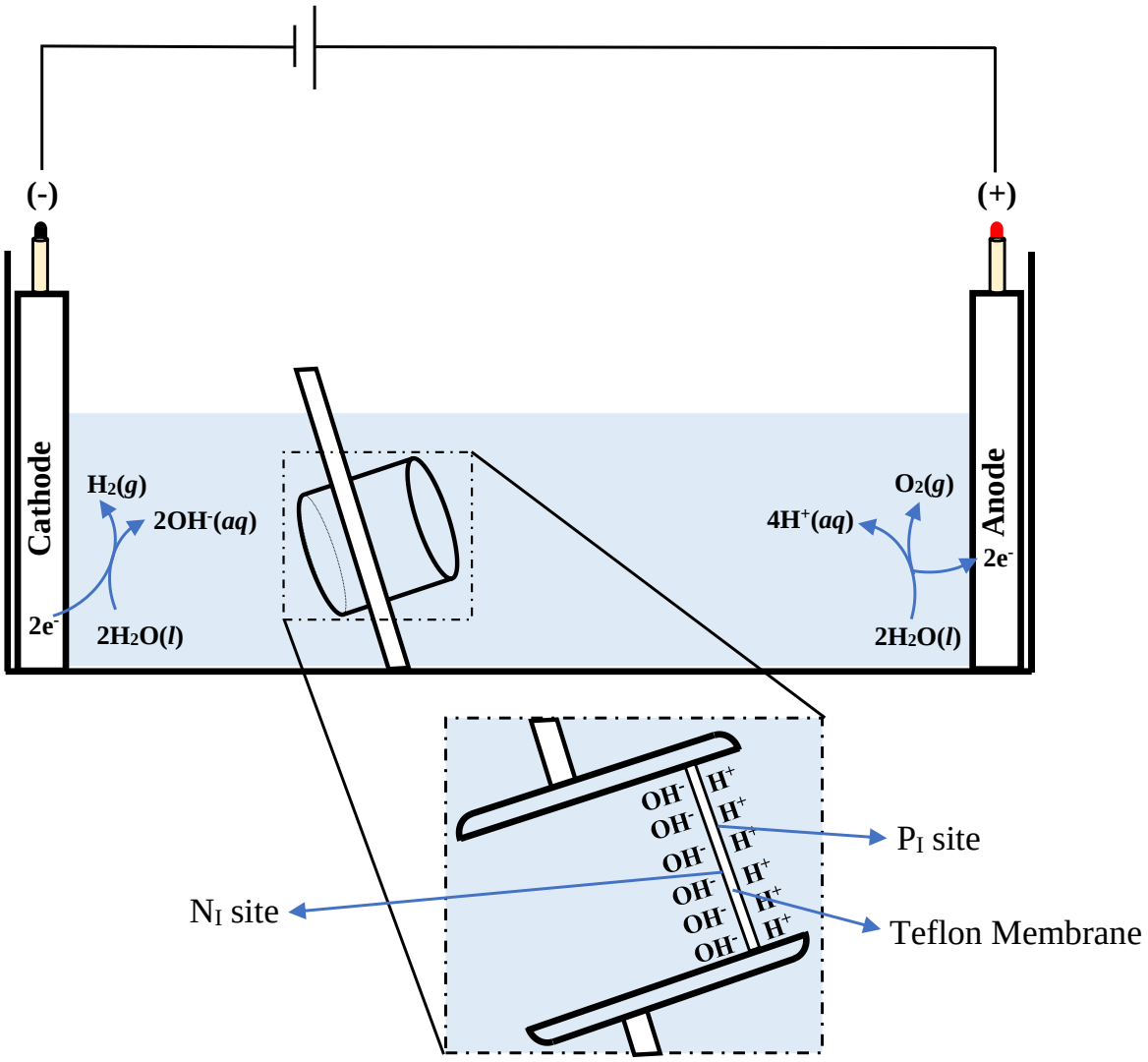

Figure 23. Demonstration of protonic capacitor.

Excess H^+ in the anode water are electrostatically localized at P_I at the water-membrane (Teflon) interface while the excess OH^- in the cathode water chamber are electrostatically attracted to N_I on the other side of membrane, forming a "excess hydroxide anions-membrane-excess protons" capacitor-like system.

In the absence of substances with which aluminum can form soluble complexes or insoluble salts, aluminum remains passive through the formation of oxides when the pH ranges

between 4 and 8.5.[162] In acidic conditions, aluminum forms soluble Al^{3+} ions, while it forms soluble AlO_2^- in alkaline conditions.[162, 163] Experiment run for "cathode-water-Al-Tf-Al-water-anode" system (in which the two Al discs were completely separated by the Tf membrane) however did not result in visible corrosion of the proton sensitive Al surface during the desired time interval. This experiment was run for a week only after which we saw some color development in the Al surface. This indicated that the capacitance developed was not entirely enough for the corrosion of proton sensitive film. For this reason, the Teflon membrane was cut in circular discs of approximately 2.3 centimeters whereas the aluminum sheet was cut in circular discs of approximately 2.4 centimeters. With this setup, when a Teflon disc was sandwiched between two aluminum discs, the periphery of the aluminum discs will touch each other creating an electric connection between the aluminum discs and an increase in capacitance (from the electric double layer of the liquid-Al film interface). Teflon membrane would however not allow any of the protons or hydroxide ions to pass through the membrane. Experiment was run for "cathode-water-Al-Tf-Al-water-anode" system with the new set up which resulted sufficient capacitance observed by visible corrosion of the proton sensitive Al surface during the desired time interval.

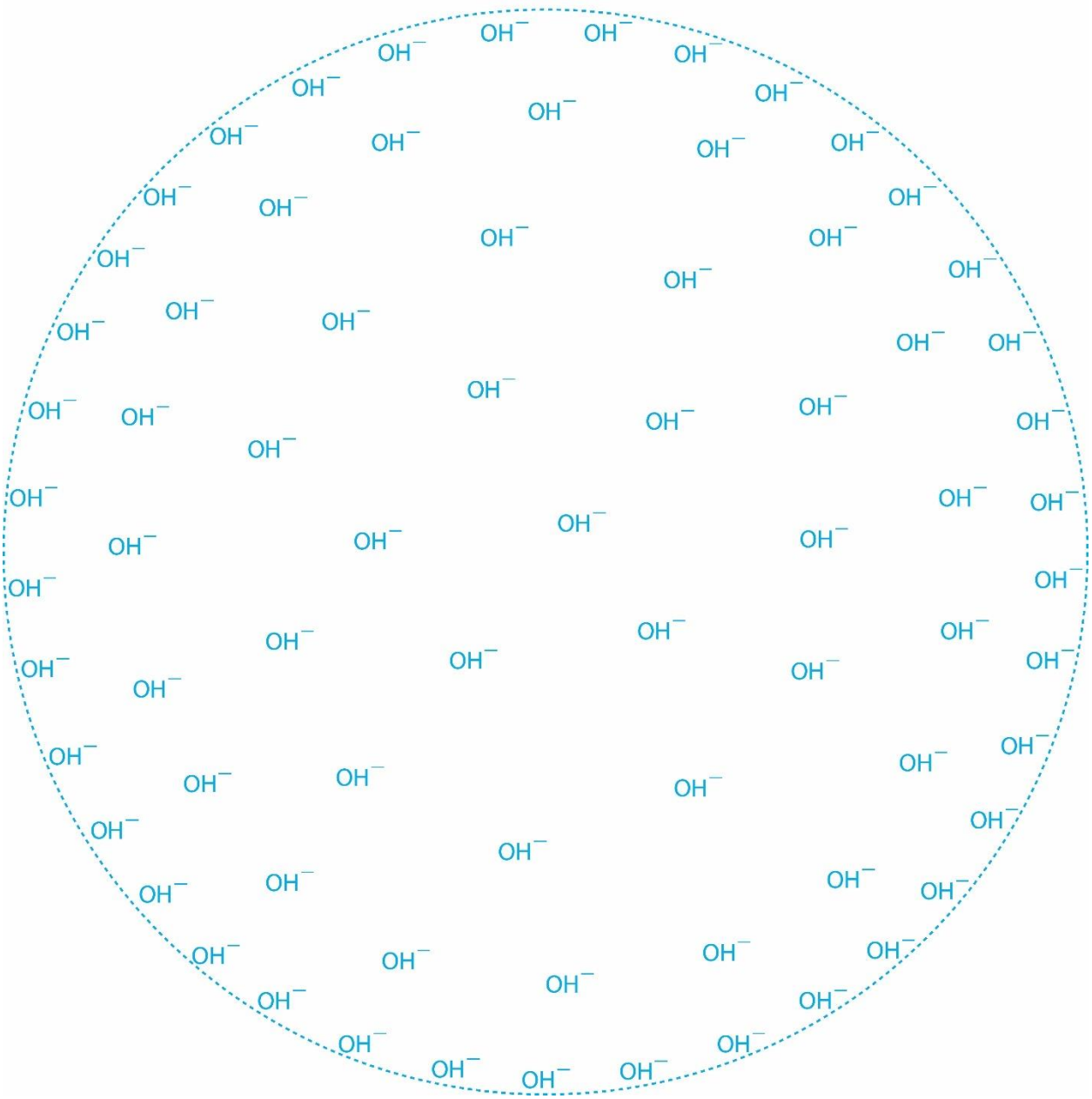

Figure 24. **Distribution of the transmembrane electrostatically localized hydroxide anions.**

This drawing was made by Prof. Lee to illustrate a predicted transmembrane-electrostatically localized hydroxide anions (TELA) disk electrostatic edge effect that makes the density of transmembrane-electrostatically localized hydroxides somewhat higher around the disk edge.

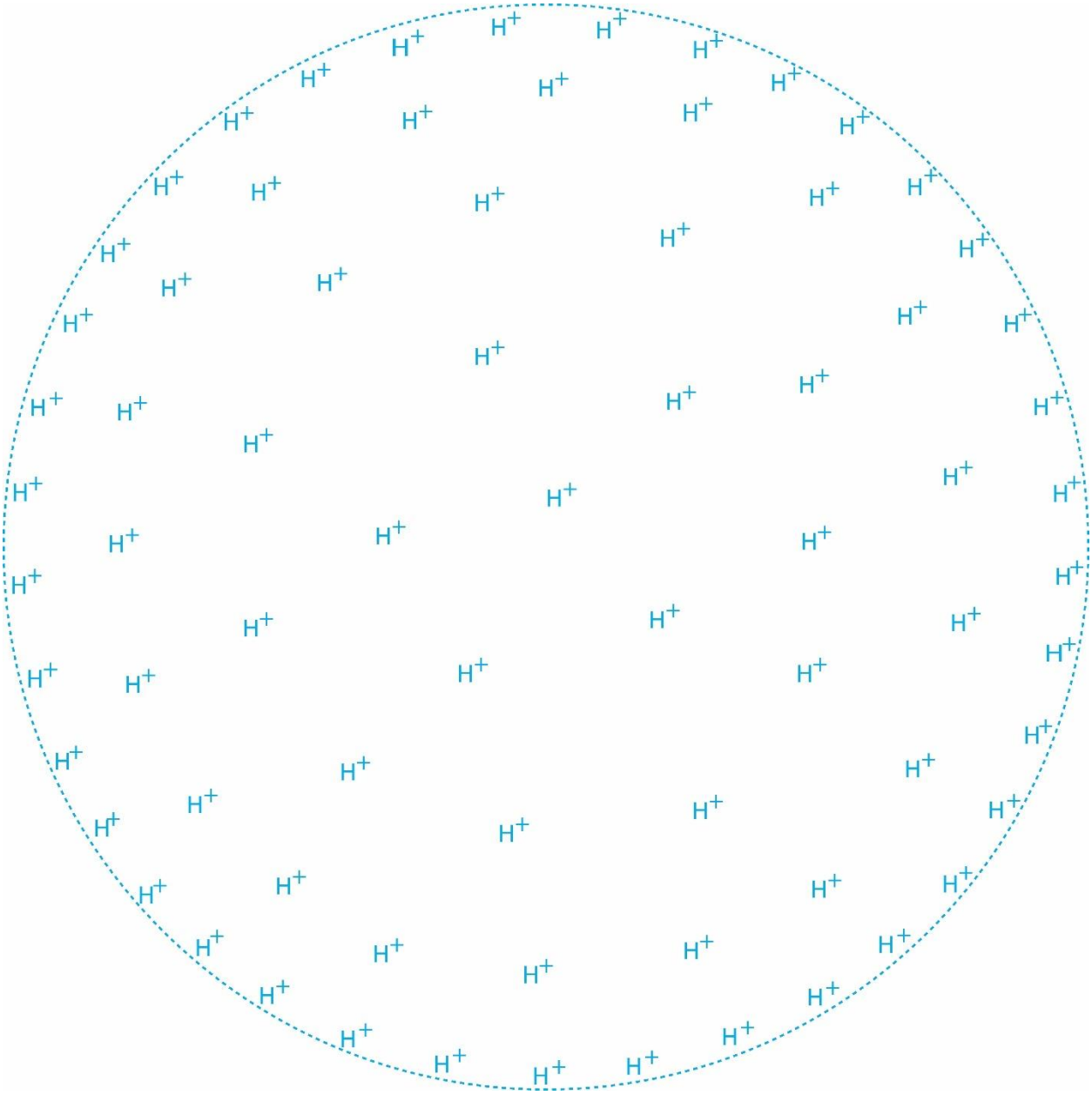

Figure 25. **Distribution of the transmembrane electrostatically localized protons.**

This drawing was made by Prof. Lee to illustrate a predicted transmembrane-electrostatically localized protons (TELP) disk electrostatic edge effect that makes the density of TELP somewhat higher around the disk edge.

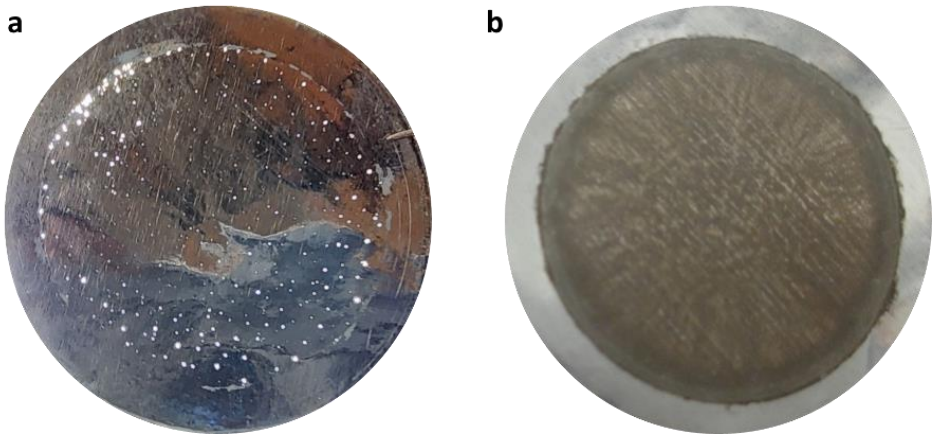

Figure 26. **Alkaline (excess hydroxides) corrosion and acidic (excess protons) corrosion of Aluminum membrane.**

Photograph of (a) N membrane taken against the light showing clusters of pinholes which seems to manifest themselves around the edge of the membrane. (b) P membrane showing corrosion as visible brown deposits all over the exposed surface with the edge showing thicker deposits.

The experimental observations of protonic corrosion in aluminum surface revealed the presence of brown deposits. On the other hand, hydroxide corrosion exhibited more aggressive behavior leading to creation of holes in the aluminum surface. For the experiment involving edge connected Al-Tf-Al system, P membrane has almost uniform brown deposit all over the exposed surface with the edge showing thicker deposits, whereas N membrane has clusters of pinholes which seems to manifest themselves around the edge of the membrane (Figure 26). This edge effect of the transmembrane electrostatically localized proton and hydroxide anions is caused by the repulsion between same charged ions along the flat membrane surface increasing the ion density around the edge as detailed in Figure 24 and Figure 25. This finding is similar to the geometric effect of the mitochondrial cristae enhancing the transmembrane electrostatically

localized proton density to the ellipsoidal crista ridges in comparison to the crista flat region.[71] This discovery also aligns notably well with a study, which demonstrates a 3.5-fold rise in surface charge density on the curved membrane surface in comparison to the flat membrane.[164]

The distinct corrosion behaviors observed between N membrane undergoing alkaline (hydroxide) corrosion and P membranes undergoing acidic (protonic)corrosion suggest a nuanced interaction with the surrounding environment. The alkaline corrosion of N membrane is attributed by the presence of localized OH^- ions at the liquid-membrane interface and their specific interaction with the membrane material. On the other hand, acidic corrosion of P membranes implies a reaction with localized H^+ present at the liquid-membrane interface. The plot of electrolysis current versus time for the edge connected Al-Tf-Al system and the edge unconnected Al-Tf-Al system is shown in Figure 28.

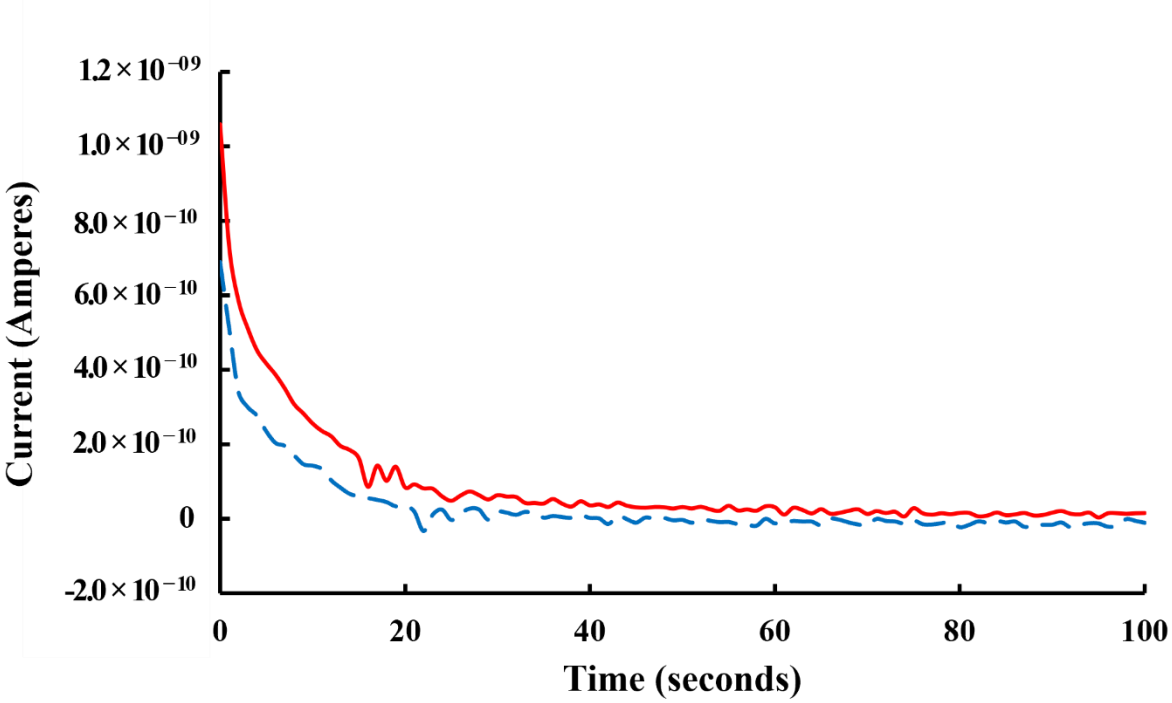

Figure 27. Current versus time data points for the experimental system with Teflon.

Average current for the first 100 seconds of three replicates of the system with various membrane thickness. Red solid line represents the "cathode-water-Tf-water-anode" system with membrane thickness 75 µm, and blue dashed line represents the "cathode-water-Tf-water-Tf-water-anode" system with membrane thickness 150 µm.

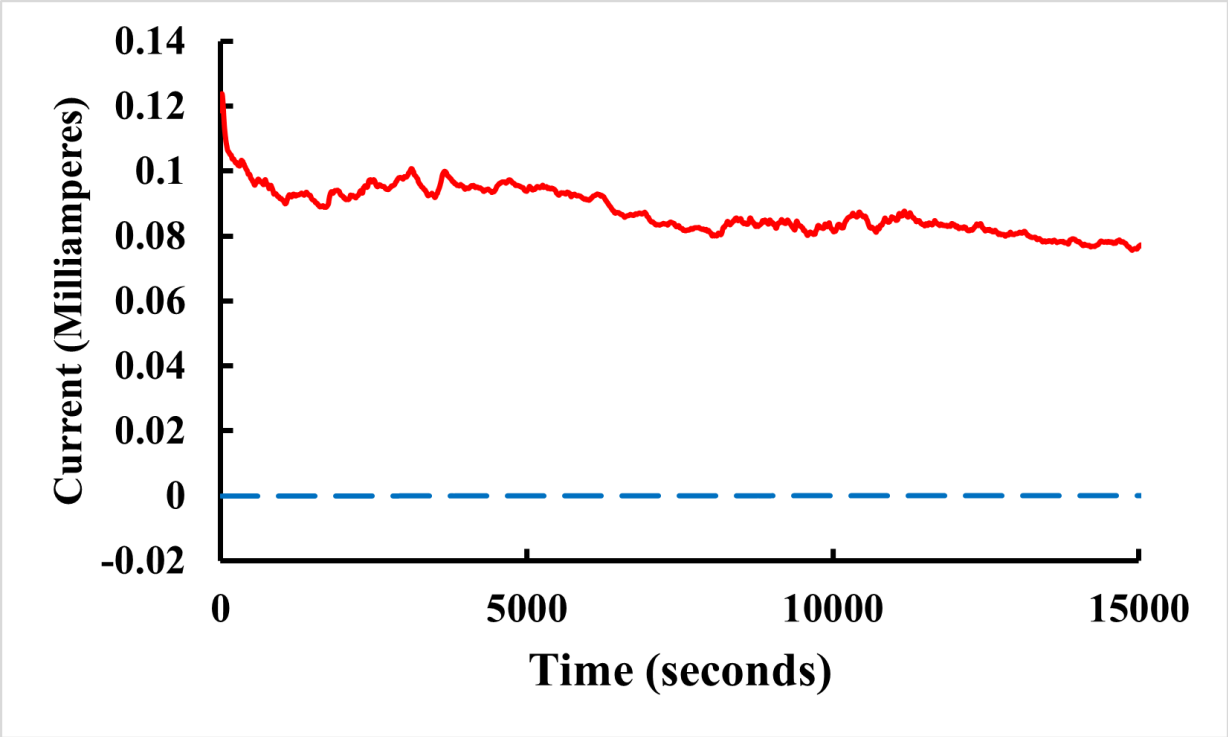

Figure 28. Current versus time data points for the experimental system with Aluminum. Averaged electrolysis current for three replicates of edge connected Al-Tf-Al system represented by red solid line, and averaged electrolysis current for three replicates of the edge unconnected Al-Tf-Al system represented by blue dashed line.

Flame atomic absorption spectroscopy of Calcium and Magnesium

The concentration of calcium (Ca^{2+}) contained in the liquid suspension of the diluted $Ca(HCO_3)_2$ solution was measured to be 4.1 mg/L (±0.04 mg/L). With that value, the final concentration of the stock solution was calculated to be 10 mM. Similarly, the concentration of magnesium (Mg^{2+}) contained in the liquid suspension of the diluted $Mg(HCO_3)_2$ solution was measured to be 0.29 mg/L (±0.03 mg/L). With that value, the final concentration of the stock solution was calculated to be 15 mM.

Proton-Cation exchange equilibrium constant of Ca^{2+}

The concentration calcium (Ca^{2+}) in the liquid suspension of the synthesized $Ca(HCO_3)_2$ solution was measured to be 10 mM based on the flame atomic absorption measurements. $Ca(HCO_3)_2$ solution with concentration of Ca^{2+} greater than 10 mM could not be synthesized in normal conditions.

The alkaline corrosion of N/N' membranes is attributed by the presence of localized OH^- ions at the liquid-membrane interface and their specific interaction with the membrane material. On the other hand, acidic corrosion of P/P' membranes imply a reaction with localized H^+ present at the liquid-membrane interface. The extent of corrosion for P' aluminum is in negative correlation with the concentration of the $Ca(HCO_3)_2$ solution used in the central sample chamber during the experiment, whereas the extent of corrosion for P aluminum is almost same for all concentrations. The experimental observations of acidic corrosion in aluminum surface revealed the presence of brown deposits (Figure 29). On the other hand, alkaline corrosion exhibited more aggressive behavior leading to creation of holes in the aluminum surface (Figure 30). For the experiment involving 0 mM (positive control), P' membrane has almost uniform brown deposit all over the exposed surface with the edge showing thicker deposits, whereas N membrane has ring of clusters of pinholes which seems to manifest themselves towards the edge of the membrane. Experiments involving 10 mM $Ca(HCO_3)_2$ shows almost no corrosion in P' membrane. Visual results as displayed in Figure 29 suggests that 2.0 mM $Ca(HCO_3)_2$ serves as about the 50% corrosion point on the aluminum P' membrane. The corrosion of aluminum membranes is also attributed with a change in mass of the membrane as shown in Table 14. Negative controls (0V) for all $Ca(HCO_3)_2$ concentrations does not incur any form of corrosion of the aluminum membranes and mass change.

Table 14. Change in pH of central sample chamber, change in mass of P' and $K_{pCa^{2+}}$ for various concentrations of $Ca(HCO_3)_2$, before and after the experiment at 200 V.

$[Ca^{2+}]$	**Initial pH**	**Final pH**	**Change in mass of P'** (mg)	**$K_{pCa^{2+}}$** (Using initial pH)	**$K_{pCa^{2+}}$** (Using final pH)
0 mM	*6.02 ± 0.11*	*7.89 ± 0.15*	*0.08 ± 0.02*	*NA*	*NA*
0.5 mM	*8.05 ± 0.02*	*8.51 ± 0.09*	*0.06 ± 0.02*	*(1.8 ± 0.1) x 10^{-5}*	*(6.2 ± 1.8) x 10^{-6}*
1.0 mM	*8.07 ± 0.02*	*8.87 ± 0.13*	*0.02 ± 0.01*	*(8.5 ± 0.6) x 10^{-6}*	*(1.4 ± 0.6) x 10^{-6}*
1.5 mM	*8.00 ± 0.03*	*8.27 ± 0.11*	*0.01 ± 0.02*	*(6.7 ± 0.7) x 10^{-6}*	*(3.7 ± 1.3) x 10^{-6}*
2.0 mM	*8.12 ± 0.02*	*8.81 ± 0.09*	*0.02 ± 0.01*	*(3.8 ± 0.3) x 10^{-6}*	*(7.9 ± 2.3) x 10^{-7}*
2.5 mM	*8.06 ± 0.01*	*7.18 ± 0.07*	*(-0.05 ± 0.01)*	*(3.5 ± 0.1) x 10^{-6}*	*(2.7 ± 0.6) x 10^{-5}*
3.0 mM	*8.02 ± 0.03*	*6.64 ± 0.08*	*(-0.09 ± 0.03)*	*(3.2 ± 0.3) x 10^{-6}*	*(7.8 ± 2.0) x 10^{-5}*
5.0 mM	*7.99 ± 0.03*	*8.54 ± 0.07*	*0.05 ± 0.02*	*(2.1 ± 0.2) x 10^{-6}*	*(5.8 ± 1.3) x 10^{-7}*
10 mM	*7.84 ± 0.03*	*8.02 ± 0.09*	*0.04 ± 0.01*	*(1.5 ± 0.1) x 10^{-6}*	*(9.8 ± 2.8) x 10^{-7}*

At the start of all experiments including the positive and negative controls, the volume of liquid in the central sample chamber is 1.5 mL. A consistent decrease in the volume of liquid in the central sample chamber correlating with the extent of corrosion is observed. The corrosion process results in the formation of a white solid precipitate that could account for the reduction in liquid volume. Reduction in volume is observed in the range of 5% to 50%.

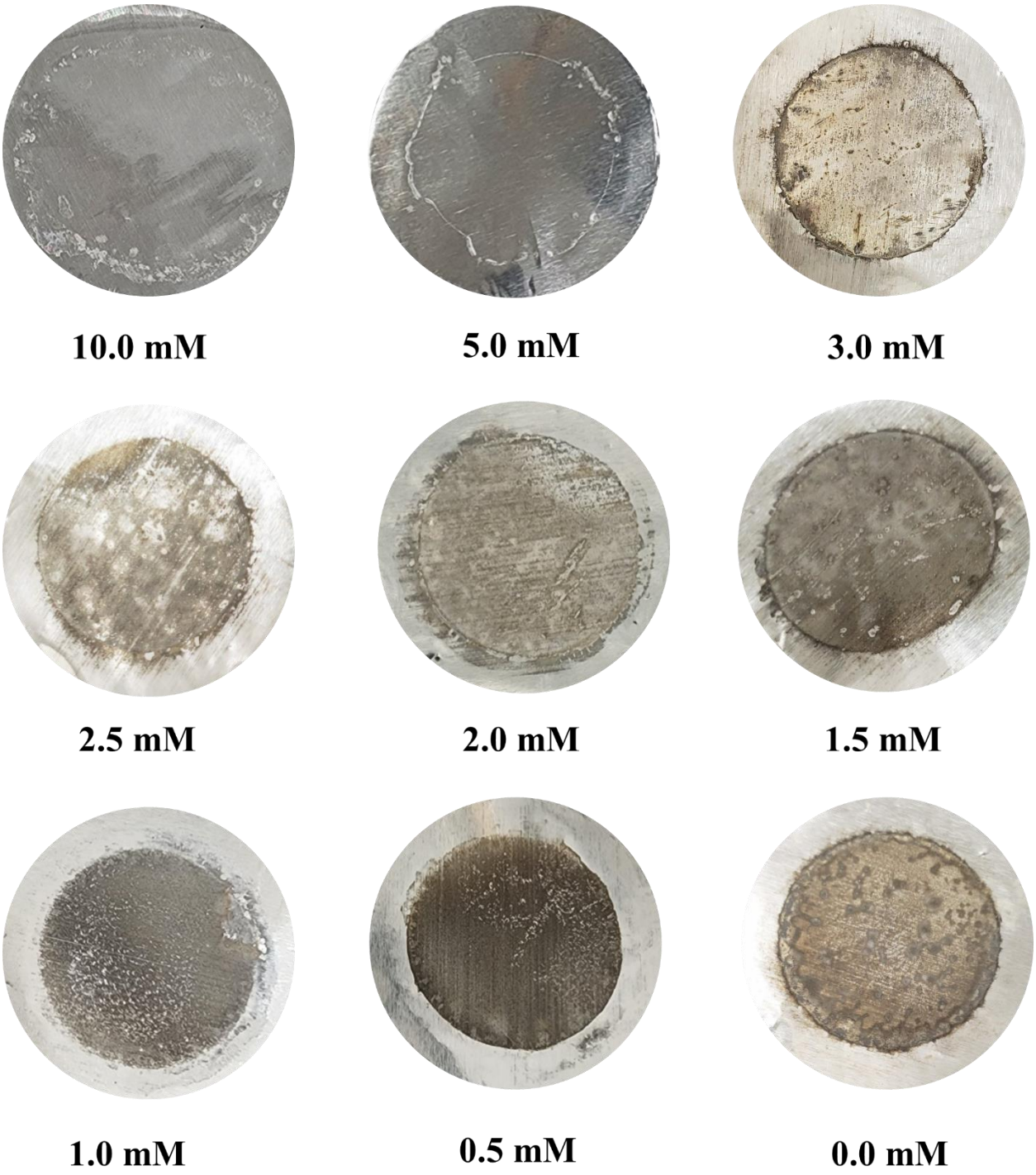

Figure 29. Digital images of P' aluminum membranes **s**howing extent of acidic corrosion in the surface of aluminum revealed by the presence of brown deposits in varying concentrations of $Ca(HCO_3)_2$ solution.

10 mM $Ca(HCO_3)_2$ had a pH of 7.84 ± 0.03 before starting the experiment with a slight increase in pH to 8.02 ± 0.09 after 5 hours experiment. Table 16 summarizes the pH values of the central sample chamber before the start of experiment and after 5 hours experiment at 200 V for all the concentrations of $Ca(HCO_3)_2$. There was an overall increase in pH of the liquid in central sample chamber after 5 hours experiment involving $Ca(HCO_3)_2$ solution with the drop in pH observed only for 2.5 mM and 3.0 mM $Ca(HCO_3)_2$. Excluding these two $Ca(HCO_3)_2$ concentrations, average of the pH of central sample chamber was 8.05 ± 0.05 before starting the experiment with an overall increase in pH to 8.60 ± 0.24 after 5 hours experiment at 200V. For the experiment involving 0 mM (positive control), pH changes from 6.02 ± 0.11 in the beginning to 7.89 ± 0.15 at the stop of the experiment. Negative controls (0V) for all $Ca(HCO_3)_2$ concentrations does not incur any significant changes in pH as well as the volume of the central sample chamber solution.

Formation of H_2 gas can occur at the P' interface during the aluminum surface corrosion according to the reactions:

$$Al_2O_3(s) + 6H^+(localized) \leftrightarrow 2Al^{3+} + 3H_2O \quad (12)$$

$$2Al\,(s) + 6H^+(localized) + 6OH^- \rightarrow 2Al(OH)_3 + 3H_2(g) \quad (13)$$

Gas formation exerts pressure on the Aluminum membranes, potentially allowing leakage of the salt solution into the cathode chamber. Salt solution in the cathodic chamber indicates a malfunction in the central sample chamber or the presence of gas formation.

The bulk phase pH and conductivity measurements were conducted before the start and at the end of each experiment. Water used to fill the cathode and anode chamber had a starting pH of 6.07 ± 0.12 and conductivity of 1.380 ± 0.264 µS respectively. After 5 hours of experiment at 200V, pH of the cathode bulk slightly increased to 6.16 ± 0.11 and conductivity slightly decreased to 1.323 ± 0.220 µS. On the other hand, pH of the anode bulk slightly decreased to 5.97 ± 0.10 and conductivity slightly increased to 1.561 ± 0.301 µS. For negative controls (0V), pH of both the cathode and anode bulk slightly decreased to 6.00 ± 0.11 and 5.95 ± 0.07 respectively. Also, conductivity of both the cathode and anode bulk slightly increased to 1.554 ± 0.267 µS and 1.598 ± 0.285 µS respectively.

There are two points of interest in investigating cation equilibrium exchange. The first is the mid-point, where 50% of protons have exchanged with the magnesium/calcium cations. In the case of monovalent cations, this was signified by 50% corrosion on the P’ membrane. The second point of interest is total proton-delocalization. This occurs when calcium cations effectively exchange with protons beyond the point of aluminum detection.

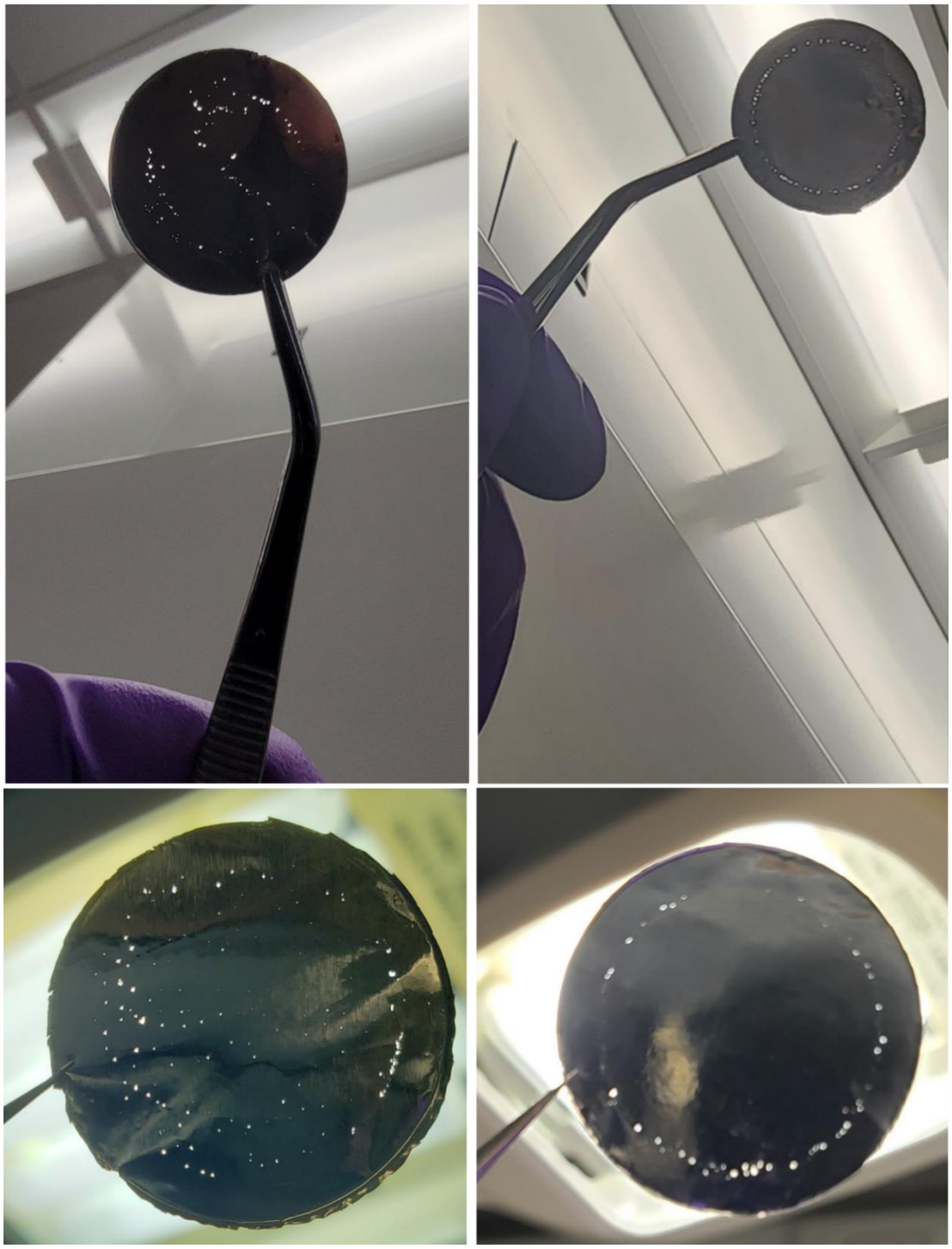

Figure 30. Photograph of various N aluminum membrane taken against the light.

Images shows alkaline corrosion of N aluminum membranes creating clusters of pinholes only visible against light which seems to manifest themselves around the edge of the membrane.

The cation exchange equilibrium constant (K_p) can be expressed as:

$$K_p = \frac{\left[{Ca_L}^{2+}\right] \cdot [H^+]}{[H_L^+] \cdot [Ca^{2+}]} \quad (14)$$

${Ca_L}^{2+}$ signifies the localized calcium cations at the P' membrane, and H_L^+ signifies the localized protons at the P membrane. When the concentrations of ${Ca_L}^{2+}$ and H_L^+ are equal, cation exchange equilibrium constant (K_p) is therefore calculated as:

$$K_{pCa^{2+}} = \frac{[H^+]}{[Ca^{2+}]} \quad (15)$$

Calculated values of $K_{pCa^{2+}}$ for all the concentrations of $Ca(HCO_3)_2$ has been listed in Table 14. The equilibrium constants were calculated with a focus on the mid-point, where 50% of H^+ have exchanged with the Ca^{2+}. Our data suggests that 2.0 mM $Ca(HCO_3)_2$ serves as about the 50% corrosion point on the aluminum P' membrane. The plot of electrolysis current versus time for the experiment involving various $Ca(HCO_3)_2$ concentrations is shown in Figure 31. After three replications, the pH before the experiment was 8.12 ± 0.02 and after the experiment was 8.81 ± 0.09. $K_{pCa^{2+}}$ at 2.0 mM $Ca(HCO_3)_2$ is calculated as $10^{-(8.12 \pm 0.02)}$ M /0.002 M = (3.8 ± 0.3) x 10^{-6} using initial pH whereas $10^{-(8.81 \pm 0.09)}$ M /0.002 M = (7.9 ± 2.3) x 10^{-7} using final pH. Using the final pH at 3.0 mM $Ca(HCO_3)_2$, $K_{pCa^{2+}}$ is calculated as $10^{-(6.64 \pm 0.08)}$ M /0.003 M = (7.8 ± 2.0) x

10^{-5} which is the largest calculated value. Similarly, using the final pH at 5.0 mM $Ca(HCO_3)_2$, $K_{pCa^{2+}}$ is calculated as $10^{-(8.54 \pm 0.07)}$ M /0.005 M = (5.8 ± 1.3) x 10^{-7} which is the smallest calculated value. A previous study determined sodium cation equilibrium exchange and potassium cation exchange to be (5.07 ± 0.46) x 10^{-8} and (6.93 ± 0.91) x 10^{-8} respectively.[142] This effectively puts calcium at an exchange of approximately up to 75 times greater than sodium and 55 times greater than potassium at 50% corrosion.

Proton-Cation exchange equilibrium constant of Mg^{2+}

The concentration of magnesium (Mg^{2+}) in the synthesized $Mg(HCO_3)_2$ solution was measured to be 15 mM based on the flame atomic absorption measurements.. $Mg(HCO_3)_2$ solution with concentration of Mg^{2+} greater than 15 mM could not be synthesized in normal conditions. Corrosion behavior and its extent followed almost same pattern as in $Ca(HCO_3)_2$ solution. Experiments involving 15 mM $Mg(HCO_3)_2$ shows almost no corrosion in P' and N membranes. Visual results as displayed in Figure 32 suggests that 1.25 mM $Mg(HCO_3)_2$ serves as the 50% corrosion point on the aluminum P' membrane. The plot of current versus time for the experiments involving various $Mg(HCO_3)_2$ concentrations is shown in Figure 34. The corrosion of aluminum membranes is also attributed with a change in mass of the membrane as shown in Table 15. Negative controls (0V) for all $Mg(HCO_3)_2$ concentrations does not incur any form of corrosion of the aluminum membranes and mass change. Changes in pH and conductivity of cathode and anode bulk also followed similar pattern for both $Mg(HCO_3)_2$ and $Ca(HCO_3)_2$.

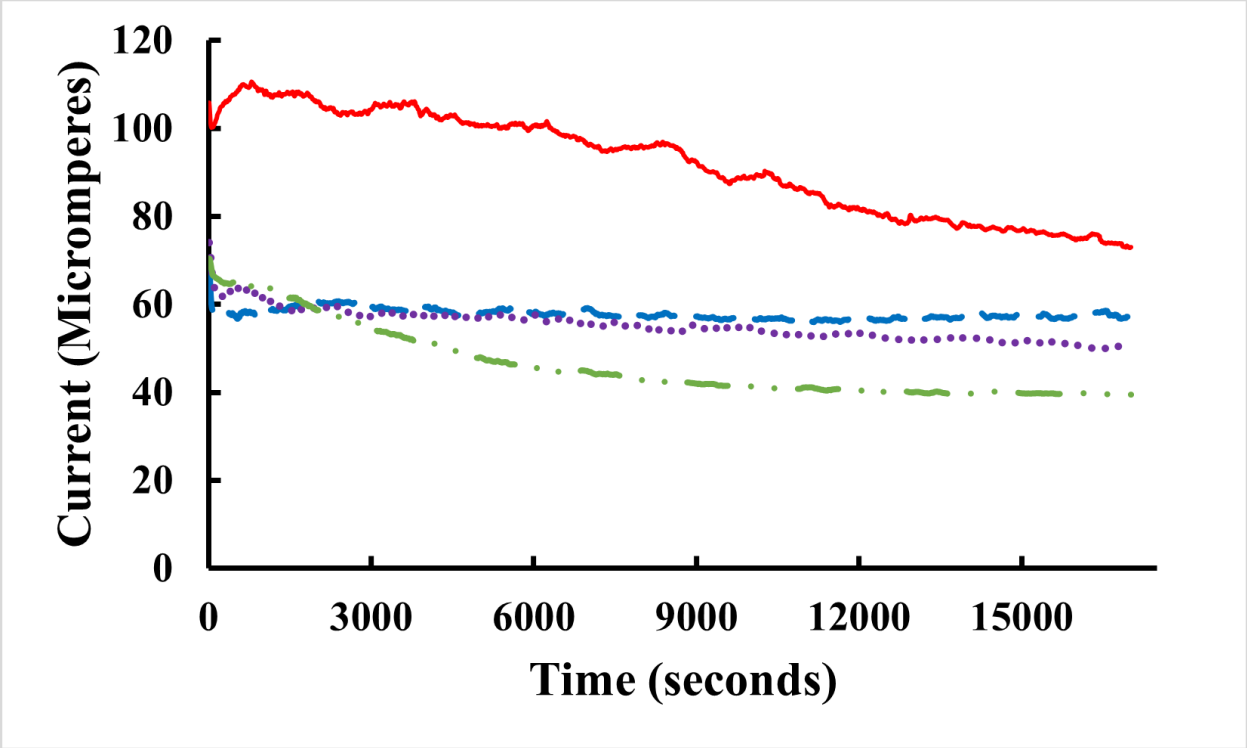

Figure 31. Current versus time data points for the experiments with $Ca(HCO_3)_2$.

Average current of three replicates for 5-hour experiment with the set up "cathode-water-(Al-Tf-Al)-$Ca(HCO_3)_2$-(Al-Tf-Al)-water-anode" and various $Ca(HCO_3)_2$ concentrations. Red solid line represents the experiment run with 0.5 mM $Ca(HCO_3)_2$ in the central sample chamber, blue dashed line represents the experiment run with 2 mM $Ca(HCO_3)_2$ in the central sample chamber, purple dotted line represents the experiment run with 10 mM $Ca(HCO_3)_2$ in the central sample chamber, and green dashed (with dots) line represents the experiment run with 0 mM $Ca(HCO_3)_2$ in the central sample chamber.

15 mM $Mg(HCO_3)_2$ had a pH of 8.30 ± 0.02 before the start of experiment with a slight increase in pH to 8.45 ± 0.12 after 5 hours experiment at 200V. There was an overall decrease in pH of the central sample chamber in the experiments involving all other $Mg(HCO_3)_2$ solutions. Table 17 summarizes the pH values of the central sample chamber before the start of experiment

and after 5 hours experiment at 200V for all the concentrations of $Mg(HCO_3)_2$. For the experiments involving concentration of $Mg(HCO_3)_2$ in between 0.5 mM to 7.5 mM the average of the pH of central sample chamber was 8.20 ± 0.08 before starting the experiment with an overall decrease in pH to 7.15 ± 0.87. There was a drastic drop in the pH of central sample chamber for the experiments involving concentration of $Mg(HCO_3)_2$ in between 1.0 mM to 3.0 mM (average pH before starting the experiment being 8.21 ± 0.07 whereas average pH after 5 hours experiment at 200V being 6.11 ± 0.12) despite of the consumption of H^+ as indicated by the proton sensing aluminum membranes. For the experiment involving 0 mM (positive control), pH changes from 5.99 ± 0.13 in the beginning to 8.02 ± 0.07 at the stop of the experiment. Negative controls (0 V) for all $Mg(HCO_3)_2$ concentrations does not incur any significant changes in pH as well as the volume of the central sample chamber solution.

The cation exchange equilibrium constant (K_p) can be expressed as:

$$K_p = \frac{\left[{Mg_L}^{2+}\right] \cdot [H^+]}{[H_L^+] \cdot [Mg^{2+}]} \tag{16}$$

${Mg_L}^{2+}$ signifies the localized magnesium cations at the P' membrane, and H_L^+ signifies the localized protons at the P membrane. When concentrations of ${Mg_L}^{2+}$ and H_L^+ are equal, the cation exchange equilibrium constant (K_p) is therefore calculated as:

$$K_{pMg^{2+}} = \frac{[H^+]}{[Mg^{2+}]} \tag{17}$$

Table 15. Change in pH of central sample chamber, change in mass of P' and $K_{pMg^{2+}}$ for various concentrations of $Mg(HCO_3)_2$ before and after the experiment at 200 V

$[Mg^{2+}]$	**Initial pH**	**Final pH**	**Change in mass of P'** (mg)	**$K_{pMg^{2+}}$** (Using initial pH)	**$K_{pMg^{2+}}$** (Using final pH)
0 mM	*5.99 ± 0.13*	*8.02 ± 0.07*	*0.11 ± 0.03*	*NA*	*NA*
0.5 mM	*8.04 ± 0.02*	*8.01 ± 0.14*	*0.05 ± 0.01*	*(1.8 ± 0.1) x 10^{-5}*	*(2.1 ± 0.9) x 10^{-5}*
0.8 mM	*8.18 ± 0.02*	*6.82 ± 0.11*	*(-0.02 ± 0.01)*	*(8.3 ± 0.5) x 10^{-6}*	*(2.0 ± 0.7) x 10^{-4}*
0.9 mM	*8.24 ± 0.02*	*7.70 ± 0.12*	*0.14 ± 0.01*	*(6.4 ± 0.4) x 10^{-6}*	*(2.3 ± 0.9) x 10^{-5}*
1.0 mM	*8.29 ± 0.01*	*7.95 ± 0.11*	*0.01 ± 0.02*	*(5.1 ± 0.2) x 10^{-6}*	*(1.2 ± 0.4) x 10^{-5}*
1.25 mM	*8.28 ± 0.02*	*6.25 ± 0.15*	*0.12 ± 0.02*	*(4.2 ± 0.3) x 10^{-6}*	*(4.8 ± 2.2) x 10^{-4}*
1.5 mM	*8.20 ± 0.02*	*6.02 ± 0.21*	*0.17 ± 0.03*	*(4.2 ± 0.3) x 10^{-6}*	*(7.1 ± 4.5) x 10^{-4}*
3.0 mM	*8.14 ± 0.02*	*6.06 ± 0.12*	*0.21 ± 0.04*	*(2.4 ± 0.2) x 10^{-6}*	*(3.0 ± 1.2) x 10^{-4}*
5.0 mM	*8.17 ± 0.02*	*7.47 ± 0.10*	*0.09 ± 0.03*	*(1.4 ± 0.1) x 10^{-6}*	*(7.0 ± 2.2) x 10^{-6}*
7.5 mM	*8.25 ± 0.03*	*8.07 ± 0.11*	*0.14 ± 0.04*	*(7.5 ± 0.7) x 10^{-7}*	*(1.2 ± 0.4) x 10^{-6}*
15 mM	*8.30 ± 0.02*	*8.45 ± 0.12*	*0.08 ± 0.02*	*(3.3 ± 0.2) x 10^{-7}*	*(2.5 ± 0.9) x 10^{-7}*

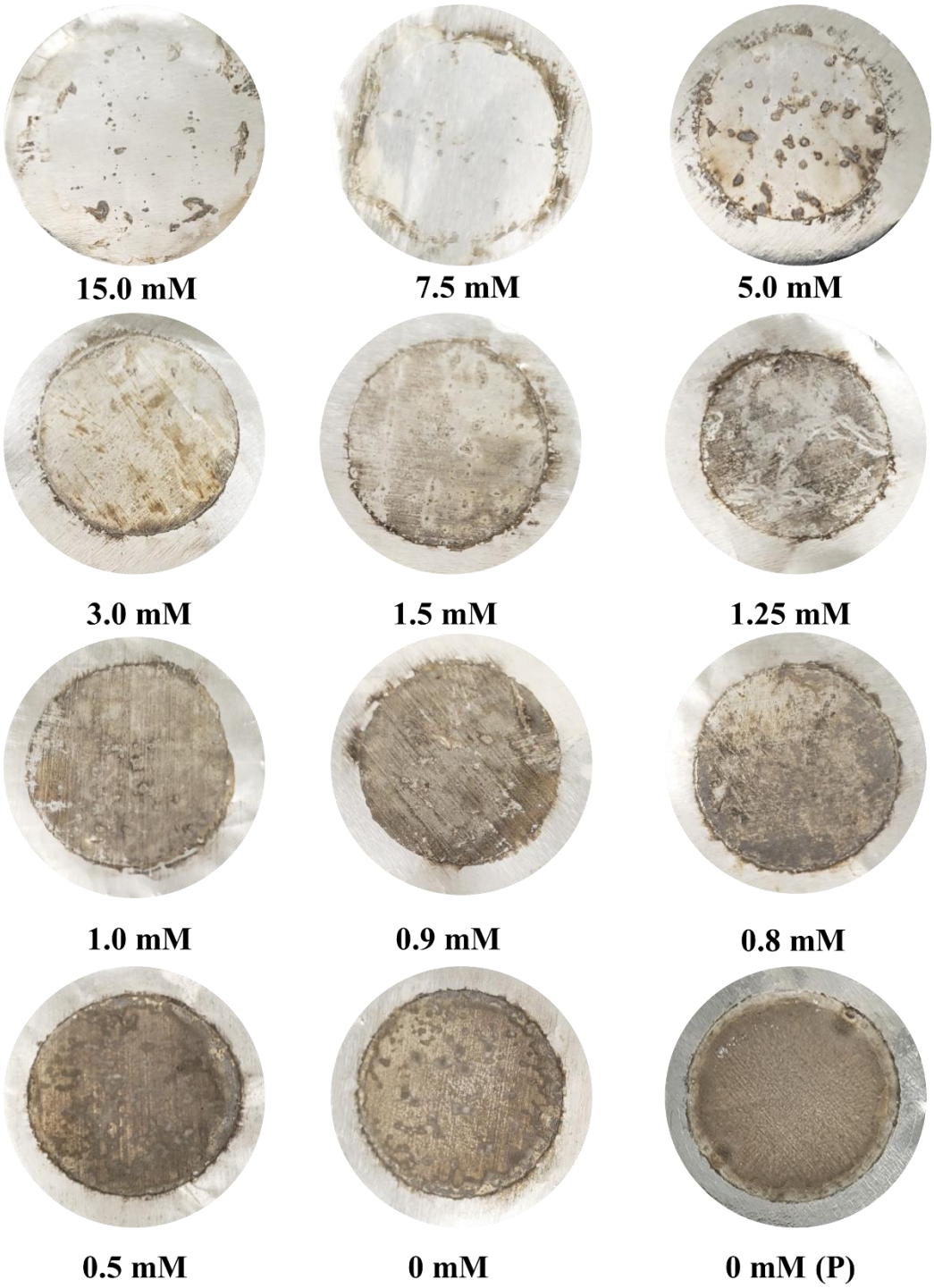

Figure 32. Digital images of P' aluminum membranes **s**howing extent of acidic corrosion in the surface of aluminum revealed by the presence of brown deposits in varying concentrations of $Mg(HCO_3)_2$ along with a typical P aluminum membrane.

Calculated values of $K_{pMg^{2+}}$ for all the concentrations of $Mg(HCO_3)_2$ has been listed in Table 15. Our data suggests 1.25 mM $Mg(HCO_3)_2$ serves as about the 50% corrosion point on the aluminum P' membrane. After three replications, the pH before the experiment was 8.28 ± 0.02 and after the experiment was 6.25 ± 0.15. Had localized concentrations of cations and protons been equal at this point, we would have an equilibrium constant of $10^{-(8.28 \pm 0.02)}$ M /0.00125 M= (4.2 ± 0.3) x 10^{-6} using initial pH, that is likely to be reasonable estimate for the value of $K_{pMg^{2+}}$ which is comparable to the $K_{pCa^{2+}}$ value of (3.8 ± 0.3) x 10^{-6}.

There may be different side reactions in the central sample chamber, depending on the concentration of the $Mg(HCO_3)_2$. When [$Mg(HCO_3)_2$] is in a range from 0 to 0.5 mM, the localized protons reacts with Al surface and form $Al(OH)_3$ which is slightly alkaline that can explain the slight increase in the central sample chamber liquid pH measured at the end of the experiment. On the other hand, when [$Mg(HCO_3)_2$] is at 0.8 mM and higher, it may react with [Al^{3+}] and [AlO_2^-] ions through the following proposed reaction[148] forming a solid and releasing protons:

$$Al^{3+} + Mg^{2+} + AlO_2^- + 2H_2O \rightarrow MgAl_2O_4 + 4H^+ \quad (18)$$

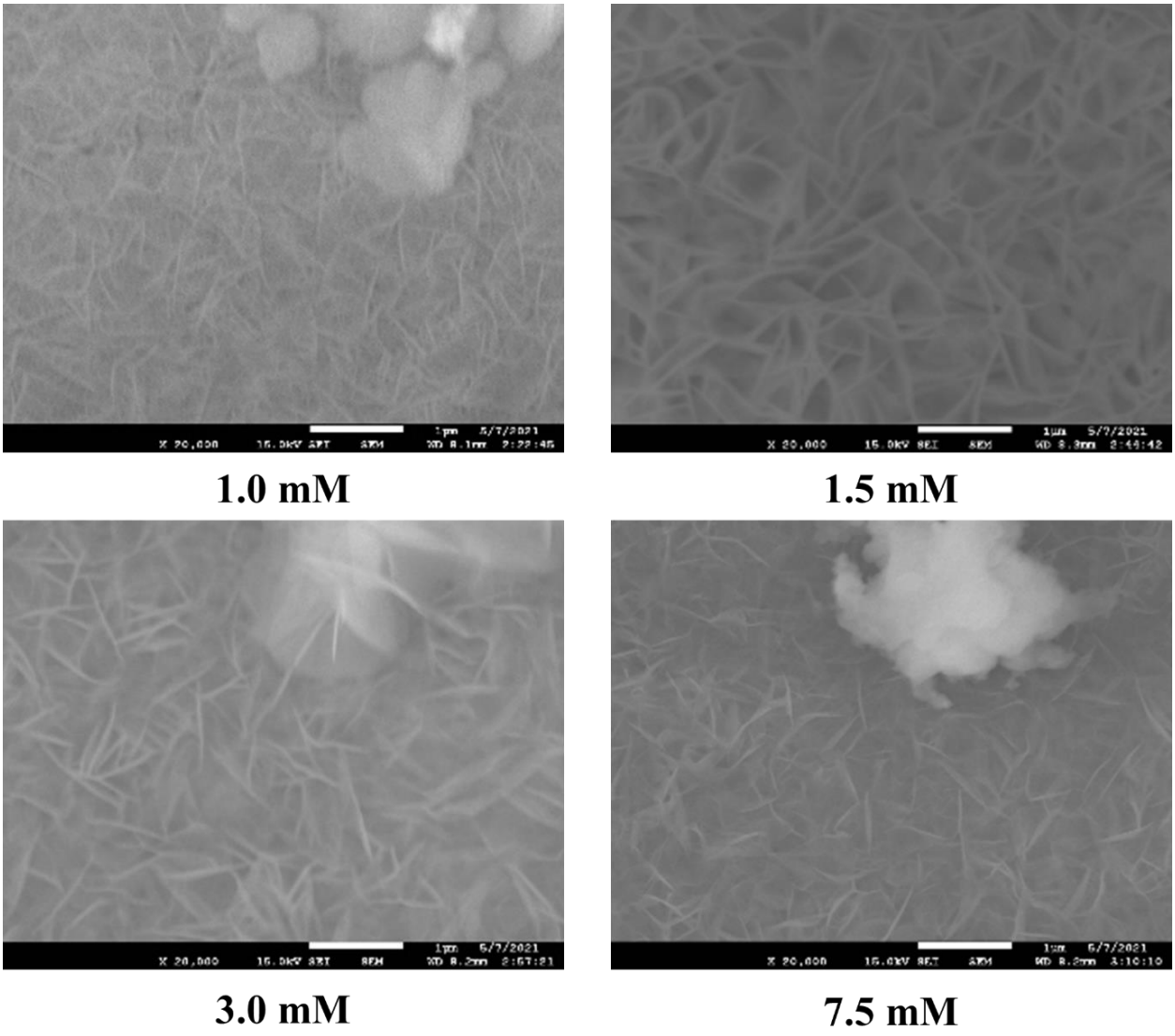

Figure 33. SEM images of the P' membranes taken after 5-hour experiment.

At 20,000 magnification, SEM images of the P' membranes taken after 5-hour experiment with the set up "cathode-water-(Al-Tf-Al)-$Mg(HCO_3)_2$-(Al-Tf-Al)-water-anode" with various concentrations of $Mg(HCO_3)_2$ shows the formation of spinel like structures of $MgAl_2O_4$.

Formation of $MgAl_2O_4$ can be explained by the spinel like structures revealed in the SEM images of the P' membranes (Figure 33).[165, 166] These spinel like structures are most abundantly seen in the membranes used for the experiments with 1.0 mM to 3.0 mM $Mg(HCO_3)_2$. This can explain the experimental observation of precipitated material and dramatic pH drop in the central sample chamber solution with 1.0 mM to 3.0 mM $Mg(HCO_3)_2$.

Consequently, use of this lowered pH value might result in an overestimation of the cation-proton exchange equilibrium constant. For example, the central sample chamber liquid pH of 1.0 mM $Mg(HCO_3)_2$ before the experiment was 8.29 ± 0.01 and after the experiment was 7.95 ± 0.11. If this data is taken as the exchange midpoint, we would have an equilibrium constant of $10^{-(8.29 \pm 0.01)}$ M /0.001 M = (5.1 ± 0.2) x 10^{-6} and $10^{-(7.95 \pm 0.11)}$ M /0.001 M = (1.2 ± 0.4) x 10^{-5} which is substantially smaller than (4.8 ± 2.2) x 10^{-4}, the constant calculated using final pH of 1.25 mM $Mg(HCO_3)_2$ experimental data. This value puts magnesium at an exchange of approximately 230 times greater than sodium and 170 times greater than potassium. Using the final pH at 1.5 mM $Mg(HCO_3)_2$, $K_{pMg^{2+}}$ is calculated as $10^{-(6.02 \pm 0.21)}$ M /0.0015 M = (7.1 ± 4.5) x 10^{-4} which is the largest calculated value. Similarly, using the final pH at 15.0 mM $Mg(HCO_3)_2$, $K_{pMg^{2+}}$ is calculated as $10^{-(8.45 \pm 0.12)}$ M /0.015 M = (2.5 ± 0.9) x 10^{-7} which is the smallest calculated value.

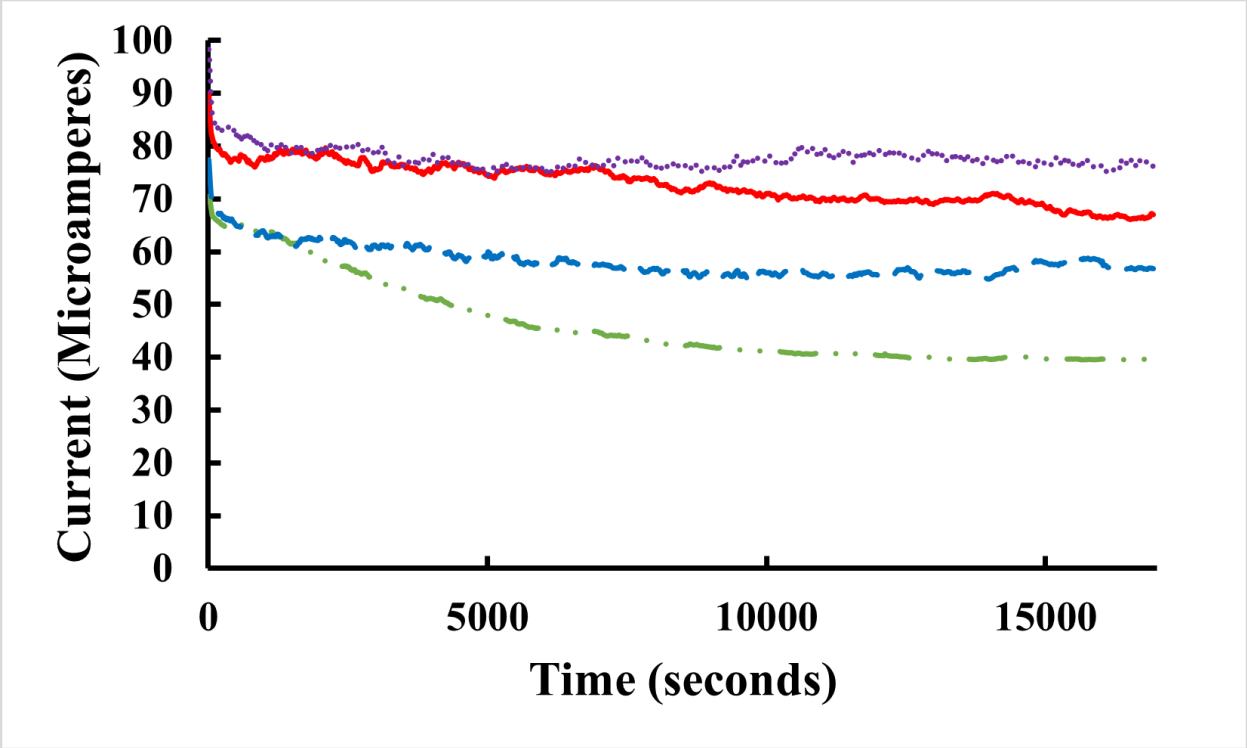

Figure 34. Current versus time data points for the experiments with $Mg(HCO_3)_2$.

Average current of three replicates for 5-hour experiment with the set up "cathode-water-(Al-Tf-Al)-$Mg(HCO_3)_2$-(Al-Tf-Al)-water-anode" and various $Mg(HCO_3)_2$ concentrations. Red solid line represents the experiment run with 0.5 mM $Mg(HCO_3)_2$ in the central sample chamber, blue dashed line represents the experiment run with 1.25 mM $Mg(HCO_3)_2$ in the central sample chamber, purple dotted line represents the experiment run with 15 mM $Mg(HCO_3)_2$ in the central sample chamber, and green dashed (with dots) line represents the experiment run with 0 mM $Mg(HCO_3)_2$ in the central sample chamber.

CONCLUSION

In our study, we conducted experimental demonstrations showing water as a protonic conductor. We observed fast transfer of protonic charge from the anode water chamber to the

cathode water chamber, although the precise mechanism governing this protonic current conduction remains not entirely clear. Our findings offer additional evidence suggesting that excess protons in water exhibit behavior like free electrons in metallic conductors, although with variances in the conduction mechanism. This implies that ultrapure water, despite being an insulator with low electrical conductivity, functions as a proficient protonic conductor. Our experimental results illustrated the rapid conduction of protonic charges within ultrapure water containing excess protons. During the open-circuit electrolysis of deionized water, excess protons are produced in the anode (P) chamber, while excess hydroxide anions are generated in the cathode (N) chamber. These free excess protons in the anode water body do not remain in the bulk liquid phase; instead, they conduct and spread themselves primarily to the liquid-membrane interface in the anode (P) chamber and simultaneously attract the excess hydroxide anions from the cathode water body to the other side of the membrane, forming an "excess anions-membrane-excess protons" capacitor-like system. Due to this phenomenon, the bulk pH in either the anode water body or the cathode water body remains unaffected by the excess protons or the excess hydroxide anions generated during the water electrolysis process. Furthermore, the transmembrane-electrostatically localized protons and their corresponding transmembrane-electrostatically localized hydroxide anions together show a unique behavior referred to as “edge effect” which is caused by the electrostatic repulsion between same charged ions on the flat membrane discs increasing the ion density towards the edge of the membrane.

TELP theory suggests that the localized excess protons are likely to be arranged in a monolayer at the water-membrane interface. This arrangement may allow for the exchange of these excess protons with non-proton cations present in the liquid phase. At 15 mM $Mg(HCO_3)_2$ and 10 mM $Ca(HCO_3)_2$, we see almost complete detectable exchange. These, however, are saturated stock

solution concentrations beyond this point are unattainable with the current parameters. Bicarbonate salts are chosen (instead of chloride salts which are corrosive to Al) [167, 168] because bicarbonate per se does not corrode Al film, which enables the use of Al film as a protonic corrosion sensor. At a nearly complete cation exchange, the minimum localized pH is 4, since this is where aluminum stops detecting protons.[169] All negative controls (0 V) show no corrosion after five hours contact with each solution. This allows us to safely assume all corrosion is from the electrolysis-generated excess protons and excess hydroxide anions. The value of $K_{pCa^{2+}}$ and $K_{pMg^{2+}}$ were calculated to be (3.8 ± 0.3) x 10^{-6} and (5.1 ± 0.2) x 10^{-6} respectively. In conclusion, we can say magnesium and calcium exchanges to a greater degree than sodium and potassium ions with TELP at the P' membrane. Magnesium bicarbonate has properties that make it difficult to study in aqueous solutions at high concentrations. There are several instances of salt formation that needs further investigation.

CHAPTER 5

CONCLUSIONS AND FUTURE DIRECTIONS

In pursuing the overarching objective of comprehensively investigating cation exchange effects in the fields of biochar and bioenergetics, this dissertation has made great progress through three distinct projects. Each project aimed at specific aspects related to cation exchange, contributing to the understanding of biochar properties and the potential applications in solubilizing phosphorus and investigating cation-proton exchange at a liquid-membrane interface. First part of this experimental study was focused on enhancing biochar properties through ozonization. A remarkable improvement in biochar cation exchange capacity (CEC) through was demonstrated. The ozonized biochar exhibited a highest CEC value of 109 ~ 152 cmol/kg, a significant enhancement compared to the untreated biochar. Surface oxygenation, as observed through X-ray photoelectron spectroscopy and elemental analysis, highlighted the formation of oxygen-functional groups, contributing to increased CEC.

Simultaneously, CEC values increased after ozonization, indicates improved cation retention capacity. These alterations have implications for soil fertility and nutrient availability, suggesting a multifaceted impact of ozonization on biochar properties. The decrease in biochar pH and the presence of oxygenated molecular fragments further highlighted the potential agricultural applications of ozonized biochar. This advancement underscores the potential of biochar surface modification for sustainable agricultural practices. Furthermore, this ozone treated biochar did not show any decrease and/or absence of germination of the monocotyl Sorgo (*Sorghum saccharatum*)

and the dicotyl mustard (*Sinapis alba*) plant species after 5 days of exposure. Ozonized biochar along with its filtrate with proper DOC concentrations preliminarily demonstrated to be beneficial during the germination in a laboratory study. Biochar can be made of various biomass which makes it quite complex to study the applications. Depending on the nature of biochar, some of the ozone treated biochar are capable of solubilizing the phosphorus from insoluble phosphate mineral phases in soil. Whereas some of the ozone treated biochar may act as a direct source of phosphorus to the plants when added to soil. Ozonized biochar emerges as a potential agent for solubilizing phosphorus, addressing a critical aspect of nutrient availability in soil. The absence of phytotoxicity further supports its application in sustainable agriculture, highlighting the ecological benefits of this innovative approach. Extensive field studies should be conducted to assess the long-term effects of applying ozonized biochar in diverse soil types and environments. Other quantitative methods should be developed to assess the release of nutrients, particularly phosphorus, from ozonized biochar in soil, with a focus on agricultural applications. Various spectroscopic studies can be conducted for further characterization of biochar and possible chemical reactions.

Experimental demonstrations show water as a protonic conductor, evidenced by a high electrolysis current because of the transfer of protonic charge from the anode to the cathode water chambers. Excess protons in the anode chamber localize to the water-membrane interface, forming an "excess anions-membrane-excess protons" capacitor-like system, without affecting bulk pH in either of the chambers. The transmembrane-electrostatically localized protons (TELP) and transmembrane-electrostatically localized hydroxide anions (TELA) on a membrane disc together exhibit an "edge effect," caused by repulsion between same-charged ions along the flat membrane disc, increasing ion density toward and around the circular edge. The localized excess protons

arrange in a monolayer at the water-membrane interface, enabling exchange with non-proton cations. Further research on the cation exchange in the field of bioenergetics may lead to more interesting findings. The degree of exchange of magnesium and calcium cations with proton is greater than sodium and potassium ions. Exchange equilibrium constants were calculated for these divalent cations. Magnesium bicarbonate has properties that make it difficult to study in aqueous solutions at high concentrations. Significant cation exchange, particularly with magnesium and calcium ions, is observed, with potential implications for further investigation into solution saturation and salt formation. Magnesium oxide and aluminum oxide are potential candidates of salt layers on the aluminum surface after the activities of electrolysis-generated excess protons and excess hydroxide anions.

There are several logical extensions to this research that could be explored in future studies. These areas include mechanistic understanding, conductivity variations, cation exchange dynamics, and salt formation studies. By addressing these areas, further research can deepen our understanding of water as a protonic conductor, elucidate underlying mechanisms, and potentially uncover novel applications in fields such as water treatment, energy storage, and electrochemistry.

REFERENCES

(1) Korb, N.; Jones, C.; Jacobsen, J., Potassium cycling, testing, and fertilizer recommendations. *Nutrient Management Module* **2002,** *5*, 1-12.

(2) Gadsby, D. C., Ion channels versus ion pumps: the principal difference, in principle. *Nat. Rev. Mol. Cell Biol.* **2009,** *10* (5), 344-352.

(3) Chowdhury, S.; Bolan, N.; Farrell, M.; Sarkar, B.; Sarker, J. R.; Kirkham, M. B.; Hossain, M. Z.; Kim, G.-H., Role of cultural and nutrient management practices in carbon sequestration in agricultural soil. *Adv. Agron.* **2021,** *166*, 131-196.

(4) Cotrufo, M. F.; Lavallee, J. M., Soil organic matter formation, persistence, and functioning: A synthesis of current understanding to inform its conservation and regeneration. *Adv. Agron.* **2022,** *172*, 1-66.

(5) Partey, S. T.; Thevathasan, N. V., Agronomic potentials of rarely used agroforestry species for smallholder agriculture in Sub-Saharan Africa: an exploratory study. *Commun. Soil Sci. Plant Anal.* **2013,** *44* (11), 1733-1748.

(6) Jatav, H. S.; Rajput, V. D.; Minkina, T.; Singh, S. K.; Chejara, S.; Gorovtsov, A.; Barakhov, A.; Bauer, T.; Sushkova, S.; Mandzhieva, S., Sustainable approach and safe use of biochar and its possible consequences. *Sustainability* **2021,** *13* (18), 10362.

(7) Venderbosch, R.; Prins, W., Fast pyrolysis technology development. *Biofpr.* **2010,** *4* (2), 178-208.

(8) Bridgwater, A.; Peacocke, G., Fast pyrolysis processes for biomass. *Renewable Sustainable Energy Rev.* **2000,** *4* (1), 1-73.

(9) Uddin, M.; Techato, K.; Taweekun, J.; Rahman, M. M.; Rasul, M.; Mahlia, T.; Ashrafur, S., An overview of recent developments in biomass pyrolysis technologies. *Energies* **2018,** *11* (11), 3115.

(10) Xue, Q.; Xie, S.; Zhang, T., Biochar production and modification for environmental improvement. In *Biochar in Agriculture for Achieving Sustainable Development Goals*, Elsevier, 2022; pp 181-191.

(11) Allohverdi, T.; Mohanty, A. K.; Roy, P.; Misra, M., A review on current status of biochar uses in agriculture. *Molecules* **2021,** *26* (18), 5584.

(12) Yeagle, P. L. *The Structure of Biological Membranes*; CRC Press, 2004.

(13) Magleby, K. L., Ion-channel mechanisms revealed. *Nature* **2017,** *541* (7635), 33-34.

(14) Jacob, N. T., Drug Targets: ligand and voltage gated ion channels. *Int. J Basic Clin. Pharmacol.* **2017,** *6*, 11.

(15) Knollmann, B. C.; Roden, D. M., A genetic framework for improving arrhythmia therapy. *Nature* **2008,** *451* (7181), 929-936.

(16) Mei, T.; Zhang, H.; Xiao, K., Bioinspired Artificial Ion Pumps. *ACS nano* **2022,** *16* (9), 13323-13338.

(17) Dudel, J., Grundlagen der Zellphysiologie. *Physiologie des Menschen* **2000**, 3-19.

(18) Rippy, J. F.; Nelson, P. V., Cation exchange capacity and base saturation variation among Alberta, Canada, moss peats. *HortScience* **2007,** *42* (2), 349-352.

(19) Oni, B. A.; Oziegbe, O.; Olawole, O. O., Significance of biochar application to the environment and economy. *Ann. Agric. Sci.* **2019,** *64* (2), 222-236.

(20) Jaremko, D.; Kalembasa, D., A comparison of methods for the determination of cation exchange capacity of soils/Porównanie metod oznaczania pojemności wymiany kationów i sumy kationów wymiennych w glebach. *Ecol. Chem. Eng. S* **2014,** *21* (3), 487-498.

(21) Maher, M.; Prasad, M.; Raviv, M., Organic soilless media components. *Soilless culture* **2008**, 459-504.

(22) Wijayawardena, M.; Megharaj, M.; Naidu, R., Exposure, toxicity, health impacts, and bioavailability of heavy metal mixtures. *Adv. Agron.* **2016,** *138*, 175-234.

(23) Lee, J. W.; Kidder, M.; Evans, B. R.; Paik, S.; Buchanan Iii, A.; Garten, C. T.; Brown, R. C., Characterization of biochars produced from cornstovers for soil amendment. *Environ. Sci. Tech.* **2010,** *44* (20), 7970-7974.

(24) Huff, M. D.; Lee, J. W., Biochar-surface oxygenation with hydrogen peroxide. *J. Environ. Manage.* **2016,** *165*, 17-21.

(25) Huff, M. D.; Marshall, S.; Saeed, H. A.; Lee, J. W., Surface oxygenation of biochar through ozonization for dramatically enhancing cation exchange capacity. *Bioresources and Bioprocessing* **2018,** *5* (1), 18.

(26) Pari, G.; Darmawan, S.; Prihandoko, B., Porous carbon spheres from hydrothermal carbonization and KOH activation on cassava and tapioca flour raw material. *Procedia Environ. Sci.* **2014,** *20*, 342-351.

(27) Zhang, T.; Walawender, W. P.; Fan, L.; Fan, M.; Daugaard, D.; Brown, R., Preparation of activated carbon from forest and agricultural residues through CO2 activation. *J. Chem. Eng.* **2004,** *105* (1-2), 53-59.

(28) Downie, A.; Crosky, A.; Munroe, P., Physical properties of biochar. In *Biochar for environmental management*, Routledge, 2012; pp 45-64.

(29) Nguyen, M.-V.; Lee, B.-K., A novel removal of CO2 using nitrogen doped biochar beads as a green adsorbent. *Process Saf. Environ. Prot.* **2016,** *104*, 490-498.

(30) González, M.; Cea, M.; Reyes, D.; Romero-Hermoso, L.; Hidalgo, P.; Meier, S.; Benito, N.; Navia, R., Functionalization of biochar derived from lignocellulosic biomass using microwave technology for catalytic application in biodiesel production. *Energy Conv. Manag.* **2017,** *137*, 165-173.

(31) Liu, C.-F.; Sun, R.-C.; Qin, M.-H.; Zhang, A.-P.; Ren, J.-L.; Xu, F.; Ye, J.; Wu, S.-B., Chemical modification of ultrasound-pretreated sugarcane bagasse with maleic anhydride. *Ind. Crops and Prod.* **2007,** *26* (2), 212-219.

(32) Kharel, G.; Sacko, O.; Feng, X.; Morris, J. R.; Phillips, C. L.; Trippe, K.; Kumar, S.; Lee, J. W., Biochar surface oxygenation by ozonization for super high cation exchange capacity. *ACS Sustain. Chem. Eng.* **2019,** *7* (19), 16410-16418.

(33) Anderson, R.; Brye, K. R.; Greenlee, L.; Gbur, E., Chemically precipitated struvite dissolution dynamics over time in various soil textures. *Agric. Sci.* **2020,** *11* (06).

(34) Cordell, D.; Drangert, J.-O.; White, S., The story of phosphorus: global food security and food for thought. *Global Environ. Change* **2009,** *19* (2), 292-305.

(35) Grantham, J., Be persuasive. Be brave. Be arrested (if necessary). *Nature* **2012,** *491* (7424), 303-303.

(36) Plants, N., Approaching peak phosphorus. *Nature Plants* **2022,** *8*, 979.

(37) Penuelas, J.; Coello, F.; Sardans, J., A better use of fertilizers is needed for global food security and environmental sustainability. *Agric. Food Secur.* **2023,** *12* (1), 5.

(38) Kohn, J.; Zimmer, D.; Leinweber, P., Is phosphorus really a scarce resource? Int. *J. Environ. Technol. Manag.* **2018,** *21*, 373-395.

(39) Cordell, D. The Story of Phosphorus: Sustainability implications of global phosphorus scarcity for food security. PhD Dissertation, University of Technology, New South Wales, Australia in collaboration with Linköping University, Linköping, Sweden, 2010. https://opus.lib.uts.edu.au/bitstream/10453/36078/9/02Whole.pdf (accessed 2024-02-08).

(40) Cerven, V.; Novak, J. M.; Szögi, A. A.; Pantuck, K.; Watts, D. W.; Johnson, M. G., The occurrence of legacy P soils and potential mitigation practices using activated biochar. *Agronomy* **2021,** *11* (7), 1289.

(41) Glaser, B.; Lehr, V.-I., Biochar effects on phosphorus availability in agricultural soils: A meta-analysis. *Sci. Rep.* **2019,** *9* (1), 9338.

(42) Khan, F.; Siddique, A. B.; Shabala, S.; Zhou, M.; Zhao, C., Phosphorus plays key roles in regulating plants' physiological responses to abiotic stresses. *Plants* **2023,** *12* (15), 2861.

(43) Patel, M. R.; Panwar, N. L., Biochar from agricultural crop residues: Environmental, production, and life cycle assessment overview. *RCR Advances* **2023**, 200173.

(44) Ajeng, A. A.; Abdullah, R.; Ling, T. C.; Ismail, S.; Lau, B. F.; Ong, H. C.; Chew, K. W.; Show, P. L.; Chang, J.-S., Bioformulation of biochar as a potential inoculant carrier for sustainable agriculture. *Environ. Technol. Innov.* **2020,** *20*, 101168.

(45) Amalina, F.; Abd Razak, A. S.; Krishnan, S.; Sulaiman, H.; Zularisam, A.; Nasrullah, M., Biochar production techniques utilizing biomass waste-derived materials and environmental applications: A review. *JHM Advances* **2022**, 100134.

(46) Dai, Y.; Zheng, H.; Jiang, Z.; Xing, B., Combined effects of biochar properties and soil conditions on plant growth: A meta-analysis. *Sci. Total. Environ.* **2020,** *713*, 136635.

(47) Manea, A.; Tabassum, S.; Lambert, M.; Cinantya, A.; Ossola, A.; Leishman, M. R., Biochar, but not soil microbial additives, increase the resilience of urban plant species to low water availability. *Urban Ecosyst.* **2023**, 1-11.

(48) Cooper, J.; Greenberg, I.; Ludwig, B.; Hippich, L.; Fischer, D.; Glaser, B.; Kaiser, M., Effect of biochar and compost on soil properties and organic matter in aggregate size fractions under field conditions. *Agric. Ecosyst. Environ.* **2020,** *295*, 106882.

(49) M. Tahat, M.; M. Alananbeh, K.; A. Othman, Y.; I. Leskovar, D., Soil health and sustainable agriculture. *Sustainability* **2020,** *12* (12), 4859.

(50) Sacko, O.; Whiteman, R.; Kharel, G.; Kumar, S.; Lee, J. W., Sustainable chemistry: solubilization of phosphorus from insoluble phosphate material hydroxyapatite with ozonized biochar. *ACS Sustain. Chem. Eng.* **2020,** *8* (18), 7068-7077.

(51) Boyer, P. D., What makes ATP synthase spin? *Nature* **1999,** *402* (6759), 247-249.

(52) Blackstock, J. C., Principles of Cellular Metabolism. In *Guide to biochemistry*, Butterworth-Heinemann, 2014; pp 112-122.

(53) Thomas, L. W.; Ashcroft, M., Exploring the molecular interface between hypoxia-inducible factor signalling and mitochondria. *Cell. Mol. Life Sci.* **2019,** *76*, 1759-1777.

(54) Unden, G.; Kim, O. B., Bioenergetics theory and components: Energy conservation and growth by anaerobic bacteria. In *Encyclopedia of Biological Chemistry*, 3rd ed.; Elsevier, 2021; pp 15-22.

(55) Yahia, E. M.; García-Solís, P.; Celis, M. E. M., Contribution of fruits and vegetables to human nutrition and health. In *Postharvest physiology and biochemistry of fruits and vegetables*, Elsevier, 2019; pp 19-45.

(56) McKinlay, J. B.; Cook, G. M.; Hards, K., Microbial energy management: A product of three broad tradeoffs. In *Advances in Microbial Physiology*, Vol. 77; Elsevier, 2020; pp 139-185.

(57) Conrard, L.; Tyteca, D., Regulation of membrane calcium transport proteins by the surrounding lipid environment. *Biomol.* **2019,** *9* (10), 513.

(58) Bhattacharyya, S., Mechanism of temperature stress acclimation and the role of transporters in plants. In *Plant Perspectives to Global Climate Changes*, Elsevier, 2022; pp 413-457.

(59) Chen, C.; Saxena, A. K.; Simcoke, W. N.; Garboczi, D. N.; Pedersen, P. L.; Ko, Y. H., Mitochondrial ATP synthase: crystal structure of the catalytic F1 unit in a vanadate-induced transition-like state and implications for mechanism. *J. Biol. Chem.* **2006,** *281* (19), 13777-13783.

(60) Sole, K. C.; Mooiman, M. B.; Hardwick, E., Ion exchange in hydrometallurgical processing: an overview and selected applications. *Sep. Purif. Rev.* **2018,** *47* (2), 159-178.

(61) Fernández, Y.; Maranon, E.; Castrillón, L.; Vázquez, I., Removal of Cd and Zn from inorganic industrial waste leachate by ion exchange. *J. Hazard. Mater.* **2005,** *126* (1-3), 169-175.

(62) Barman, M. K.; Bhattarai, A.; Saha, B., Applications of ion exchange resins in environmental remediation. *Vietnam J. Chem.* **2023,** *61* (5), 533-550.

(63) Wheaton, R.; Anderson, R., Industrial applications of ion exchange resins. *J. Chem. Educ.* **1958,** *35* (2), 59.

(64) *Applications of Ion Exchange Materials in Biomedical Industries*, Inamuddin Ed.; Springer, 2019. DOI: 10.1007/978-3-030-06082-4

(65) *Applications of ion exchange materials in chemical and food industries*, Inamuddin; Rangreez, T. A.; Asiri, A. M., Eds.; Springer, 2019. DOI: 10.1007/978-3-030-06085-5

(66) Wieckowski, A. *Electrochemical processes in biological systems*; Wiley Online Library: 2015.

(67) Tasaki, I.; Hallett, M., Bioenergetics of nerve excitation. *J. Bioenerg.* **1972,** *3*, 65-79.

(68) Yang, X.; Heinemann, M.; Howard, J.; Huber, G.; Iyer-Biswas, S.; Le Treut, G.; Lynch, M.; Montooth, K. L.; Needleman, D. J.; Pigolotti, S., Physical bioenergetics: Energy fluxes, budgets, and constraints in cells. *Proc. Natl. Acad. Sci.* **2021,** *118* (26), e2026786118.

(69) Lee, J. W., TELP theory: Elucidating the major observations of Rieger et al. 2021 in mitochondria. *Mitochondr. Commun.* **2023,** *1*, 62-72.

(70) Lee, J. W., Mitochondrial energetics with transmembrane electrostatically localized protons: do we have a thermotrophic feature? *Sci. Rep.* **2021,** *11* (1), 14575.

(71) Lee, J. W., Protonic Capacitor: Elucidating the biological significance of mitochondrial cristae formation. *Sci. Rep.* **2020,** *10* (1), 10304.

(72) Lee, J. W., Electrostatically localized proton bioenergetics: better understanding membrane potential. *Heliyon* **2019,** *5* (7).

(73) Biederman, L. A.; Harpole, W. S., Biochar and its effects on plant productivity and nutrient cycling: a meta-analysis. *Gcb Bioenergy* **2013,** *5* (2), 202-214.

(74) Jeffery, S.; Verheijen, F. G. A.; van der Velde, M.; Bastos, A. C., A quantitative review of the effects of biochar application to soils on crop productivity using meta-analysis. *Agric. Ecosyst. Environ.* **2011,** *144* (1), 175-187.

(75) Spokas, K. A.; Cantrell, K. B.; Novak, J. M.; Archer, D. W.; Ippolito, J. A.; Collins, H. P.; Boateng, A. A.; Lima, I. M.; Lamb, M. C.; McAloon, A. J.; Lentz, R. D.; Nichols, K. A., Biochar: A Synthesis of Its Agronomic Impact beyond Carbon Sequestration. *J Environ. Qual.* **2012,** *41* (4), 973-989.

(76) Glaser, B.; Lehmann, J.; Zech, W., Ameliorating physical and chemical properties of highly weathered soils in the tropics with charcoal: A review. *Biol. Fertil. Soils* **2002,** *35* (4), 219-230.

(77) Liang, B.; Lehmann, J.; Solomon, D.; Kinyangi, J.; Grossman, J.; O'Neill, B.; Skjemstad, J. O.; Thies, J.; Luizão, F. J.; Petersen, J.; Neves, E. G., Black Carbon Increases Cation Exchange Capacity in Soils. *Soil Sci. Soc. Am. J.* **2006,** *70* (5), 1719-1730.

(78) Xu, R.-k.; Zhao, A.-z.; Yuan, J.-h.; Jiang, J., pH buffering capacity of acid soils from tropical and subtropical regions of China as influenced by incorporation of crop straw biochars. *J. Soils Sediments* **2012,** *12*, 494-502.

(79) Laird, D. A.; Fleming, P.; Davis, D. D.; Horton, R.; Wang, B.; Karlen, D. L., Impact of biochar amendments on the quality of a typical Midwestern agricultural soil. *Geoderma* **2010,** *158* (3-4), 443-449.

(80) Ramos, F. T.; Dores, E. F. d. C.; Weber, O. L. d. S.; Beber, D. C.; Campelo Jr, J. H.; Maia, J. C. d. S., Soil organic matter doubles the cation exchange capacity of tropical soil under no-till farming in Brazil. *J. Sci. Food Agric.* **2018,** *98* (9), 3595-3602.

(81) Pignatello, J. J., Uchimiya, M., Abiven, S., Schmidt, M.W.I., , Evolution of biochar properties in soil. In *Biochar for Environmental Management: Science, Technology and Implementation*; Lehmann, J., Joseph, S., Eds.; Routledge: Sterling, VA, 2015; pp 195– 233.

(82) Kavitha, B.; Reddy, P. V. L.; Kim, B.; Lee, S. S.; Pandey, S. K.; Kim, K. H., Benefits and limitations of biochar amendment in agricultural soils: A review. *J. Environ. Manag.* **2018,** *227*, 146-154.

(83) Katterer, T.; Roobroeck, D.; Andren, O.; Kimutai, G.; Karltun, E.; Kirchmann, H.; Nyberg, G.; Vanlauwe, B.; de Nowina, K. R., Biochar addition persistently increased soil fertility

and yields in maize-soybean rotations over 10 years in sub-humid regions of Kenya. *Field Crop Res.* **2019,** *235*, 18-26.

(84) El-Naggar, A.; Lee, S. S.; Rinklebe, J.; Farooq, M.; Song, H.; Sarmah, A. K.; Zimmerman, A. R.; Ahmad, M.; Shaheen, S. M.; Ok, Y. S., Biochar application to low fertility soils: A review of current status, and future prospects. *Geoderma* **2019,** *337*, 536-554.

(85) Hailegnaw, N. S.; Mercl, F.; Pracke, K.; Szakova, J.; Tlustos, P., Mutual relationships of biochar and soil pH, CEC, and exchangeable base cations in a model laboratory experiment. *J. Soils Sediments* **2019,** *19* (5), 2405-2416.

(86) Igaz, D.; Simansky, V.; Horak, J.; Kondrlova, E.; Domanova, J.; Rodny, M.; Buchkina, N. P., Can a single dose of biochar affect selected soil physical and chemical characteristics? *Vodohospod. Cas.* **2018,** *66* (4), 421-428.

(87) Mensah, A. K.; Frimpong, K. A., Biochar and/or Compost Applications Improve Soil Properties, Growth, and Yield of Maize Grown in Acidic Rainforest and Coastal Savannah Soils in Ghana. *Int. J. Agron.* **2018**.

(88) Ding, Y.; Liu, Y. G.; Liu, S. B.; Huang, X. X.; Li, Z. W.; Tan, X. F.; Zeng, G. M.; Zhou, L., Potential Benefits of Biochar in Agricultural Soils: A Review. *Pedosphere* **2017,** *27* (4), 645-661.

(89) Lee, J. W.; Hawkins, B.; Kidder, M. K.; Evans, B. R.; Buchanan, A. C.; Day, D., Characterization of biochars produced from peanut hulls and pine wood with different pyrolysis conditions. *Bioresour. Bioprocess.* **2016,** *3* (1), 15.

(90) Lee, J. W.; Hawkins, B.; Day, D. M.; Reicosky, D. C., Sustainability: the capacity of smokeless biomass pyrolysis for energy production, global carbon capture and sequestration. *Energy Environ. Sci.* **2010,** *3* (11), 1695-1705.

(91) Liu, X.; Mao, P. N.; Li, L. H.; Ma, J., Impact of biochar application on yield-scaled greenhouse gas intensity: A meta-analysis. *Sci. Total Environ.* **2019,** *656*, 969-976.

(92) Aller, D. M.; Archontoulis, S. V.; Zhang, W. D.; Sawadgo, W.; Laird, D. A.; Moore, K., Long term biochar effects on corn yield, soil quality and profitability in the US Midwest. *Field Crop Res.* **2018,** *227*, 30-40.

(93) Spokas, K. A., Review of the stability of biochar in soils: predictability of O: C molar ratios. *Carbon Manage.* **2010,** *1* (2), 289-303.

(94) Lee, J. W., *Ozonized biochar compositions and methods of making and using the same.* United States Patent No. US 10,971,335 B2 (2018).

(95) Munera-Echeverri, J. L.; Martinsen, V.; Strand, L. T.; Zivanovic, V.; Cornelissen, G.; Mulder, J., Cation exchange capacity of biochar: An urgent method modification. *Sci. Total Environ.* **2018,** *642*, 190-197.

(96) Tarnawski, M.; Baran, A., Use of chemical indicators and bioassays in bottom sediment ecological risk assessment. *Arch. Environ. Contam. Toxicol.* **2018,** *74*, 395-407.

(97) Valdes, H.; Sanchez-Polo, M.; Rivera-Utrilla, J.; Zaror, C. A., Effect of ozone treatment on surface properties of activated carbon. *Langmuir* **2002,** *18* (6), 2111-2116.

(98) Huff, M. D.; Kumar, S.; Lee, J. W., Comparative analysis of pinewood, peanut shell, and bamboo biomass derived biochars produced via hydrothermal conversion and pyrolysis. *J. Environ. Manag.* **2014,** *146*, 303-308.

(99) Lee, J. W.; Kidder, M.; Evans, B. R.; Paik, S.; Buchanan Iii, A. C.; Garten, C. T.; Brown, R. C., Characterization of Biochars Produced from Cornstovers for Soil Amendment. *Environ. Sci. Technol.* **2010,** *44* (20), 7970-7974.

(100) Lee, J. W., Ozonized biochar: phosphorus sustainability and sand soilization. *Patent Application pending* (**2019**).

(101) Suliman, W.; Harsh, J. B.; Abu-Lail, N. I.; Fortuna, A. M.; Dallmeyer, I.; Garcia-Perez, M., Modification of biochar surface by air oxidation: Role of pyrolysis temperature. *Biomass Bioenerg.* **2016,** *85*, 1-11.

(102) Smith, M.; Ha, S.; Amonette, J. E.; Dallmeyer, I.; Garcia-Perez, M., Enhancing cation exchange capacity of chars through ozonation. *Biomass Bioenerg.* **2015,** *81*, 304-314.

(103) Kyziol, J.; Twardowska, I.; Schmitt-Kopplin, P., The role of humic substances in chromium sorption onto natural organic matter (peat). *Chemosphere* **2006,** *63* (11), 1974-1982.

(104) Harada, Y.; Inoko, A., Cation-exchange properties of soil organic matter: I. Effects of conditions for the measurement on cation-exchange capacity values of humic acid preparations. *Soil Sci. Plant Nutr.* **1975,** *21* (4), 361-369.

(105) Kelessidis, V. C.; Papanicolaou, C.; Foscolos, A., Application of Greek lignite as an additive for controlling rheological and filtration properties of water–bentonite suspensions at high temperatures: A review. *Int. J. Coal Geol.* **2009,** *77* (3-4), 394-400.

(106) Löfgren, S.; Cory, N.; Zetterberg, T.; Larsson, P.-E.; Kronnäs, V., The long-term effects of catchment liming and reduced sulphur deposition on forest soils and runoff chemistry in southwest Sweden. *For. Ecol. Manage.* **2009,** *258* (5), 567-578.

(107) Kelessidis, V. C.; Tsamantaki, C.; Michalakis, A.; Christidis, G. E.; Makri, P.; Papanicolaou, K.; Foscolos, A., Greek lignites as additives for controlling filtration properties of water–bentonite suspensions at high temperatures. *Fuel* **2007,** *86* (7-8), 1112-1121.

(108) Seyedbagheri, M.-M., Influence of humic products on soil health and potato production. *Potato Res.* **2010,** *53* (4), 341-349.

(109) Smil, V. *Feeding the word: a challenge for the 21-st century*; Cambridge: MIT Press, 2000.

(110) Smil, V., Phosphorus in the environment: natural flows and human interferences. *Annu. Rev.Energy Env.* **2000,** *25* (1), 53-88.

(111) Alewell, C.; Ringeval, B.; Ballabio, C.; Robinson, D. A.; Panagos, P.; Borrelli, P., Global phosphorus shortage will be aggravated by soil erosion. *Nat. Commun.* **2020,** *11* (1), 4546.

(112) Herrera-Estrella, L.; López-Arredondo, D., Phosphorus: the underrated element for feeding the world. *Trends Plant Sci.* **2016,** *21* (6), 461-463.

(113) Brownlie, W. J.; Sutton, M. A.; Reay, D. S.; Heal, K. V.; Hermann, L.; Kabbe, C.; Spears, B. M., Global actions for a sustainable phosphorus future. *Nat. Food* **2021,** *2* (2), 71-74.

(114) Rosmarin, A., The precarious geopolitics of phosphorous. *Down to earth* **2004,** *30* (June), 27-34.

(115) Jasinski, S.M. *Phosphate rock statistics and information*. US Geological Survey: 2006.

(116) Steen, I., Phosphorus availability in the 21st century: management of a non-renewable resource. *Phosphorus Potassium* **1998,** *217*, 25-31.

(117) Jasinski, S. M. *Mineral commodity summaries: phosphate rock*. US Geological Survey: 2021.

(118) Mogollón, J. M.; Bouwman, A. F.; Beusen, A. H.; Lassaletta, L.; van Grinsven, H. J.; Westhoek, H., More efficient phosphorus use can avoid cropland expansion. *Nat. Food* **2021,** *2* (7), 509-518.

(119) Hamilton, H. A.; Ivanova, D.; Stadler, K.; Merciai, S.; Schmidt, J.; Van Zelm, R.; Moran, D.; Wood, R., Trade and the role of non-food commodities for global eutrophication. *Nat. Sustain.* **2018,** *1* (6), 314-321.

(120) Lehmann, J.; Cravo, M. d. S.; Vasconselos de Macêdo, J. L.; Moreira, A.; Schroth, G., Phosphorus management for perennial crops in central Amazonian upland soils. *Plant Soil* **2001,** *237*, 309-319.

(121) Brownlie, W. J.; Sutton, M. A.; Cordell, D.; Reay, D. S.; Heal, K. V.; Withers, P. J.; Vanderbeck, I.; Spears, B. M., Phosphorus price spikes: A wake-up call for phosphorus resilience. *Front. Sustain. Food Syst.* **2023,** *7*, 1088776.

(122) *Our Phosphorus Future: Towards Global Phosphorus Sustainability*, Johnes, P. J.; Heathwaite, L.; Spears, B.; Brownlie, W.; Elser, J. J.; Haygarth, P. M.; Macintosh, K.; Withers, P., Eds.; UK Centre for Ecology and Hydrology, Edinburgh, 2022. https://doi.org/10.13140/RG.2.2.14950.50246

(123) Purakayastha, T.; Bera, T.; Bhaduri, D.; Sarkar, B.; Mandal, S.; Wade, P.; Kumari, S.; Biswas, S.; Menon, M.; Pathak, H., A review on biochar modulated soil condition improvements and nutrient dynamics concerning crop yields: Pathways to climate change mitigation and global food security. *Chemosphere* **2019,** *227*, 345-365.

(124) Alotaibi, K. D.; Arcand, M.; Ziadi, N., Effect of biochar addition on legacy phosphorus availability in long-term cultivated arid soil. *Chem. Biol. Technol. Agric.* **2021,** *8*, 1-11.

(125) Blanco-Canqui, H., Biochar and soil physical properties. *Soil Sci. Soc. Am. J.* **2017,** *81* (4), 687-711.

(126) Jien, S.-H.; Wang, C.-S., Effects of biochar on soil properties and erosion potential in a highly weathered soil. *Catena* **2013,** *110*, 225-233.

(127) Zhang, Y.; Wang, J.; Feng, Y., The effects of biochar addition on soil physicochemical properties: A review. *Catena* **2021,** *202*, 105284.

(128) Li, H.; Li, Y.; Xu, Y.; Lu, X., Biochar phosphorus fertilizer effects on soil phosphorus availability. *Chemosphere* **2020,** *244*, 125471.

(129) Ng, C. W. W.; Wang, Y. C.; Ni, J. J.; So, P. S., Effects of phosphorus-modified biochar as a soil amendment on the growth and quality of Pseudostellaria heterophylla. *Sci. Rep.* **2022,** *12* (1), 7268.

(130) Zhao, L.; Cao, X.; Zheng, W.; Scott, J. W.; Sharma, B. K.; Chen, X., Copyrolysis of biomass with phosphate fertilizers to improve biochar carbon retention, slow nutrient release, and stabilize heavy metals in soil. *ACS Sustain. Chem. Eng.* **2016,** *4* (3), 1630-1636.

(131) Wang, T.; Camps-Arbestain, M.; Hedley, M.; Bishop, P., Predicting phosphorus bioavailability from high-ash biochars. *Plant Soil* **2012,** *357*, 173-187.

(132) El Sharkawi, H. M.; Tojo, S.; Chosa, T.; Malhat, F. M.; Youssef, A. M., Biochar-ammonium phosphate as an uncoated-slow release fertilizer in sandy soil. *Biomass Bioenergy* **2018,** *117*, 154-160.

(133) Yao, Y.; Gao, B.; Chen, J.; Yang, L., Engineered biochar reclaiming phosphate from aqueous solutions: mechanisms and potential application as a slow-release fertilizer. *Environ. Sci. Technol.* **2013,** *47* (15), 8700-8708.

(134) Gwenzi, W.; Nyambishi, T.; Chaukura, N.; Mapope, N., Synthesis and nutrient release patterns of a biochar-based N–P–K slow-release fertilizer. *Int. J. Environ. Sci. Technol.* **2018,** *15*, 405-414.

(135) Das, S. K.; Ghosh, G. K., Developing biochar-based slow-release NPK fertilizer for controlled nutrient release and its impact on soil health and yield. *Biomass Convers. Biorefin.* **2023,** *13* (14), 13051-13063.

(136) Wang, Y.; Lin, Y.; Chiu, P. C.; Imhoff, P. T.; Guo, M., Phosphorus release behaviors of poultry litter biochar as a soil amendment. *Sci.Total Environ.* **2015,** *512*, 454-463.

(137) Jones, D. L.; Simfukwe, P.; Hill, P. W.; Mills, R. T.; Emmett, B. A., Evaluation of dissolved organic carbon as a soil quality indicator in national monitoring schemes. *PLoS One* **2014,** *9* (3), e90882.

(138) Porcal, P.; Koprivnjak, J.-F.; Molot, L. A.; Dillon, P. J., Humic substances—part 7: the biogeochemistry of dissolved organic carbon and its interactions with climate change. *Environ. Sci. Pollut. Res.* **2009,** *16*, 714-726.

(139) Neset, T. S. S.; Cordell, D., Global phosphorus scarcity: identifying synergies for a sustainable future. *J. Sci. Food Agric.* **2012,** *92* (1), 2-6.

(140) Lee, J. W., Proton-electrostatics hypothesis for localized proton coupling bioenergetics. *Bioenergetics* **2012,** *1* (104), 1-8.

(141) Lee, J., Proton-electrostatic localization: explaining the bioenergetic conundrum in alkalophilic bacteria. *Bioenergetics* **2015,** *4* (121), 1-8.

(142) Saeed, H.; Lee, J., Experimental determination of proton-cation exchange equilibrium constants at water-membrane interface fundamental to bioenergetics. *WATER J. Multidiscip. Res. J.* **2018,** *9*, 116-140.

(143) Lee, J., A possible electrostatic interpretation for proton localization and delocalization in chloroplast bioenergetics system. *Biophys. J.* **2005**, 88(1), 324A-325A.

(144) Lee, J. W., Electrostatically localized proton bioenergetics: better understanding membrane potential. *Heliyon* **2019,** *5* (7), e01961.

(145) Lee, J. W., Physical chemistry of living systems: Isothermal utilization of latent heat by electrostatically localized protons at liquid-membrane interface. *Biophys. J.* **2019,** *116* (3), 317a.

(146) Lee, J. W., New Finding in Oxidative Phosphorylation: Isothermal Utilization of Latent Heat Energy by Electrostatically Localized Protons at Liquid-Membrane Interface. *FASEB J.* **2019,** *33* (S1), 485.12-485.12.

(147) Lee, J. W., Isothermal environmental heat energy utilization by transmembrane electrostatically localized protons at the liquid–membrane interface. *ACS Omega* **2020,** *5* (28), 17385-17395.

(148) Dove, P. M.; Nix, C. J., The influence of the alkaline earth cations, magnesium, calcium, and barium on the dissolution kinetics of quartz. *Geochim. Cosmochim. Ac.* **1997,** *61* (16), 3329-3340.

(149) Takeda, H.; Hattori, M.; Nishizawa, T.; Yamashita, K.; Shah, S. T.; Caffrey, M.; Maturana, A. D.; Ishitani, R.; Nureki, O., Structural basis for ion selectivity revealed by high-resolution crystal structure of Mg2+ channel MgtE. *Nat. Commun.* **2014,** *5* (1), 5374.

(150) Persson, I., Hydrated metal ions in aqueous solution: How regular are their structures? *Pure Appl. Chem.* **2010,** *82* (10), 1901-1917.

(151) Ohtaki, H.; Radnai, T., Structure and dynamics of hydrated ions. *Chem. Rev.* **1993,** *93* (3), 1157-1204.

(152) Johansson, G., Structures of complexes in solution derived from X-ray diffraction measurements. In *Advances in Inorganic Chemistry*, Elsevier, 1992; pp 159-232.

(153) Jalilehvand, F.; Spångberg, D.; Lindqvist-Reis, P.; Hermansson, K.; Persson, I.; Sandström, M., Hydration of the calcium ion. An EXAFS, large-angle X-ray scattering, and molecular dynamics simulation study. *J. Am. Chem. Soc.* **2001,** *123* (3), 431-441.

(154) Shannon, R. D., Revised effective ionic radii and systematic studies of interatomic distances in halides and chalcogenides. *Acta Crystallogr. Sect. A:* **1976,** *32* (5), 751-767.

(155) Conway, B. E., Ionic hydration in chemistry and biophysics. **1981**.

(156) Adapa, S.; Malani, A., Role of hydration energy and co-ions association on monovalent and divalent cations adsorption at mica-aqueous interface. *Sci. Rep.* **2018,** *8* (1), 12198.

(157) Boehm, H.; Schneider, M., Hydroxyl groups on the surface of "Aerosil" amorphous silica and their reactions. *Z. Anorg. Allgem. Chem.* **1959,** *301* (5/6), 326.

(158) DeCoursey, T. E.; Hosler, J., Philosophy of voltage-gated proton channels. *J. R. Soc. Interface* **2014,** *11* (92), 20130799.

(159) DeCoursey, T. E., Voltage-gated proton channels: molecular biology, physiology, and pathophysiology of the HV family. *Physiol. Rev.* **2013,** *93* (2), 599-652.

(160) Cukierman, S., Proton mobilities in water and in different stereoisomers of covalently linked gramicidin A channels. *Biophys. J.* **2000,** *78* (4), 1825-1834.

(161) Eigen, M.; De Maeyer, L., Self-dissociation and protonic charge transport in water and. *Proc. R. Soc. Lond. A.* **1958,** *247* (1251), 505-533.

(162) Pourbaix, M. *Atlas of electrochemical equilibria in aqueous solutions*, 2nd ed.; National Association of Corrosion Engineers, 1974.

(163) Scamans, G.; Birbilis, N.; Buchheit, R., Corrosion of aluminum and its alloys. In *Shreir's Corrosion*, Elsevier, 2010; pp 1974-2010.

(164) Strauss, M.; Hofhaus, G.; Schröder, R. R.; Kühlbrandt, W., Dimer ribbons of ATP synthase shape the inner mitochondrial membrane. *EMBO J.* **2008,** *27* (7), 1154-1160.

(165) Li, H.; Wei, H. Y.; Cui, Y.; Sang, R. L.; Bu, J. L.; Wei, Y. N.; Lin, J.; Zhao, J. H., Synthesis and characterisation of $MgAl_2O_4$ spinel nanopowders via nonhydrolytic sol–gel route. *J. Ceram. Soc. Jpn.* **2017,** *125* (3), 100-104.

(166) Jia, Z.; Graver, B.; Walmsley, J. C.; Yu, Y.; Solberg, J. K.; Nisancioglu, K., Effect of magnesium on segregation of trace element lead and anodic activation in aluminum Alloys. *J. Electrochem. Soc.* **2007,** *155* (1), C1.

(167) Heine, M.; Keir, D.; Pryor, M., The specific effects of chloride and sulfate ions on oxide covered aluminum. *J. Electrochem. Soc.* **1965,** *112* (1), 24.

(168) Britton, S. C.; Evans, U. R., CCXXXIII.—The passivity of metals. Part VI. A comparison between the penetrating powers of anions. *J Chem. Soc. (Resumed)* **1930**, 1773-1784.

(169) Sukiman, N. L.; Zhou, X.; Birbilis, N.; Hughes, A. E.; Mol, J. M. C.; Garcia, S. J.; Zhou, X.; Thompson, G. E. Durability and Corrosion of Aluminium and Its Alloys: Overview, Property Space, Techniques and Developments. In *Aluminium Alloys: New Trends in Fabrication and Applications*; Ahmad, Z., Ed.; Intech, 2012; pp 47-98.

APPENDIX A

THE CHARACTERISTICS OF ROGUE BIOCHAR

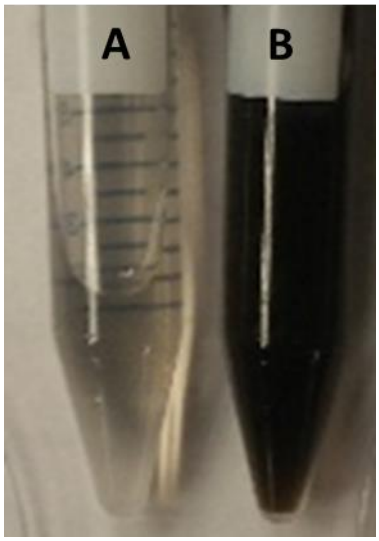

Figure S1: Photograph of the filtrate liquid from the non-ozonized control (A) and the dry-ozonized (B) Rogue biochar samples. A) Showing a portion of the first wash (17 mL/g) from the untreated control biochar; B) Showing a portion of the first wash (17 mL/g) from the dry-ozonized biochar.

Table S1: The characteristics of Rogue Biochar. The Rogue Biochar characteristic data represented in this table are the results from the International Biochar Initiative (IBI) Laboratory Tests for Certification Program (Lab ID. Number: 7020309-01).

Rogue Biochar Properties	**IBI Laboratory Test Result**	**Characterization Method**
Surface Area	456 m^2/g dry	Butane Activity Surface Area Correlation Based on McLaughlin, Shields, Jagiello, & Thiele's 2012 paper: Analytical Options for Biochar Adsorption and Surface Area
Bulk Density	4.9 lb/cu ft (78.5 kg / m^3)	
Organic carbon content	83.6 % of total dry mass	Dry Combust-ASTM D 4373
Hydrogen/Carbon (H:C)	0.25 (0.7 Max)/1 Molar Ratio	H dry combustion/C(above)
Ash content	8.7 % of total dry mass	ASTM D-1762-84
Nitrogen content	0.94 % of total dry mass	Dry Combustion
pH value	10.50	4.11USCC:dil. Rajkovich
Electrical Conductivity (EC20 w/w)	1.212 dS/m	4.10USCC:dil. Rajkovich
Liming (neut. Value as-CaCO3)	11.1 %CaCO3	AOAC 955.01
Carbonates (as-CaCO3)	5.1 %CaCO3	ASTM D 4373
Total (K)	5723 mg/kg	EPA3050B/EPA 6010
Total (P)	725 mg/kg	EPA3050B/EPA 6010
Ammonia (NH4-N)	8.4 mg/kg	Rayment & Higginson
Nitrate (NO3-N)	1.7 mg/kg	Rayment & Higginson
Volatile Matter	25.3 percent dw	ASTM D1762-84

Table S2: Amount of dissolved organic carbon (DOC) material extracted from the non-ozonized control Rogue biochar and the dry-ozonized Rogue biochar. The DOC was measured from the filtrate of the biochar; the DOC was measured from the first wash and the second wash. The DOC measurement of the filtrates was done in duplicate (n=2) and the average ±SD is represented below. For normalized data, the mg of DOC for every gram of biochar was determined by adding the total DOC extracted from the 1st wash and the 2nd wash.

Biochar sample	DOC concentration in mg/L from 1st wash (17mL/g biochar)	DOC concentration in mg/L from 2nd wash (200 mL/g biochar)	DOC from Biochar (mg DOC/g biochar)
Non-ozonized biochar (control)	40.40 (±7.08)	7.12 (±1.02)	2.10 (±0.23)
Dry-ozonized biochar	362.98 (±47.07)	24.66 (±3.07)	10.98 (±1.00)

Table S3: BET surface area of the unground Rogue biochar before and after ozonization. Helium was used as backfill following the evacuation procedure. Values are means ± SD from triplicates (n=3).

Biochar sample	BET surface area (m^2/g) ± SD
Rogue biochar non-ozonized	377.4 (±22.2)
Rogue biochar dry-ozonized	332.1 (±17.8)

Table S4: BET surface area of the ground Pine 400 biochar (non-ozonized) and the ground Rogue biochar (before and after ozonization.) Nitrogen was used as backfill following the evacuation procedure. Values are means ± SD from triplicates (n=3).

Biochar sample	BET surface area (m^2/g) ± SD
Pine 400 non-ozonized biochar	2.05 (±0.42)
Rogue biochar non-ozonized	389.9 (±10.3)
Rogue biochar dry-ozonized	240.5 (±6.1)

Table S5: Angle Resolved Atomic Concentration (in %)

Sample #1: Ozonized Biochar (RBC 90D)

Photoelectron Take Off Angle*	***C***	***O***	***O/C***
80°	78.57	21.43	0.273
70°	78.86	21.14	0.268
50°	79.24	20.76	0.262
30°	79.58	20.42	0.257
10°	79.45	20.55	0.259

****with respect to surface normal.***

Sample #2: Control Biochar (RBC UN)

*Photoelectron Take Off Angle**	*C*	*O*	*O/C*
80°	86.38	13.62	0.158
70°	86.26	13.74	0.159
50°	86.59	13.41	0.155
30°	86.62	13.38	0.154
10°	86.69	13.31	0.154

with respect to surface normal.

Table S6: Angle Resolved XPS Information Depth – O1s

*Photoelectron Take Off Angle**	*Estimated Information Depth/nm*
80°	1.5
70°	2.9
50°	5.5
30°	7.4
10°	8.4

with respect to surface normal.

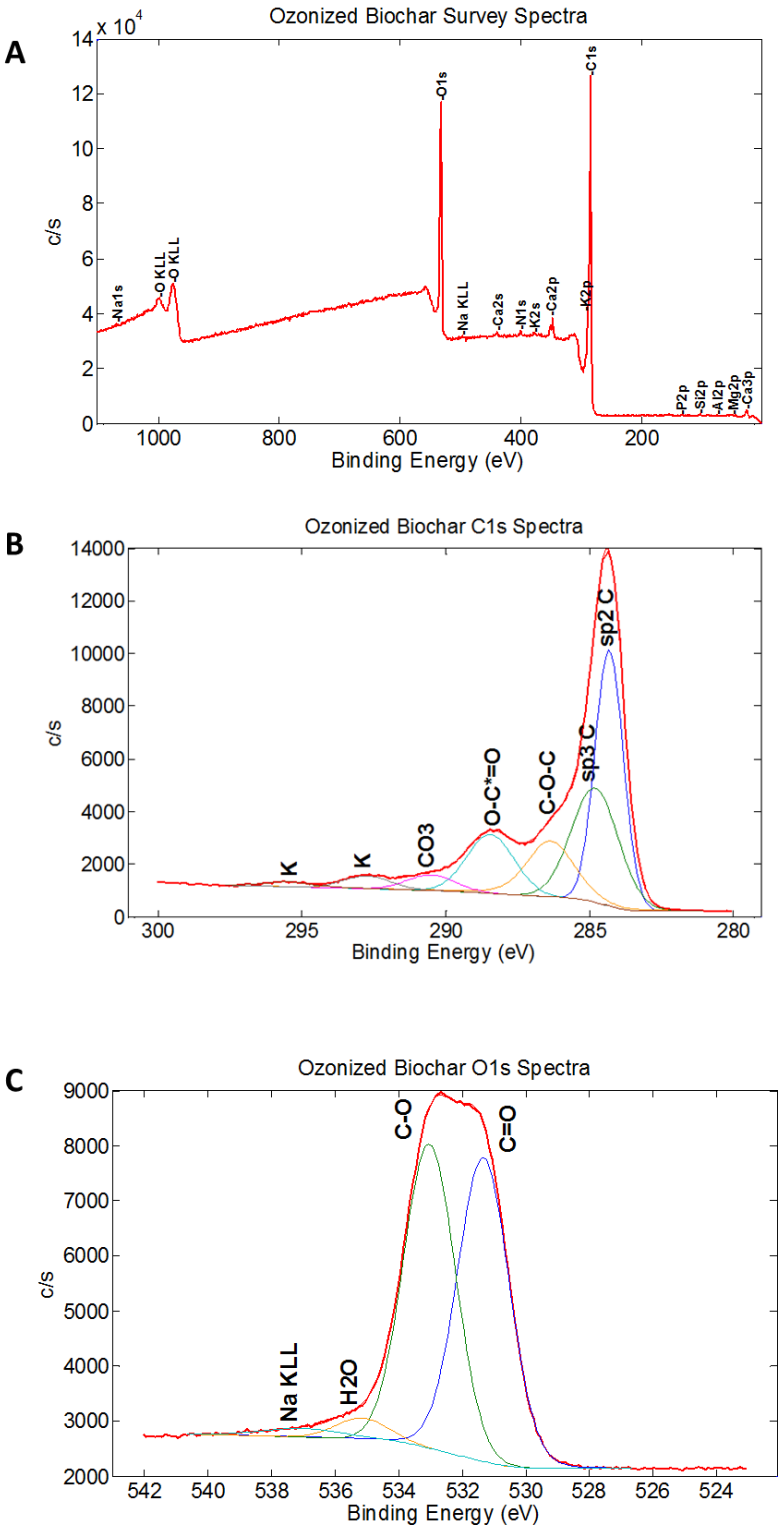

Figure S2: Representation of the survey spectra (A), C1s spectra (B) and O1s spectra (C) from the ozonized biochar sample.

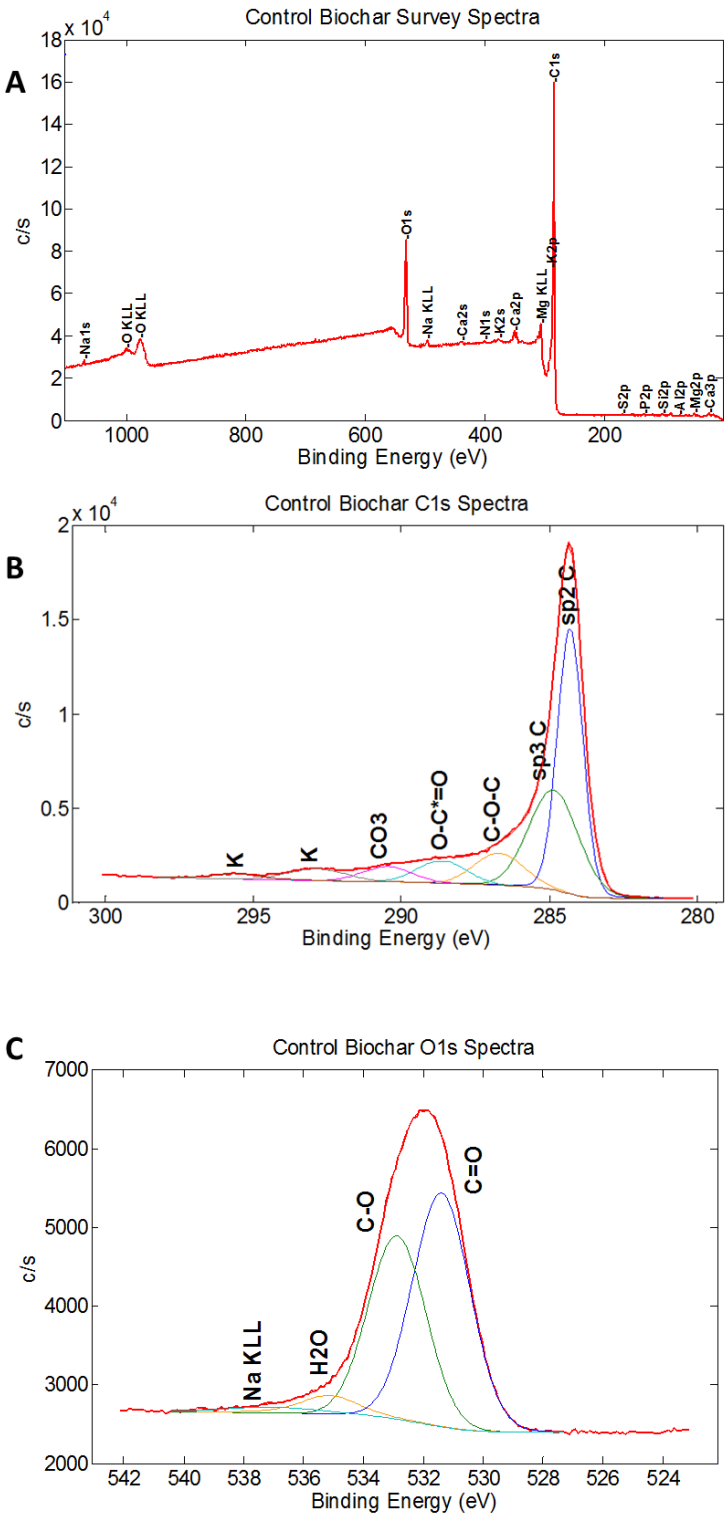

Figure S3: Representation of the survey spectra (A), C1s spectra (B) and O1s spectra (C) from the untreated control biochar sample.

Table S7: SEM-EDS analysis values of the 20 replicates for the Rogue biochar before and after ozonization.

Ozonized Biochar			**Control Biochar**		
C	**O**	**O/C**	**C**	**O**	**O/C**
89.18	10.82	0.121	92.06	7.94	0.086
84.19	15.81	0.188	91.12	8.88	0.097
74.81	25.19	0.337	94.00	6.00	0.064
89.28	10.72	0.120	93.22	6.78	0.073
89.76	10.24	0.114	90.14	9.86	0.109
84.46	15.54	0.184	91.55	8.45	0.092
92.68	7.32	0.079	94.53	5.47	0.058
87.56	12.44	0.142	93.29	6.71	0.072
91.97	8.03	0.087	92.47	7.53	0.081
88.15	11.85	0.134	92.43	7.57	0.082
77.63	22.37	0.288	92.34	7.66	0.083
91.82	8.18	0.089	93.09	6.91	0.074
89.48	10.52	0.118	94.53	5.47	0.058
91.21	8.79	0.096	91.13	8.87	0.097
81.44	18.56	0.228	91.68	8.32	0.091
79.99	20.01	0.250	92.97	7.03	0.076
87.92	12.08	0.137	92.45	7.55	0.082
82.74	17.26	0.209	91.82	8.18	0.089
91.42	8.58	0.094	91.16	8.84	0.097
81.34	18.66	0.229	89.20	10.80	0.121
avg= 86.35 ±5.21	avg= 13.65 ±5.21	avg=0.16 ±0.07	avg=92.26 ±1.36	avg=7.74 ±1.36	avg=0.08 ±0.02

Table S8: Elemental analysis data of carbon and oxygen weight percent of the 6 replicates for the Rogue biochar before and after ozonization.

Ozonized biochar (RBC UN)		Non-ozonized biochar (RBC 90D)	
Oxygen wt %	Carbon wt %	Oxygen wt %	Carbon wt %
20.811	74.833	9.9	85.893
21.363	74.365	9.691	86.94
20.58	74.713	10.182	85.96
17.258	73.148	7.028	74.58
16.845	73.276	6.784	85.252
16.904	72.604	7.002	76.876
avg= 18.96 ±2.16	avg= 73.823 ±0.932	avg=8.4 ±1.6	avg= 82.583 ±5.387

APPENDIX B

BIOCHAR CEC MEASUREMENT PROTOCOL (MODIFIED AMMONIUM ACETATE METHOD) USED AT THE USDA/ARS LABORATORY

1. Pretreatment (adjust to pH 7)

a. Weigh 1 gram of biochar in 50 ml plastic tubes. Record the weight of the tubes with the lids and record the dry matter content of biochar by taking a subsample and drying it at 105 ˚C for 24 hours.

b. Add 20 ml of deionized water and shake horizontally at 200 rpm for 4 hours to ensure proper wetting of the sample. After the wetting step, add 1.5M HCl (or NaOH) gradually until slurry reaches pH 7, keeping track of the volume used. Check pH at intervals over the next 48 hours, and if needed add more HCl or NaOH.

c. After 48 hours, centrifuge the tubes at 1700 g until the supernatant is clear. If, after three hours of centrifuging, the supernatant is still not clear, let the samples stand for two hours on the benchtop to settle. Pipette out the supernatant avoiding the floating biochar particles

d. Add 20ml of deionized water to remove residual acid, and shake horizontally for 1 hour.

e. Centrifuge the tubes at 1700 g until the supernatant is clear. If, after three hours of centrifuging, the supernatant is still not clear, let the samples stand for two hours on the benchtop.

f. Measure EC and then discard the supernatants. Repeat the washings with water (steps c through e) until EC < 200μS/cm.

After step 1d we were unable to centrifuge the biochar out of suspension. Below is the modified procedure used to determine the CEC of the Ozonized and Control biochar samples.

2. Saturation with 1M NH_4OAc
    a. Prepare Whatman Nuclepore Track-Etch membranes (2 μm) and Whatman glass funnel on 250 ml Erlenmeyer flasks.
    b. Add pH-adjusted biochar samples and 20 ml NH_4OAc (pH 7) to the glass funnel. Swirl and let stand for 2 hours.
    c. After 2 hours, turn on the vacuum to remove NH_4OAc.
    d. Repeat 2b/2c so that the sample is washed a total of four times with NH_4OAc. Let the fourth NH_4OAc washing sit overnight before vacuuming out.
3. Remove non-complexed NH_4 with 100% Ethanol
    a. Add 20 ml EtOH to each funnel. Swirl and let stand for 2 hours. If there is biochar on the sides of the funnel, rinse down with a small volume of EtOH.
    b. Repeat 3a for a total of four EtOH washings.
4. Displacement of exchangeable NH_4 with KCl
    a. Attach new Erlenmeyer flasks to each glass funnel.
    b. Add 20 ml 2M KCl to each funnel. Swirl and let stand for 2 hours.
    c. Repeat 4b for a total of four extractions with KCl. Collect all 80 ml of KCl in the same flasks (i.e. extracting volume = 80 ml).
5. Ammonium was measured colorimetrically using citrate and phenylphenol-Nitroprusside and analyzed with spectrophotometer plate reader.

APPENDIX C

PHOSPHORUS SOLUBILIZATION BY OZONIZED BIOCHAR AND ITS DOC FILTRATE

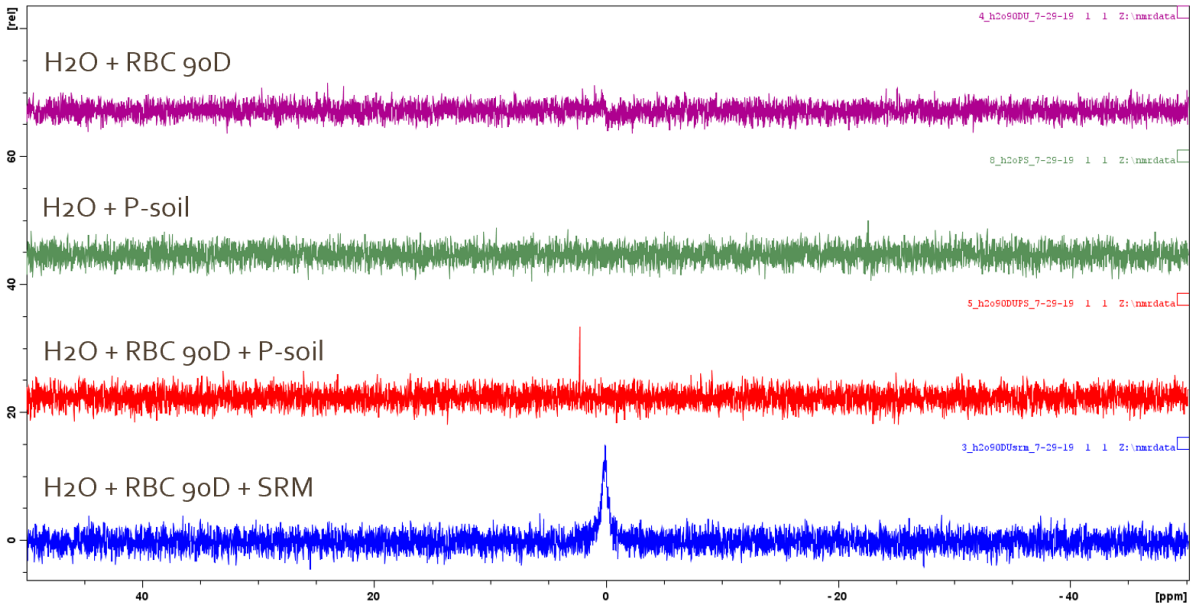

Figure S4. ^{31}P NMR Spectra for Mixture of RBC 90D and P-soil compared with two controls and RBC 90D mixed with SRM 694.

Table S9. pH of the control samples for phosphorus assays at different time intervals

Samples	pH		
	30 mins	**2 days**	**14 days**
Water	6.27±0.04	5.72±0.01	5.93±0.02
P400 UN + water	5.15±0.01	4.89±0.02	5.37±0.01
P400 90D + water	4.11±0.02	4.15±0.01	4.72±0.02
P400 90W + water	3.52±0.04	3.35±0.02	3.58±0.04
P400 90D filtrate	3.82±0.01	3.86±0.01	3.97±0.01
P400 90W filtrate	2.86±0.02	2.88±0.01	3.00±0.01
P400 90W+S filtrate	3.19±0.01	3.28±0.02	4.3±0.01

Table S10. pH of the samples with Portneuf Soil for phosphorus assays at different time intervals

Samples	pH		
	30 mins	**2 days**	**14 days**
Water + P-soil	8.35±0.04	7.89±0.03	7.63±0.01
P400 UN + water + P-soil	7.40±0.04	7.89±0.02	7.22±0.01
P400 90D + water + P-soil	7.13±0.02	7.10±0.06	7.13±0.04
P400 90W + water + P-soil	6.57±0.05	6.62±0.03	6.68±0.01
P400 90D filtrate + P-soil	7.31±0.02	7.57±0.01	7.44±0.01
P400 90W filtrate + P-soil	6.62±0.04	7.24±0.12	7.29±0.03
P400 90W+S filtrate + P-soil	6.82±0.02	7.63±0.02	7.50±0.11

Table S11. pH of the samples with Bennett Soil for phosphorus assays at different time intervals

Samples	pH		
	30 mins	**2 days**	**14 days**
Water + B-soil	8.36±0.01	7.93±0.04	7.76±0.06
P400 UN + water + B-soil	7.34±0.02	7.28±0.03	7.26±0.01
P400 90D + water + B-soil	7.02±0.04	7.16±0.02	7.02±0.03
P400 90W + water + B-soil	6.07±0.08	6.22±0.09	6.41±0.08
P400 90D filtrate + B-soil	7.27±0.01	7.44±0.01	7.35±0.01
P400 90W filtrate + B-soil	6.40±0.01	7.23±0.02	7.23±0.01
P400 90W+S filtrate + B-soil	6.84±0.02	7.52±0.01	7.36±0.08

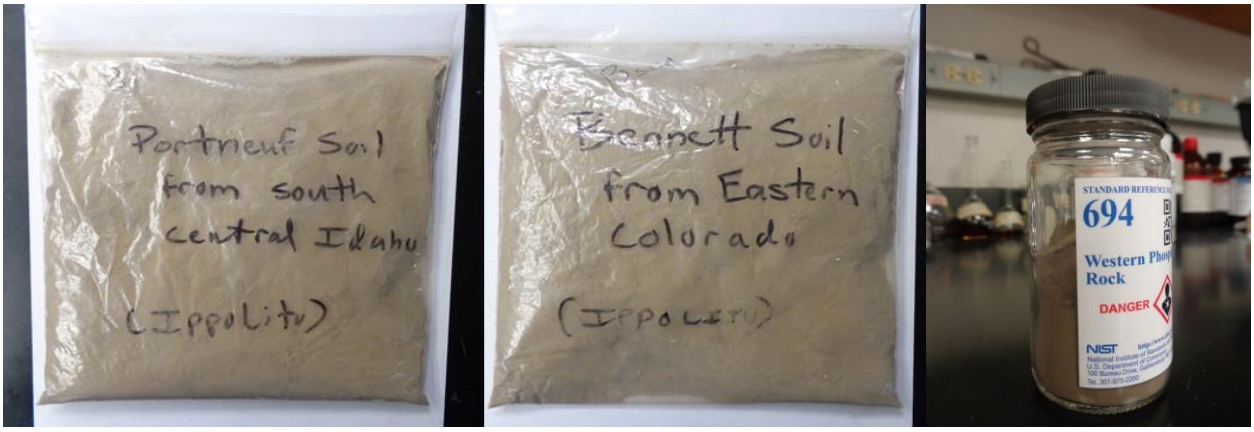

Figure S5. Soils used in phosphorus solubilization (Portneuf Soil from South Central Idaho, Bennett Soil from Eastern Colorado, and Western Phosphate Rock SRM 694 from National Institute of Standard and Technology.

APPENDIX D

PHYTOTOXICITY STUDY OF OZONIZED BIOCHAR AND ITS DOC FILTRATE

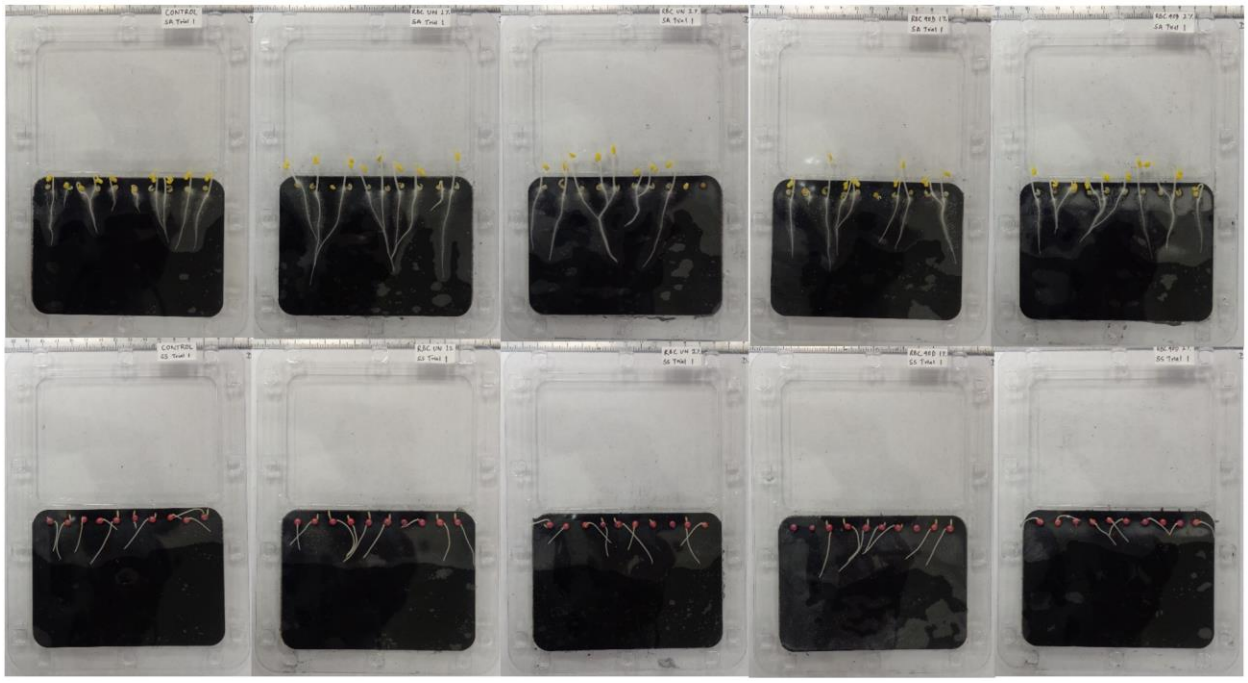

Figure S6. Images of the test plates for phytotoxicity study of ozone treated biochar taken after 3 days of exposure of seeds of monocotyl Sorgo (*Sorghum saccharatum*) and the dicotyl mustard (*Sinapis alba*) to soil mixed with various biochar concentrations.

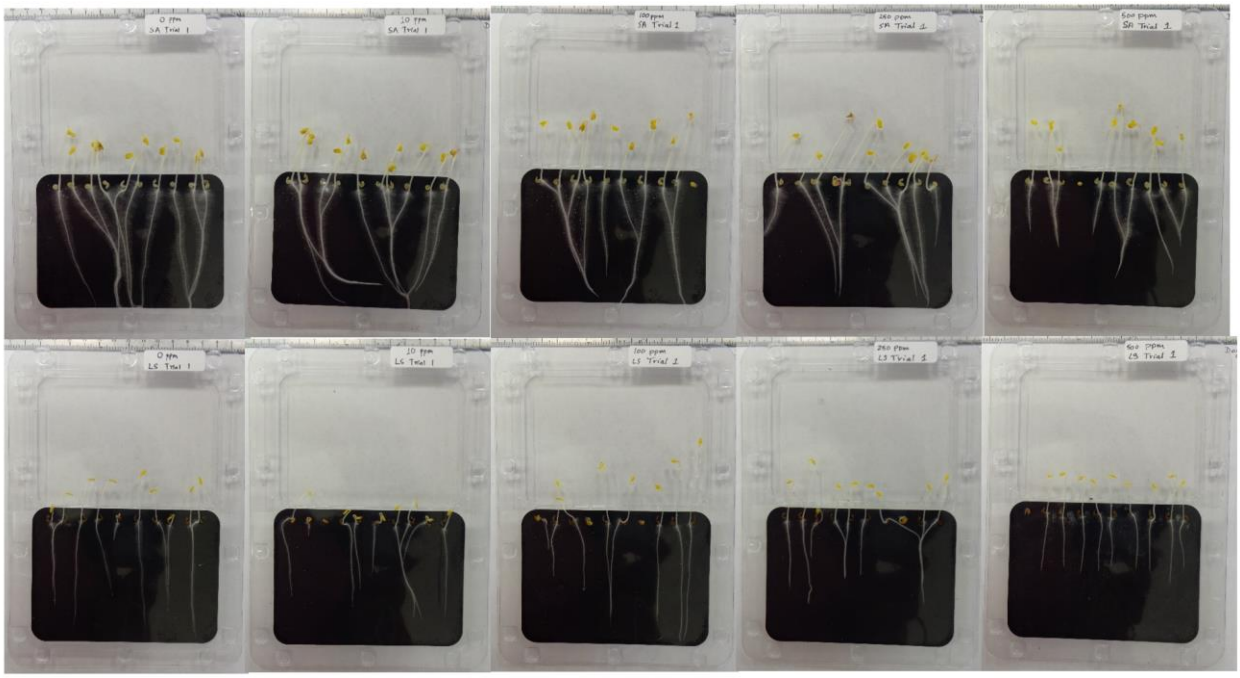

Figure S7. Images of the test plates for phytotoxicity study of various concentration of ozone treated biochar DOC filtrate taken after 3 days of exposure of seeds of the dicotyls garden cress (*Lepidium sativum*) and mustard (*Sinapis alba*).

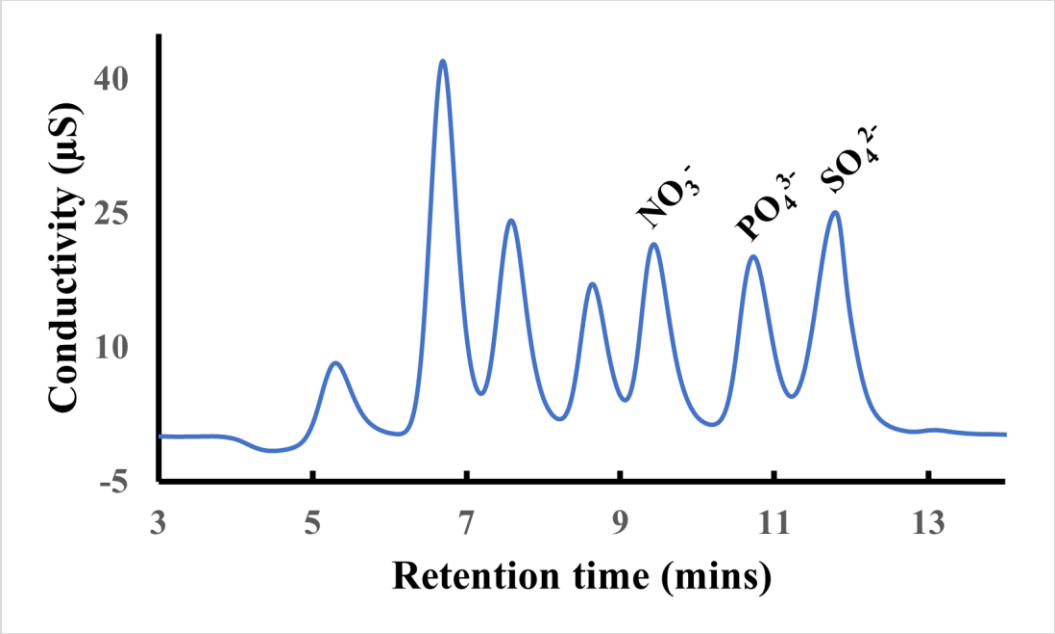

Figure S8. Conductivity signals of anions from Dionex 7 Anion standard used for Ion Chromatography measurements of phosphorus concentration released by ozonized biochar filtrate with various DOC concentrations in soil after 30 minutes of incubation with SRM 694, P-soil, and B-soil.

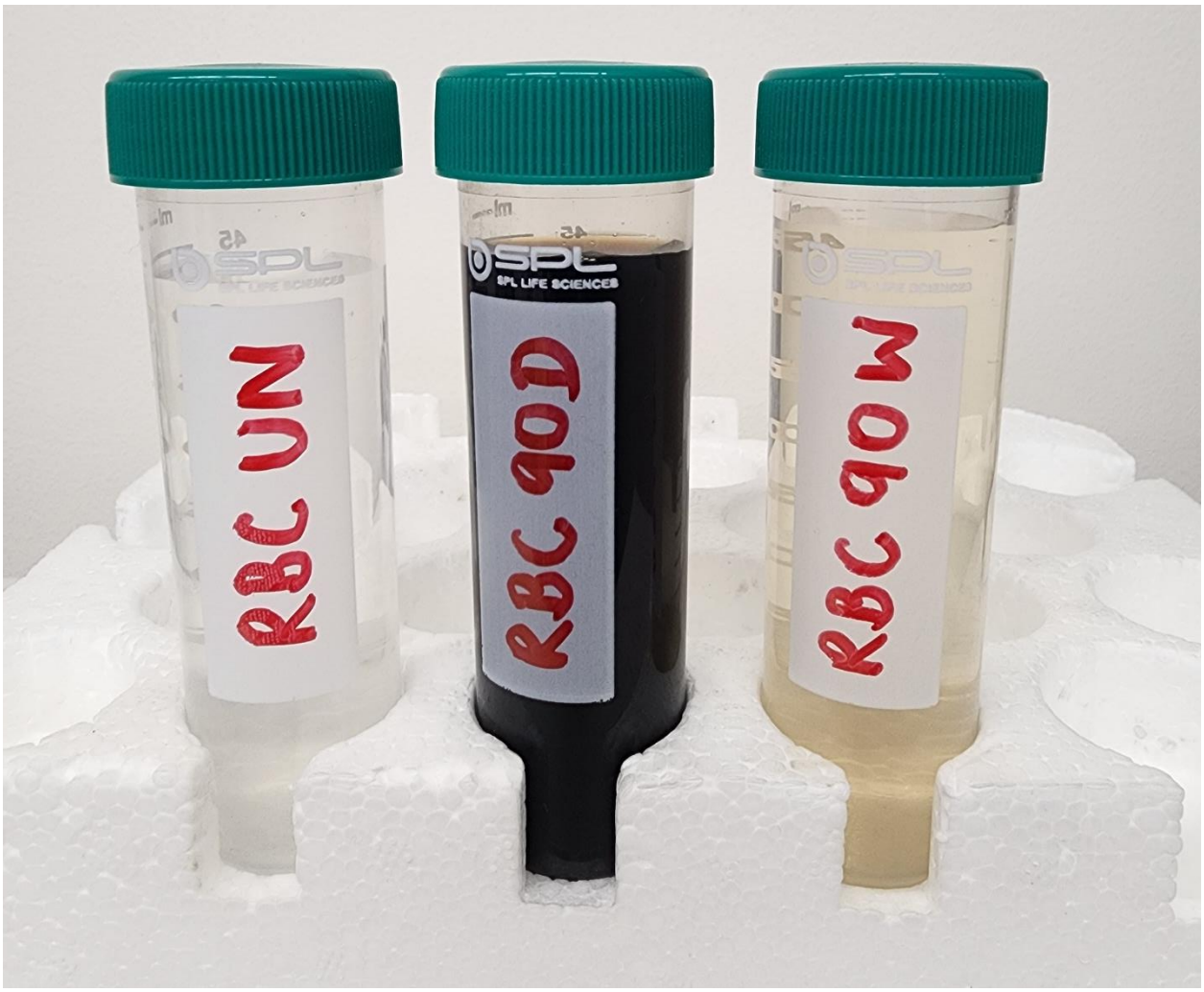

Figure S9: Photograph of the filtrate liquid from the non-ozonized (RBC UN), the dry-ozonized (RBC 90D), and wet-ozonized (RBC 90W) Rogue biochar samples.

Figure S10: Photograph of the filtrate liquid from the non-ozonized (P400 UN), the dry-ozonized (P400 90D), the wet-ozonized (P400 90W), and the wet-ozonized and sonicated (P400 90W+S) Pinewood biochar samples.

APPENDIX E

CALCIUM AND MAGNESIUM CATION-PROTON EXCHANGE

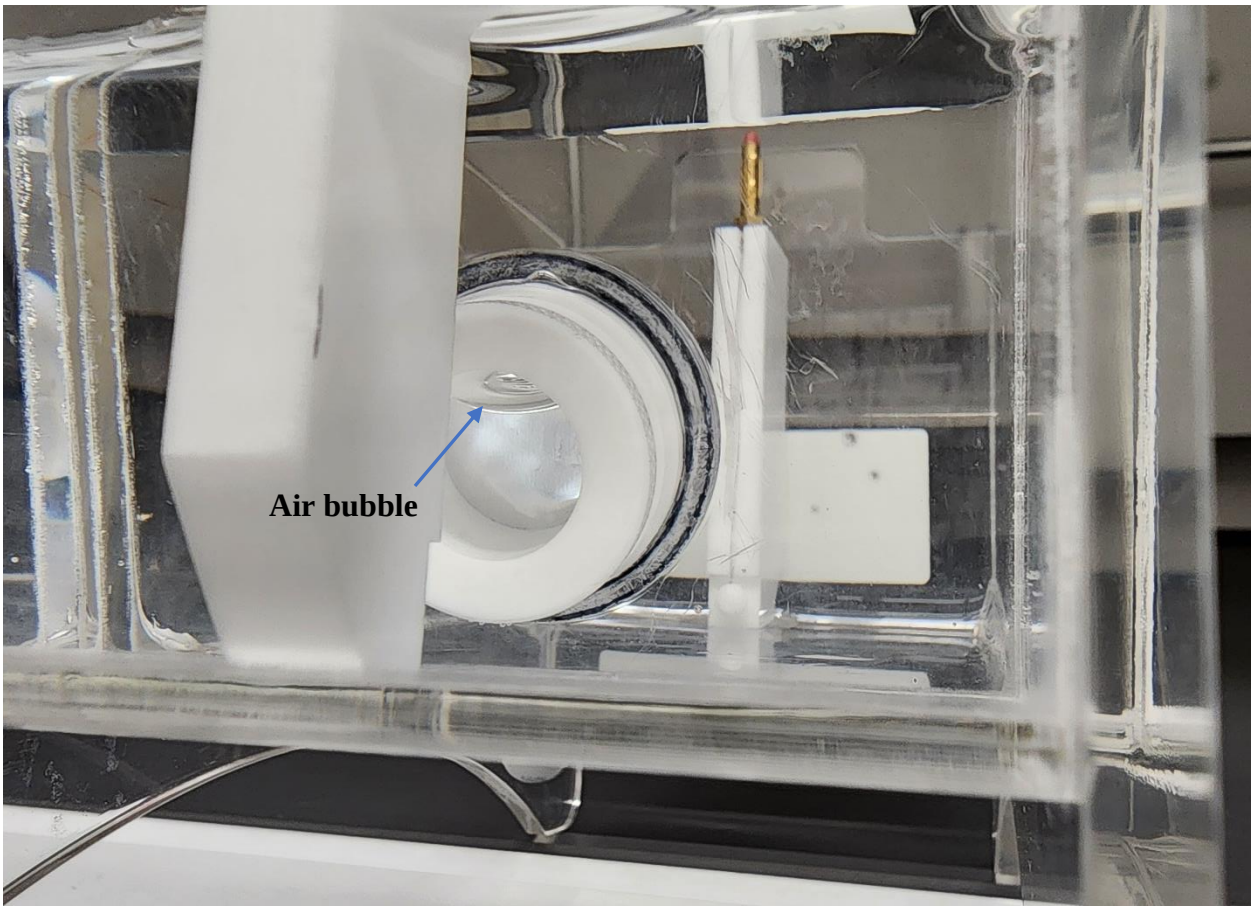

Figure S11: Photograph of the cathode chamber of the electrolysis chamber showing the air bubble formed at N membrane of the Teflon sample chamber during filling the cathode chamber with water.

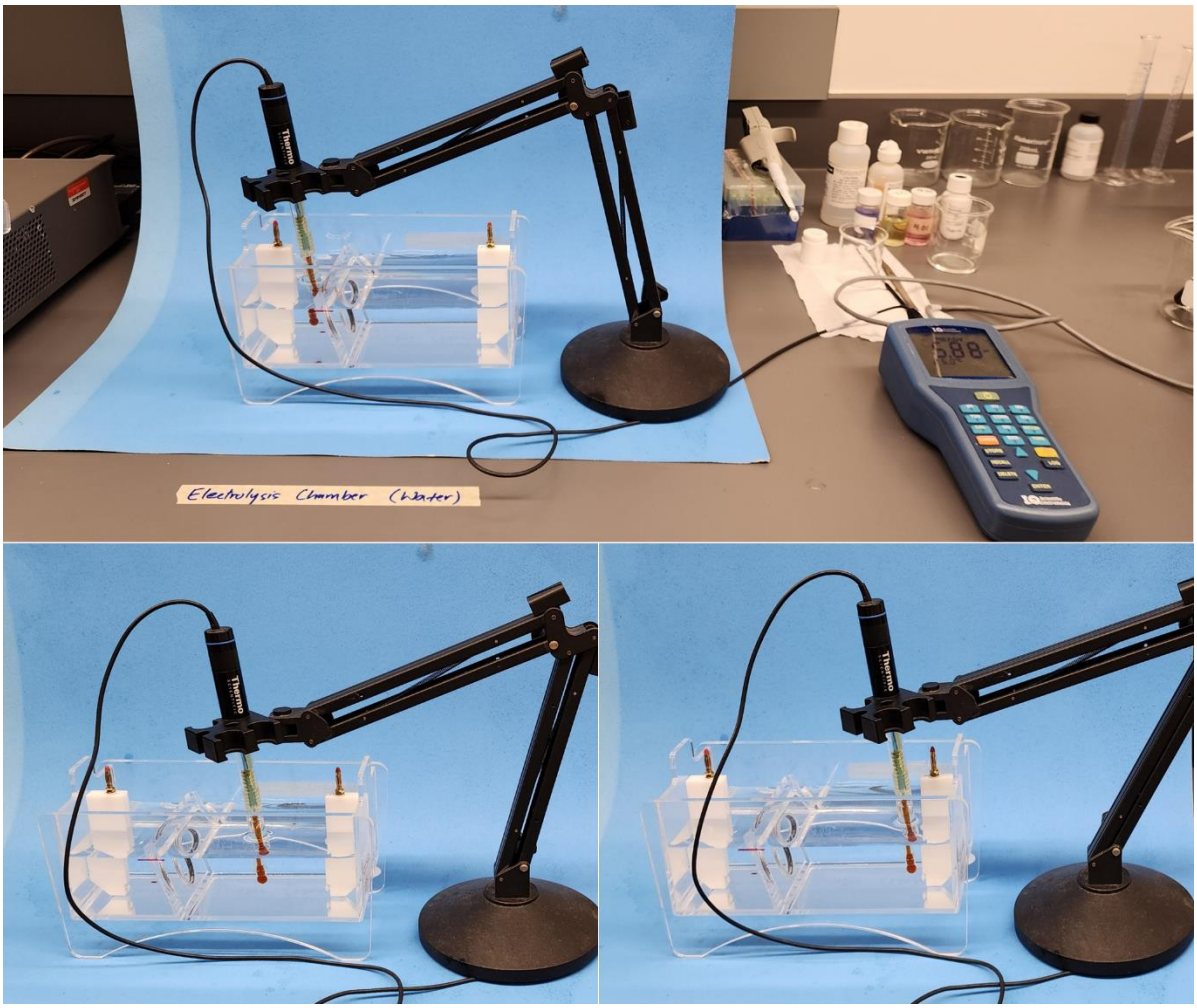

Figure S12: Photographs of the electrolysis chamber taken while measuring the pH in the cathode and anode bulk water phase performed at various distances from the cathode and anode (to demonstrate excess protons do not change the chamber bulk water pH).

Table S12. Raw data for the conductivity measurements of cathode and anode water, pH measurements for cathode, anode and sample chamber, and mass of P' and P aluminum membranes before and after the experiment at 200 V for 2 mM $Ca(HCO_3)_2$ (Trial 1)

	Conductivity of Cathode Water (µS)	**Conductivity of Anode Water (µS)**	**pH of Cathode chamber**	**pH of Anode chamber**	**pH of Sample chamber**	**Mass of P' Aluminum (mg)**	**Mass of P Aluminum (mg)**
Before	1.219	1.219	6.07	6.07	8.09	28.69	28.46
	1.220	1.220	6.06	6.06	8.09	28.70	28.44
	1.221	1.221	6.07	6.07	8.09	28.71	28.45
	1.222	1.222	6.09	6.09	8.10	28.69	28.44
	1.222	1.222	6.10	6.10	8.10	28.69	28.45
	1.223	1.223	6.11	6.11	8.10	28.68	28.46
Average	**1.221**	**1.221**	**6.08**	**6.08**	**8.10**	**28.69**	**28.45**
SD	**0.001**	**0.001**	**0.02**	**0.02**	**0.01**	**0.01**	**0.01**
After	1.259	1.535	6.15	6.01	8.71	28.72	28.42
	1.260	1.536	6.16	6.01	8.69	28.73	28.41
	1.261	1.537	6.18	6.03	8.73	28.73	28.43
	1.262	1.538	6.19	6.05	8.74	28.71	28.43
	1.263	1.539	6.20	6.04	8.75	28.74	28.41
	1.264	1.540	6.21	6.03	8.76	28.73	28.41
Average	**1.262**	**1.538**	**6.18**	**6.03**	**8.73**	**28.73**	**28.42**
SD	**0.002**	**0.002**	**0.02**	**0.02**	**0.03**	**0.01**	**0.01**

Table S13. Raw data for the conductivity measurements of cathode and anode water, pH measurements for cathode, anode and sample chamber, and mass of P' and P aluminum membranes before and after the experiment at 200 V for 2 mM $Ca(HCO_3)_2$ (Trial 2)

	Conductivity of Cathode Water (µS)	Conductivity of Anode Water (µS)	pH of Cathode chamber	pH of Anode chamber	pH of Sample chamber	Mass of P' Aluminum (mg)	Mass of P Aluminum (mg)
Before	1.109	1.109	6.18	6.18	8.15	28.39	28.25
	1.110	1.110	6.15	6.15	8.12	28.39	28.27
	1.111	1.111	6.16	6.16	8.15	28.40	28.27
	1.112	1.112	6.17	6.17	8.15	28.39	28.25
	1.112	1.112	6.18	6.18	8.15	28.40	28.25
	1.113	1.113	6.19	6.19	8.12	28.37	28.27
Average	**1.111**	**1.111**	**6.17**	**6.17**	**8.14**	**28.39**	**28.26**
SD	**0.001**	**0.001**	**0.01**	**0.01**	**0.02**	**0.01**	**0.01**
After	1.254	1.419	6.27	6.01	8.89	28.41	28.26
	1.258	1.420	6.28	6.02	8.91	28.40	28.25
	1.256	1.422	6.29	6.03	8.91	28.41	28.24
	1.259	1.423	6.30	6.04	8.93	28.41	28.24
	1.261	1.424	6.31	6.05	8.95	28.40	28.25
	1.260	1.425	6.32	6.07	8.96	28.41	28.25
Average	**1.258**	**1.422**	**6.30**	**6.04**	**8.93**	**28.41**	**28.25**
SD	**0.003**	**0.002**	**0.02**	**0.02**	**0.03**	**0.01**	**0.01**

Table S14. Raw data for the conductivity measurements of cathode and anode water, pH measurements for cathode, anode and sample chamber, and mass of P' and P aluminum membranes before and after the experiment at 200 V for 2 mM $Ca(HCO_3)_2$ (Trial 3)

	Conductivity of Cathode Water (µS)	Conductivity of Anode Water (µS)	pH of Cathode chamber	pH of Anode chamber	pH of Sample chamber	Mass of P' Aluminum (mg)	Mass of P Aluminum (mg)
Before	1.337	1.337	5.93	5.93	8.12	28.06	28.20
	1.338	1.338	5.94	5.94	8.12	28.08	28.19
	1.339	1.339	5.96	5.96	8.09	28.05	28.21
	1.339	1.339	5.97	5.97	8.09	28.09	28.19
	1.340	1.340	5.98	5.98	8.12	28.06	28.20
	1.341	1.341	5.99	5.99	8.12	28.07	28.19
Average	**1.339**	**1.339**	**5.96**	**5.96**	**8.11**	**28.07**	**28.20**
SD	**0.001**	**0.001**	**0.02**	**0.02**	**0.02**	**0.01**	**0.01**
After	1.405	1.526	6.09	5.88	8.76	28.09	28.22
	1.406	1.527	6.10	5.90	8.77	28.10	28.21
	1.407	1.528	6.11	5.91	8.78	28.09	28.22
	1.407	1.529	6.12	5.91	8.79	28.08	28.20
	1.408	1.530	6.13	5.92	8.81	28.08	28.21
	1.409	1.530	6.14	5.93	8.82	28.09	28.21
Average	**1.407**	**1.528**	**6.12**	**5.91**	**8.79**	**28.09**	**28.21**
SD	**0.001**	**0.002**	**0.02**	**0.02**	**0.02**	**0.01**	**0.01**

Table S15. Raw data for the conductivity measurements of cathode and anode water, pH measurements for cathode, anode and sample chamber, and mass of P' and P aluminum membranes before and after the experiment at 0 V for 2 mM $Ca(HCO_3)_2$

	Conductivity of Cathode Water (µS)	Conductivity of Anode Water (µS)	pH of Cathode chamber	pH of Anode chamber	pH of Sample chamber	Mass of P' Aluminum (mg)	Mass of P Aluminum (mg)
Before	1.219	1.219	6.07	6.07	8.09	26.79	26.66
	1.220	1.220	6.06	6.06	8.09	26.79	26.67
	1.221	1.221	6.07	6.07	8.09	26.78	26.67
	1.222	1.222	6.09	6.09	8.10	26.78	26.65
	1.222	1.222	6.10	6.10	8.10	26.81	26.67
	1.223	1.223	6.11	6.11	8.10	26.80	26.65
Average	**1.221**	**1.221**	**6.08**	**6.08**	**8.10**	**26.79**	**26.66**
SD	**0.001**	**0.001**	**0.02**	**0.02**	**0.01**	**0.01**	**0.01**
After	1.507	1.586	5.95	5.90	8.13	26.82	26.69
	1.508	1.587	5.96	5.91	8.15	26.81	26.70
	1.509	1.588	5.98	5.92	8.16	26.81	26.69
	1.510	1.589	5.98	5.93	8.17	26.82	26.68
	1.512	1.590	5.99	5.94	8.18	26.81	26.71
	1.513	1.591	6.00	5.94	8.19	26.83	26.70
Average	**1.510**	**1.589**	**5.98**	**5.92**	**8.16**	**26.82**	**26.70**
SD	**0.002**	**0.002**	**0.02**	**0.02**	**0.02**	**0.01**	**0.01**

Table S16. Raw data for the conductivity measurements of cathode and anode water, pH measurements for cathode, anode and sample chamber, and mass of P' and P aluminum membranes before and after the experiment at 200 V for 1.25 mM $Mg(HCO_3)_2$ (Trial 1)

	Conductivity of Cathode Water (µS)	Conductivity of Anode Water (µS)	pH of Cathode chamber	pH of Anode chamber	pH of Sample chamber	Mass of P' Aluminum (mg)	Mass of P Aluminum (mg)
Before	1.232	1.232	6.05	6.05	8.25	28.21	28.13
	1.233	1.233	5.97	5.97	8.26	28.20	28.12
	1.234	1.234	5.97	5.97	8.26	28.22	28.12
	1.234	1.234	5.98	5.98	8.25	28.21	28.13
	1.235	1.235	5.98	5.98	8.26	28.22	28.12
	1.236	1.236	5.97	5.97	8.27	28.23	28.13
Average	**1.234**	**1.234**	**5.99**	**5.99**	**8.26**	**28.22**	**28.13**
SD	**0.001**	**0.001**	**0.03**	**0.03**	**0.01**	**0.01**	**0.01**
After	1.118	1.506	6.18	5.86	6.17	28.33	28.16
	1.119	1.507	6.19	5.87	6.18	28.34	28.14
	1.120	1.508	6.19	5.88	6.19	28.35	28.16
	1.121	1.508	6.20	5.88	6.21	28.31	28.15
	1.122	1.509	6.21	5.89	6.22	28.34	28.17
	1.123	1.510	6.21	5.89	6.22	28.32	28.16
Average	**1.121**	**1.508**	**6.20**	**5.88**	**6.20**	**28.33**	**28.16**
SD	**0.002**	**0.001**	**0.01**	**0.01**	**0.02**	**0.01**	**0.01**

Table S17. Raw data for the conductivity measurements of cathode and anode water, pH measurements for cathode, anode and sample chamber, and mass of P' and P aluminum membranes before and after the experiment at 200 V for 1.25 mM $Mg(HCO_3)_2$ (Trial 2)

	Conductivity of Cathode Water (µS)	Conductivity of Anode Water (µS)	pH of Cathode chamber	pH of Anode chamber	pH of Sample chamber	Mass of P' Aluminum (mg)	Mass of P Aluminum (mg)
Before	1.785	1.785	6.13	6.13	8.28	28.39	28.55
	1.785	1.785	6.11	6.11	8.28	28.38	28.55
	1.783	1.783	6.10	6.10	8.29	28.38	28.57
	1.783	1.783	6.10	6.10	8.28	28.37	28.56
	1.784	1.784	6.10	6.10	8.29	28.37	28.57
	1.783	1.783	6.09	6.09	8.28	28.38	28.55
Average	**1.784**	**1.784**	**6.11**	**6.11**	**8.28**	**28.38**	**28.56**
SD	**0.001**	**0.001**	**0.01**	**0.01**	**0.01**	**0.01**	**0.01**
After	1.692	2.13	6.07	5.96	6.42	28.51	28.57
	1.693	2.13	6.06	5.98	6.43	28.52	28.59
	1.691	2.13	6.06	5.99	6.42	28.51	28.56
	1.692	2.13	6.08	5.97	6.45	28.53	28.58
	1.693	2.13	6.09	6.01	6.46	28.51	28.59
	1.694	2.14	6.09	6.02	6.45	28.51	28.57
Average	**1.693**	**2.13**	**6.08**	**5.99**	**6.44**	**28.52**	**28.58**
SD	**0.001**	**0.00**	**0.01**	**0.02**	**0.02**	**0.01**	**0.01**

Table S18. Raw data for the conductivity measurements of cathode and anode water, pH measurements for cathode, anode and sample chamber, and mass of P' and P aluminum membranes before and after the experiment at 200 V for 1.25 mM $Mg(HCO_3)_2$ (Trial 3)

	Conductivity of Cathode Water (µS)	Conductivity of Anode Water (µS)	pH of Cathode chamber	pH of Anode chamber	pH of Sample chamber	Mass of P' Aluminum (mg)	Mass of P Aluminum (mg)
Before	1.338	1.338	6.19	6.19	8.29	28.26	28.33
	1.339	1.339	6.18	6.18	8.32	28.27	28.35
	1.340	1.340	6.17	6.17	8.31	28.26	28.32
	1.340	1.340	6.17	6.17	8.31	28.26	28.35
	1.341	1.341	6.16	6.16	8.32	28.27	28.34
	1.341	1.341	6.16	6.16	8.32	28.25	28.31
Average	**1.340**	**1.340**	**6.17**	**6.17**	**8.31**	**28.26**	**28.33**
SD	**0.001**	**0.001**	**0.01**	**0.01**	**0.01**	**0.01**	**0.02**
After	1.563	1.475	6.14	6.12	6.08	28.35	28.29
	1.564	1.472	6.16	6.13	6.09	28.36	28.30
	1.565	1.471	6.15	6.09	6.10	28.37	28.27
	1.566	1.471	6.16	6.10	6.11	28.36	28.28
	1.566	1.470	6.14	6.11	6.11	28.36	28.29
	1.567	1.470	6.14	6.11	6.12	28.35	28.28
Average	**1.565**	**1.472**	**6.15**	**6.11**	**6.10**	**28.36**	**28.29**
SD	**0.001**	**0.002**	**0.01**	**0.01**	**0.01**	**0.01**	**0.01**

Table S19. Raw data for the conductivity measurements of cathode and anode water, pH measurements for cathode, anode and sample chamber, and mass of P' and P aluminum membranes before and after the experiment at 0 V for 1.25 mM $Mg(HCO_3)_2$

	Conductivity of Cathode Water (µS)	Conductivity of Anode Water (µS)	pH of Cathode chamber	pH of Anode chamber	pH of Sample chamber	Mass of P' Aluminum (mg)	Mass of P Aluminum (mg)
Before	1.785	1.785	6.13	6.13	8.28	28.16	27.94
	1.785	1.785	6.11	6.11	8.28	28.14	27.93
	1.783	1.783	6.10	6.10	8.29	28.16	27.95
	1.783	1.783	6.10	6.10	8.28	28.15	27.94
	1.784	1.784	6.10	6.10	8.29	28.17	27.95
	1.783	1.783	6.09	6.09	8.28	28.16	27.93
Average	**1.784**	**1.784**	**6.11**	**6.11**	**8.28**	**28.16**	**27.94**
SD	**0.001**	**0.001**	**0.01**	**0.01**	**0.01**	**0.01**	**0.01**
After	2.17	2.03	5.87	5.92	8.11	28.13	27.97
	2.18	2.03	5.86	5.93	8.08	28.12	27.98
	2.18	2.03	5.86	5.90	8.08	28.12	27.96
	2.18	2.04	5.85	5.91	8.08	28.13	27.96
	2.17	2.04	5.86	5.91	8.09	28.12	27.97
	2.18	2.04	5.85	5.91	8.09	28.13	27.96
Average	**2.18**	**2.04**	**5.86**	**5.91**	**8.09**	**28.13**	**27.97**
SD	**0.01**	**0.01**	**0.01**	**0.01**	**0.01**	**0.01**	**0.01**

VITA

Gyanendra Kharel
Department of Chemistry and Biochemistry
Old Dominion University
Norfolk, VA 23529

EDUCATION

Ph. D. (Expected May 2024) in Chemistry, Old Dominion University, Norfolk, VA 23529
M. S. (December 2021) in Chemistry, Old Dominion University, Norfolk, VA 23529
M. S. (December 2013) in Physical Chemistry, Tribhuvan University, Kathmandu, Nepal
B. S. (December 2003) in Chemistry, Tribhuvan University, Kathmandu, Nepal

PROFESSIONAL EXPERIENCE

2014-2016, Chemical and Environmental Analyst, Material Lab, Dubai, UAE

PUBLICATIONS

Kharel, G.; Sacko, O.; Feng, X.; Morris, J. R.; Phillips, C.; Trippe, K.; Kumar, S.; Lee, J. W. Biochar Surface Oxygenation by Ozonization for Super High Cation Exchange Capacity. ACS Sustain. Chem. Eng. 2019, 7, No. 16410.

Sacko, O.; Whiteman, R.; Kharel, G.; Kumar, S.; Lee, J. W. Sustainable chemistry: solubilization of phosphorus from insoluble phosphate material hydroxyapatite with ozonized biochar. ACS Sustain. Chem. Eng. 2020, 8, No. 7068.

Raut, K.K.; Pandey. S.; Kharel, G.; Pascal, S.M. Evidence of direct interaction between cisplatin and the caspase-cleaved prostate apoptosis response-4 (cl-Par-4) tumor suppressor. Protein Science 2023, p.e4867.

HONORS AND AWARDS

2023, 6th Annual Three Minute Thesis Competition (Second place and the People's choice award), Old Dominion University, Norfolk VA 23529
2022, SEES Graduate Travel Award, Old Dominion University, Norfolk, VA 23529
2022, SEES Leadership Awards (Nominated for Ellen Neufeldt Leader of the Year), Old Dominion University, Norfolk, VA 23529
2022, Outstanding Teaching Assistant (Chemistry and Biochemistry), Old Dominion University, Norfolk, VA 23529
2022, Graduate Research Achievement Day research poster competition (Honorable mention), Old Dominion University, Norfolk VA 23529
2016, Employee of the year, Material Lab, Dubai